ULTRAFAST MOLECULAR DYNAMICS INDUCED BY FEW-FEMTOSECOND ULTRAVIOLET EXCITATION

Dissertation
zur Erlangung des Doktorgrades
an der Fakultät für Mathematik, Informatik und Naturwissenschaftenät
Fachbereich Physik
Hamburg Universität

vorgelegt von

LORENZO COLAIZZI

Hamburg
2022

Gutachterinnen der Dissertation:	Prof. Dr.. Francesca Calegari
Zusammensetzung der Prüfungskommission:	Prof. Dr. Francesca Calegari Prof. Dr. Markus Drescher Prof. Dr. Franz Kärtner Prof. Dr. Mauro Nisoli Prof. Dr. Daniela Pfannkuche
Vorsitzender der Prüfungskommission:	Prof. Dr. Daniela Pfannkuche
Datum der Disputation:	13. Oktober 2022
Vorsitzender des Promotionsausschusses Physik:	Prof. Dr. Wolfgang Parak
Leiter des Fachbereichs Physik:	Prof. Dr. Günter H. W. Sigl
Dekan der Fakultät MIN:	Prof. Dr. Heinrich Graener

ABSTRACT

Pushing our capability of watching and controlling the microscopic world in real-time is one of the main challenges of spectroscopy today. Ultrashort lasers have been the best candidate to this purpose. Femtosecond ($1\,\mathrm{fs} = 10^{-15}\,\mathrm{s}$) lasers were critical for the birth of femtochemistry, allowing investigation and potential control of chemical reactions at the fs time scale, the natural time scale of nuclear motion in matter. Furthermore, the advent of attosecond ($1\,\mathrm{as} = 10^{-18}\,\mathrm{s}$) laser science has pushed this frontier even further setting the route to explore the natural time scale of electrons. Despite the many outstanding results in this field, our understanding of ultrafast molecular physics is still at its infancy and intense research needs to be pursued.

The work presented in this thesis aims at tackling this challenge with the development of an attosecond beamline for pump-probe experiments. It consists in a 3-arms interferometer which combines extreme ultraviolet (XUV) attosecond pulses, few-cycle near-infrared (NIR) pulses and the novel few-fs ultraviolet (UV) pulses. The beamline has been employed for the investigation of ultrafast molecular dynamics in a set of gas-phase molecules of increasing complexity, whose studies represent the main part of the thesis.

In methyl-iodide, the few-fs UV pulse was used to trigger an ultrafast non-adiabatic dynamics in the molecule in the vicinity of a conical intersection. The evolution was probed by NIR-induced ionization, observing a novel ultrafast dynamics in the pump-probe appearance of the iodine fragment.

We employed the few-fs pulse to excite a coherent superposition of Rydberg states through a 2-photon absorption in acetone. The evolution is then probed by ionization through a few-cycle linearly polarized NIR pulse. Both photoelectrons and photoions showed ultrafast oscillations that can be assigned to vibrational or purely electronics motion.

In methyl-lactate, the UV pulse was used to populate a set of Rydberg states in the neutral molecule. The excitation was then followed by single-photon ionization by a circularly polarized NIR pulse. With this scheme, we demonstrated that by inducing electronic coherence it is possible to modulate the chiral response of the molecule.

Finally, large water clusters were ionized by an XUV attosecond pulse train as a preliminary step for measuring electron dynamics in such complex target. We demonstrated a robust protocol to isolate the water clusters contribution in the photoelectron kinetic energy spectrum, which is affected by other species inevitably produced by the cluster source.

ZUSAMMENFASSUNG

Die Fähigkeit, die mikroskopische Welt in Echtzeit zu beobachten und zu kontrollieren, ist eine der größten Herausforderungen der heutigen Spektroskopie. Ultrakurzpulslaser sind die besten Kandidaten für diesen Zweck. Femtosekundenlaser ($1\,\mathrm{fs} = 10^{-15}\,\mathrm{s}$) waren entscheidend für die Entstehung der Femtochemie, da sie die Untersuchung und potenzielle Kontrolle chemischer Reaktionen auf der Zeitskala von fs, der natürlichen Zeitskala der Kernbewegung in Materie, ermöglichen. Darüber hinaus hat das Aufkommen der Attosekunden-Laserforschung ($1\,\mathrm{as} = 10^{-18}\,\mathrm{s}$) diese Grenze noch weiter verschoben und den Weg zur Erforschung der natürlichen Zeitskala von Elektronen geöffnet. Trotz der vielen herausragenden Ergebnisse auf diesem Gebiet ist unser Verständnis der ultraschnellen Molekülphysik noch am Anfang, und es muss noch intensiv geforscht werden.

Die in dieser Doktorarbeit vorgestellten Arbeiten zielen darauf ab, diese Herausforderung mit der Entwicklung einer Attosekunden-Beamline für Pump-Probe-Experimente anzugehen. Sie besteht aus einem 3-armigen Interferometer, Interferometer, welches extreme ultraviolette (XUV) Attosekundenimpulse, Nahinfrarotimpulse (NIR) mit wenigen optischen Zyklen und neuartige ultraviolette (UV) Impulse mit wenigen fs kombiniert. Die Beamline ist mit einem Doppelspektrometer zum Nachweis geladener Teilchen gekoppelt, mit dem gleichzeitig Elektronen-Velocity-Map-Imaging (VMI) und Time-of-Flight-Massenspektren (TOFMS) aufgenommen werden können. Die Beamline wurde für die Untersuchung der ultraschnellen Molekulardynamik in einem Satz von Molekülen in Gasphase mit zunehmender Komplexität eingesetzt, wobei dessen Untersuchungen den Hauptteil der Arbeit ausmachen.

Bei Methyljodid wurde der few-fs UV-Puls verwendet, um eine ultraschnelle nicht-adiabatische Dynamik in dem Molekül, welches sich in der Nähe einer konischen Kreuzung befindet, auszulösen. Die Entwicklung wurde durch NIR-induzierte Ionisierung untersucht, wobei eine neuartige ultraschnelle Dynamik in der Pump-Probe Erscheinung des Iodfragments beobachtet wurde.

Wir haben den extrem kurzen Impuls verwendet, um eine kohärente Überlagerung von Rydberg-Zuständen durch eine 2-Photonen-Absorption in Aceton anzuregen. Die Entwicklung wird dann durch Ionisierung mittels eines linear polarisierten NIR-Pulses mit wenigen Zyklen untersucht. Sowohl die Photoelektronen als auch die Photoionen zeigten ultraschnelle Oszillationen, die Schwingungen oder rein elektronischen Bewegungen zugeordnet werden können.

In Methyl-Lactat wurde der UV-Impuls dazu verwendet, um eine Reihe von Rydberg-Zuständen im neutralen Molekül anzuregen. Auf die Anregung folgte dann die Einzelphotonen-Ionisierung durch einen zirkular polarisierten NIR-Impuls. Mit diesem Schema haben wir gezeigt, dass es möglich ist, die chirale Reaktion des Moleküls durch Induktion elektronischer Kohärenz zu modulieren.

Schließlich wurden große Wassercluster durch einen XUV-Attosekundenpulszug ionisiert, um die Elektronendynamik in solch komplexen Targets zu messen. Wir demonstrierten ein robustes Verfahren, um den Beitrag der Wassercluster im kinetischen Energiespektrum der Photoelektronen zu isolieren, der durch andere Spezies, die unvermeidlich von der Clusterquelle erzeugt werden, beeinflusst wird.

PUBLICATIONS AND CONFERENCES

Some of the research leading to this thesis has appeared previously in the following publications or are in preparations

JOURNAL ARTICLES

- "Investigation of methyl-iodide photodissociation with few-fs resolution"

  L.Colaizzi, J. González-Vázquez, K. Saraswathula, S. Riabchuk, E. P. Månsson, , V. Wanie, A. Trabattoni, F. Martin and F. Calegari
  in preparation

- "Covariance mapping for acetone dissociation"

  L.Colaizzi, K. Saraswathula, S. Riabchuk, E. P. Månsson, V. Wanie, A. Trabattoni and F. Calegari
  in preparation

- "Femtosecond-resolved Rydberg states dynamics in chiral molecules"

  V. Wanie, E. Bloch, Erik P Månsson, **L. Colaizzi**, K. Saraswathula, S. Riabchuk, F. Légaré, A. Trabattoni, M.C. Heitz, N. Ben Amor, V. Blanchet, Y. Mairesse, B. Pons and F. Calegari
  in preparation

- "Investigation of ultrafast chiral electron dynamics with site- and chemical-specificity: time-resolved photoelectron circular dichroism at Free Electron Laser"

  D. Faccialà, M.Devetta, S. Beauvarlet, N. Besley, F. Calegari, C. Callegari, D. Catone, E. Cinquanta, A. G. Ciriolo, **L. Colaizzi**, M. Coreno, G. Crippa, G. De Ninno, M. Di Fraia, M. Galli, G. Garcia, Y. Mairesse, M. Negro, O. Plekan, P. Prasannan Geetha, K. Prince, A. Pusala, S. Stagira, S. Turchini, K. Ueda, D. You, N. Zema, V. Blanchet, L. Nahon, I. Powis, C. Vozzi
  – *PRX*, 2022
  submitted
  – arXiv doi: 10.48550/arXiv.2202.13704

- "Photoelectron Spectroscopy of Large Water Clusters Ionized by an XUV Comb"

  A. Trabattoni, **L. Colaizzi**, L. Ban, V. Wanie, K. Saraswathula, E. P. Månsson, P. Rupp, Q. Liu, L. Seiffert, E. A. Herzig, A. Cartella, B.L. Yoder, F. Legare, M.F. Kling, T. Fennel, R. Signorell and F. Calegari

– *J. Phys. Photonics 2 035007 (2020)*
doi: 10.1088/2515-7647/ab92b1.

- "Generation of deep ultraviolet sub-2-fs pulses"

  M. Galli, V. Wanie, D. P. Lopes, E. P. Månsson, A. Trabattoni, **L. Colaizzi**, K. Saraswathula, A. Cartella, F. Frassetto, L. Poletto, F. Légaré, S. Stagira, M. Nisoli, R. Martínez Vázquez, R. Osellame, F. Calegari
  – *Optics Letters Vol. 44, Issue 6, pp. 1308-1311 (2019)*
  doi: 10.1364/OL.44.001308

BOOK CONTRIBUTIONS

- "Advances of ultraviolet light sources: towards femtosecond pulses in the few-cycle regime"

  V. Wanie, **L. Colaizzi**, A. Cartella, A. Trabattoni and F. Calegari
  – in *Emerging Laser Technologies for High-Power and Ultrafast Science*, edited by F. Légaré, 2053-2563.
  IOP Publishing, 2021. ISBN:978-0-7503-2536-3

PROCEEDINGS

- "Angle-resolved Photoelectron Spectroscopy of large Water Clusters ionized by an XUV Comb"

  L. Colaizzi, L. Ban, V. Wanie, K. Saraswathula, E. P. Månsson, P. Rupp, Q. Liu, L. Seiffert, E. A. Herzig, A. Cartella, B.L. Yoder, A. Trabattoni, F. Legare, M.F. Kling, T. Fennel, R. Signorell and F. Calegari
  – *The 22nd International Conference on Ultrafast Phenomena 2020*, paper Tu4A. 31
  doi: 10.1364/UP.2020.Tu4A.31

- "Core-level Time Resolved Spectroscopy of Photoelectron Circular Dichroism in Fenchone"

  D. Faccialà, M. Devetta, S. Beauvarlet, N. Besley, F. Calegari, C. Callegari, D. Catone, E. Cinquanta, A. Ciriolo, **L. Colaizzi**, M. Coreno, G. Crippa, G. De Ninno, M. Di Fraia, M. Galli, G. Garcia, Y. Mairesse, M. Negro, O. Plekan, I. Powis, P. Prasannan Geetha, K. Prince, A. Pusala, S. Stagira, S. Turchini, K. Ueda, D. You, N. Zema, L. Nahon, V. Blanchet and C. Vozzi
  – *The 22nd International Conference on Ultrafast Phenomena 2020*, paper M3B.5
  doi: 10.1364/UP.2020.M3B.5

CONFERENCE CONTRIBUTIONS

Oral presentations

- "Ultrafast molecular dynamics induced by few-femtosecond ultraviolet excitation"

  L.Colaizzi, K. Saraswathula, S. Riabchuk, E. P. Månsson, V. Wanie, A. Trabattoni and F. Calegari
  – *AttoChem Young scientist symposium 2021*, 14th-17th September 2021, (online)
  link

Poster presentations

- *MML workshop (2021)*, 22nd -24th November 2021,Jena, Germany (online)
  link
- *2nd Annual Workshop of the COST Action AttoChem (2021)*, 13th-15th October 2021, Hamburg, Germany (online)
  link
- *2021 Conference on Lasers and Electro-Optics Europe (CLEO/Europe)*, 21th-25th July, 2021, (online)
  link
- *the 32nd International Conference on Photonic, Electronic and Atomic Collisions*, 20th-23th July,2021, (online)
  link
- *2021 Conference on Lasers and Electro-Optics Europe (CLEO/Europe)*, 21th-25th July, 2021, (online)
  link
- *52nd Annual Meeting of the APS Division of Atomic, Molecular and Optical Physics (DAMOP)*, 31st June -4th July, 2021, (online)
  link
- *Time-resolved imaging of photo-induced dynamics Faraday Discussion*, 1st - 4th February 2021, (online)
  link
- *The 22nd International Conference on Ultrafast Phenomena 2020*, 16th-20th November 2020, (online)
  link
- *1st Annual Workshop of the COST Action AttoChem 2020*, 9-11 September 2020, (online)
  link

- *7th International Conference on Attosecond Science and Technology (ATTO 2019)*, 1st-5th July 2019, University of Szeged Congress Centre, Hungary
  link

- *PALM International School 2018*, 28th May - 1st June 2018, Benoit Frachon Conference Center Gif-sur-Yvette (near Paris), France
  link

CONTENTS

1

INTRODUCTION

A major turning point in science has always been the identification of the suitable time scale to describe a dynamical process. On the most fundamental level, it translates into identifying the most suitable time interval, or clock, to record the individual steps of the process. For instance, the "Astronomical Calendar" was firstly introduced in ancient Egypt to time the number of days in a year as consequence of the observation of the heliacal rising of the star Sirius. Since then, significant effort has been done in order to find or develop the most suitable time reference. In particular, when scientists began to access the microcosm, they discover that the constituents of matters move with incredible rapidity. Because of inertia, there is an intrinsic relation in between the mass of an object and its velocity. Therefore, we expect to address faster and faster processes the deeper we dive into the structure of matter and the smaller the observed objects become (Fig. 1.1).

The structural rearrangement of proteins occurs generally on the millisecond (ms) scale, but it can reach the microsecond (µs), when considering α-helix formation. Chemical reactions such as proton transfer, take place from the nanosecond (ns) down to femtosecond (fs) time range, depending on the complexity of the species involved. Molecular collisions, which are interpreted as Brownian motion of molecules in a gas, are more suitably described on the picosecond (ps) range. Tens of ps are also well suited to molecular rotation in space. The natural time scale for internal vibrational motion of the nuclei in a molecule is the *femtosecond* (10^{-15} = fs). For example, the $H-H$ stretching period of molecular hydrogen is 7.6 fs. When dealing with faster processes, which involve electrons, the *attosecond* (10^{-18} = as) describes their motion in atoms, molecules, and solids.

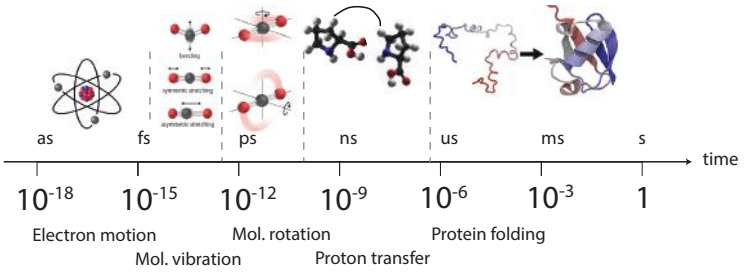

Figure 1.1: Different time scale in molecular dynamical processes.

The interest for such processes can be understood by the most straightforward meaning of the word dynamics that is "change". Changes in chemistry are described through chemical reactions in which reagents are put together to create new products. From a physical perspective, chemical reactions can be considered as the sum of all the extremely fast elementary processes described above. By means of molecular translations, rotations, vibrations and even electronic transitions, molecules undergo specific rearrangements of atoms, which lead to bond breaking and remaking to ultimately form the final product species. Since most of these steps are conveniently measured in femtoseconds, one can say that "all chemistry is femtochemistry" [1]. Gaining access to this domain, or the investigation of each elementary processes and the understanding of their complex combinations, is crucial in unravelling specific chemical or physical mechanisms and identifying fundamental ingredients towards the successful outcome of the reactions. In other words, understanding comes before control.

Up to the 19th century, recording times of individual steps in any process was essentially limited to the time scales related to direct sensory perception, such as vision (0.1 s) or hearing (0.1 ms). Only with the invention of the first Ruby Laser by T. Maiman in the 1960 [2], the temporal resolution increased drastically, reaching only two decades later the 100 fs range. The time resolution increased by more than 10 order of magnitude in respect to the previous century.

As a consequence, the development of femtosecond lasers has revolutionized our understanding of molecular dynamics. A. H. Zewail demonstrated the possibility of using femtosecond lasers to track chemical reactions in real time in a series of studies which awarded him the Nobel prize for Chemistry in 1999 [3]. In such experiments, a first femtosecond pulse, named *pump*, initiates the dynamics and acts as a starting clock by defining its zero time. A second femtosecond pulse, called *probe*, provides the shutter speed for freezing the nuclear motion and recording the particular snapshot. By accurately synchronized the pump - probe delay, an acquisition of snapshots at different times of the molecular evolution allows for the full molecular dynamics to be observed.

These pioneering experiments founded the well-established field of femtochemistry. Applied for the first time to study photodissociation dynamics of ICN [4], femtochemistry has been extended in the investigation of a wide variety of molecular processes by combining femtosecond pulses with different observables such as spectroscopy, mass spectrometry and diffraction spectrometry [5]. Additionally, femtochemistry introduced the possibility to control chemical reaction by steering the motion of the nuclei of the involved molecules, by selectively breaking bonds and favoring others. In practice, *coherent control* is based on the re-shaping of femtosecond pulses in frequency and amplitude in order to drive the molecular system to a specific reaction

channel [6, 7]. Through the use of these methods, femtochemistry established itself as the first real possibility of controlling chemical reaction in real time, by exploiting femtosecond laser duration and coherence to efficiently control the nuclei dynamics.

Attosecond dynamics in molecules

At the beginning of the new century development in ultrafast sources allowed the creation of light pulses in the extreme ultraviolet spectral range (XUV) of even shorter duration, down to the attosecond time scale.

Ever since the first experimental demonstrations in 2001 [8, 9], attosecond pulses have been employed to measure Auger relaxation dynamics in noble gas [10]. Afterwards, they have been applied on many atomic processes such as the real time observation of valence electron motion in krypton [11], characterization of the electron wavepackets in helium [12] and the measurements of the photoionization delay [13, 14] to name just a few. The success in atomic targets clearly showed the potential of attosecond sources and were fundamental for the development of the experimental techniques which gave access to the natural time scale of electron motion.

At the time attosecond pulses were demonstrated, applications towards molecular systems were immediately suggested. Observing the electronic degrees of freedom in molecules on attosecond timescales is very appealing since it provides novel pathways towards controlling chemical processes. The first molecular attosecond experiment addressed charge localization during the dissociation ionization of the hydrogen molecule [15]. Immediately after, the feasibility of controlling the dissociation of the molecule was demonstrated, by acting in the very first instant of motion [16]. These two of experiments manifest the dual nature of employing attosecond pulses on molecular target. On one hand, attosecond pulses stands as the ideal tool to unravel extremely fast processes in nature. For instance, ultrafast electron dynamics induced by light has been proven to play a crucial role in the initial stages of photosynthesis, in radiation damage of biologically relevant molecules and in the general in any chemical or biological process which is related to electron transfers. On the other hand, attosecond pulses can be used as control knob to steer electron dynamics and to guide chemical reactions [17, 18].

In femtochemistry, the time domain observation is based on the fact that the pump laser excites a coherent superposition of states, which evolves with a phase factor that is proportional to their energy. The shorter the duration of the pump laser, the larger is its frequency bandwidth and the larger is the energy bandwidth of the excited wavepackets. Because femtosecond pulses were mostly employed, femtochemistry experiments were almost exclusively limited on the

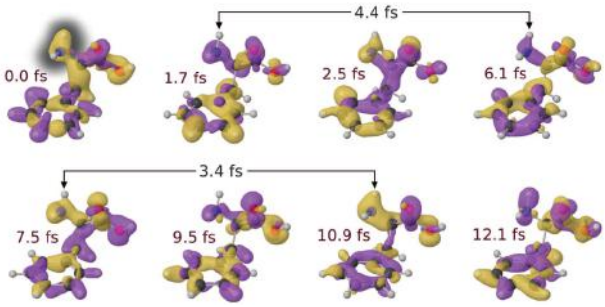

Figure 1.2: Ultrafast dynamics of the hole density in the amino acid phenylalanine induced by sudden ionization by an attosecond XUV pulses. Adapted from [22].

excitation of purely rotational or vibrational nuclear wavepackets, without directly affecting the electronic states. The experiment could then reveal the evolution of such a wavepacket, through processes such as dissociation, internal conversion or intersystem crossing, including conical intersection where multiple electronic states become degenerate for a particular molecular geometry. The development of attosecond pulses introduced the perfect tool to move beyond this concept, since their bandwidth typically spans a range of different electronic states allowing electronic coherences to be excited. Due to bandwidth of such electronic wavepacket, the subsequent motion occurs on a time scale ranging from attoseconds to a few femtoseconds. The creation of an electronic wavepacket, whose motion is purely driven by their coherent superposition and not by the nuclei, open up new possibilities to steer the subsequent nuclear motion and affect the resulting reaction, for instance to circumvent vibrational energy redistribution [19].

A purely electronic motion driven only by electronic correlation was first observed in a pioneering experiment by Weinkauf *et al.* [20]. It was suggested as an interpretation of an extremely efficient charge transfer along the chain of a small peptide. Such motion was named *charge migration* to distinguish the coherent evolution of purely electronic states from the charge rearrangement encountered in electron transfer processes, which are governed by electrons-nuclei coupling on longer timescale [21]. More than a decade later, ultrafast charge migration was observed in the amino acid phenylalanine, after prompt ionization by an isolated attosecond pulses [22]. In this experiment, the electronic correlation was induced by the extremely large bandwidth of the ionizing pulses, which coherently excites several cationic states. As a result, a sub-4.5 fs charge motion was observed along the molecule as it is depicted in Fig. 1.2. The charge density redistributes along the molecules, oscillating in particular around the ammine group.

Two remarks need to be made here, which provide the motivation for the work described in this thesis. First of all, the extremely large

bandwidth of an attosecond pulses, although allowing the excitation of several electronic states, creates the condition for which it will pump or probe an extremely considerable number of states, including many vibrational and rotational states, all at the same time. In other words, attosecond pulses activate many distinct dynamical processes at the same time. In particular, it is even more worsen when the XUV attosecond pulses are used in combination with the typical NIR probe, which easily allows multiphoton probing. Most of the case, one has to rely on the invaluable contribution of theory, which helps unravel the different contribution to address the specific dynamics observed in the experiment.

In most cases, the excitation of electronic coherences takes molecular dynamics outside the realm of the Born-Oppenheimer approximation [23] in which the nuclear and electronic degrees of freedom can be decoupled, due the fact that the mass of the electron is smaller by several order of magnitude than the nuclei. This approximation leads to the common description of molecular dynamics in terms of rotational and vibrational wavepackets moving on a potential energy surface, which is typically used to describe femtochemistry experiments where only a single electronic state is excited. In such a description, points in which two electronic states are degenerate, i.e., molecular geometries for which two potential energy surfaces corresponding to two distinct electronic states approach each other represents particular cases. They represent points for which the electrons time scale is slowed down to a time scale comparable to the ro-vibrational dynamics, in which the coupling in between nuclei and electron degrees of freedom cannot be neglected. Excitation of electronic coherences, more likely involving several electronic states obviously needs to include such effects, where the electronic and the nuclear dynamics must be treated in a correlated manner. From this perspective, attosecond pulses are the perfect tool to study molecular dynamics in the presence of conical intersections and gain more insights about these regions where the Born-Oppenheimer approximation fails [24].

Ultraviolet excitation

While XUV attosecond pulses allows to study electronic wavepackets only after ionization, broadband UV pulses are able to excite electronic coherences in the neutral, because of the lower photon energy, typically below the ionization potential of most molecules. This property can be used to extend purely electronic motion to the neutral molecule. Additionally, over the last few years it became clear the that the breakdown of the Born-Oppenheimer approximation at conical intersection plays a crucial role in many fundamental photo-induced processes in nature, such as vision, photosynthesis and radiation damage in biomolecules

[25]. Therefore, few-femtosecond UV pulses can be applied to tackle specific problems of fundamental interest in photochemistry.

UV light is defined as electromagnetic radiation with wavelength shorter than 400 nm and it comprises of three classes: UV-C (200 nm to 280 nm), UV-B (280 nm to 315 nm) and UV-A (315 nm to 400 nm). In particular, the main source of UV light in nature is the sun with fundamental impact on biology, including production of vitamin D, vision, and DNA photodamage, among others. The general interest in chemistry for this energy range comes from the fact that these energies match electronic transitions in molecules and for this reason they are responsible many photo-induced processes. For instance, in more complex biomolecules, the presence of chromophore such as imidazole, pyrrole and phenol results in strong UV absorption in aromatic amino acids or nucleobases [26]. Despite the fact that UV radiation is only a minor fraction of the sunlight reaching Earth's surface, it represents the most harmful and mutagenic component of the solar spectrum. For example, it is the main responsible of the formation of nucleobases dimers in DNA, an altered structures which interfere with the normal DNA polymerases decoding and can ultimately lead to mutation and skin cancer [27]. It is anyway surprising that the overall mechanism which leads to this mutation is strongly inefficient, because of ultrafast relaxation mechanisms through which nucleobases can dissipate the excessive energy through very efficient non-radiative decays due to the very short lifetimes (< 200 fs) of the excited states involved [28]. The remarkable stability of DNA bases upon UV radiation can be understood in terms of protection mechanisms involving ultrafast relaxation around conical intersections [29], however investigation of such dynamics has been scarce, because of the lack of suitably short excitation pulse.

Non-linear upconversion schemes for UV generation are based on typically second harmonic generation, coupled with sum frequency generation by using Ti:Sapphire laser input, but the intrinsic dispersion of the BBO medium limited the pulses duration to hundreds of femtoseconds, with proposed complex scheme aiming at introducing negative dispersion, even with a lack of negative dispersive medium in the UV [30]. In 2019, we demonstrated the feasibility of producing sub-2 fs UV pulses by employing third harmonic generation in noble gas driven a few-cycle NIR pulses [31]. The spectrum of such pulses is reported in Fig 1.3, extending from 210 nm to 340 nm - which corresponds to a bandwidth of 2.28 eV - and a temporal duration which was measured to be 1.95 fs. The demonstration of such short pulses in the ultraviolet acts as a bridge which connect attosecond science in molecules with neutral molecular dynamics and chemical processes, explored so far only on a longer time scale.

Beyond the duration record, we can currently generate sub-2 fs pulses in a vacuum beamline which is set up for pump-probe exper-

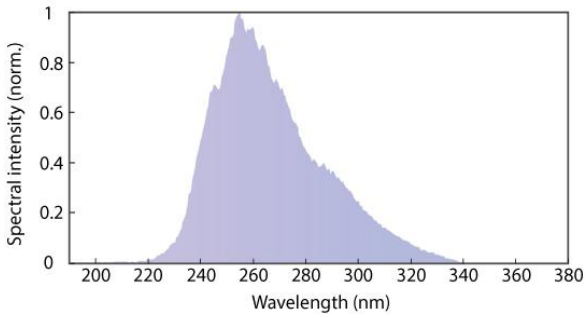

Figure 1.3: Ultraviolet spectrum supporting 1.45 fs time duration generated third harmonic generation in gas by a few-cycle NIR pulses. The corresponding time duration was measured to be 1.95 fs. Adapted from [31].

iments, which combines the UV pulses with NIR infrared few-cycle pulses and in the future with XUV attosecond pulses. In this thesis I will present the first experimental efforts in using few-femtosecond UV pulses, in a series of benchmark pump-probe experiments on different targets.

The aim of this work is to show that spectroscopy employing ultrashort UV pulses opens new ways in investigating the photo-induced electron dynamics in the excited targets. In the first place, it allows investigation of photo-induced processes with unprecedented time resolution. This will be shown in an experiment of photodissociation in methyl-iodide, a prototypical target for ultrafast UV-induced dynamics. Employing such short excitation pulses allow us to retrieve dynamics which were never observed before. Additionally, we will explore the possibility of triggering electronic coherences in the neutral. It will be shown in an experiment performed in acetone, by exciting a superposition coherent of Rydberg states exploiting the bandwidth of the few-fs UV pulses. Such experiments aim at interrogating the role of electrons in the first moments upon photo-excitation, also addressing the interaction of nuclear and electronic degrees of freedom. Finally, we will show that electronic coherence and their evolution can be exploited to control the chiral response of methyl-lactate molecules, demonstrating chemical control over a few-fs time scale.

To conclude, the work included in this thesis aim at extending UV spectroscopy to the few-fs time scale, or alternatively to extend attosecond science from XUV to lower photon energy. I will show different possibilities of employing few-femtosecond ultraviolet excitation in molecules, with the aim in addressing fundamental questions: (*i*) what is the role of electrons in the first moments upon photo-excitation? (*ii*) how does nuclear and electronic degrees of freedom are coupled to each other? The answers to these questions are of fundamental

importance towards photo-induced control of chemical reactions in the very first instant after excitation [32].

1.1 ORGANIZATION OF THE WORK

The thesis is organized as follow.

The following chapter (Ch.2) introduces many concepts which are fundamental to the understanding of the work presented in the thesis, focusing on general model of molecular dynamics and light-matter interaction.

Ch.3 contains all the details of the experimental setup employed in all the experiments. Initially, the beamline providing the three different light sources for pump-probe spectroscopy is introduced. Afterwards, the particle detection instruments, and the molecular source employed are described. Finally, we focus on the effort towards improving the few-fs UV pulses generation.

The remaining chapters of the thesis cover the different experiment performed. Each chapter starts with a brief introduction on the particular target or method employed.

Ch.4 is about the investigation of methyl-iodide, a halide-alkane substitute. This molecule represents the prototypical molecule in investigating UV-induced ultrafast dynamics, as it shows a strong absorption at 266 nm which results in an ultrafast photodissociation, but so far was never investigated on this time resolution. The experimental approach and theoretical interpretation of the results are reported.

Ch.5 reports the investigation of the evolution of a Rydberg excitation in acetone. A detailed experimental effort, exploiting the possibility of our setup of measuring simultaneously the emitted photoelectrons kinetic energy and the produced fragments. Despite the fact that a detailed theoretical support is not ready yet, discussion about the interpretation of the experimental data is attempted on the basis of previous works.

The use of photoelectron circular dichroism to investigate the chiral response induced by electronic coherences in methyl-lactate is described in Ch.6. The experimental method will be treated in detail, in particular regarding the necessity of using differential methods to be able to observe the evolution of the electronic wavepackets on a few-femtosecond scale.

Ch.7 describe a preliminary experiment in which we investigate the photoionization of water clusters from an XUV attosecond pulses. It stands as a first step to extend attosecond experiments to complex target aiming at studying molecules in solution.

Finally, the last chapter (Ch. 8) will be dedicated to summarizing all the results and provide an outlook for each experiment.

2

FUNDAMENTALS OF LIGHT-MATTER INTERACTION

On the most fundamental level, spectroscopy studies the interaction of radiation with matter, which occur through absorption, emission or scattering processes. Since these processes involve different transitions inside the molecular target - rotational, translational, vibrational and electronic, and depend directly on the energy of photons used, spectroscopy allows us to investigate in detail the structure of microscopic systems by employing different light sources across the electromagnetic spectrum.

For many of these processes, light-matter interaction is usually described through a semi-classical approach, in which the system is described using quantum mechanics and the radiation is treated classically, using Maxwell's equations. This is generally justified by the high intensities involved, which allows light to be considered as a continuous photon flux.

Every microscopic system is characterized by a series of quantized energy levels, obtained as eigenstates of the Hamiltonian of the system, known also as time-independent Schrödinger equation. When electromagnetic radiation interacts with the particle system, it causes a time-dependent perturbation that can induce transitions between the different quantum states. This transition probability is estimated using the time-dependent Schrödinger equation.

As first approximation, the role of the magnetic field can be neglected since the electric field is considerably more intense. In addition, the wavelength of the radiation is usually much larger than the typical size of the molecular target. In other words, the spatial variation of the electric field is exceedingly negligible compared to the distances on which electron or nuclei move. This leads to the so-called dipole approximation and all the transitions involved are called electric dipole transitions.

Applying the first-order theory of time-dependent perturbations, one can calculate the probability of such transition. In the simplest case of weak and long perturbation, the transition rate, or transition probability per unit time, in between two molecular states F_f and F_i is expressed by

$$k_{fi} = \frac{\pi}{2\hbar^2}\,\delta\left(\omega_{fi} - \omega\right)\left|\left\langle F_f \left| \vec{e}\cdot\vec{d} \right| F_i \right\rangle\right|^2 \tag{2.1}$$

where $\omega_{fi} = (E_f - E_i)/\hbar$ represents the energy difference between the two states, ω is the radiation frequency and $\vec{e}\cdot\vec{d}$ is the projections of the dipole operator on the direction of the field polarization. The

necessary conditions to obtain a maximum transition probability imply that: firstly, radiation frequency should be resonant with the transition; secondly, symmetry selection rules in between the initial and final states must be met.

2.1 ADIABATIC DESCRIPTION

On a more general level, the stationary states introduced in 2.1 represent the general stationary states of the molecule $F(\vec{q},\vec{Q})$ including all electronic $\vec{q}$ and all nuclear $\vec{Q}$ degrees of freedom. However, in the description of molecular systems it is always convenient to separate the molecular wavefunction into a nuclear part $\Phi^n(\vec{Q})$ and an electronic part $\chi^{el}(\vec{q};\vec{Q})$, with the latter depending only parametrically on the nuclear coordinates. This separation is done by employing the *Born-Oppenheimer approximation* [ref].

Essentially, the molecular Hamiltonian is

$$\hat{H}_{mol}(\vec{Q},\vec{q}) = \hat{T}_n(\vec{Q}) + \hat{H}_{el}(\vec{q};\vec{Q}) \tag{2.2}$$

where $\hat{T}_n$ is the nuclear kinetic energy and $\vec{H}_{el}$, the latter comprising the kinetic energy of the electrons and all the electrostatic potential interaction (electron-electron repulsion, electron-nuclear attraction, and the nuclear-nuclear repulsion). We note that the second term only depends on the nuclear coordinate $\vec{Q}$ parametrically, because all the differential operators are contained in the first term. This allows the so-called *adiabatic representation* in which we expand the complete molecular wavefunctions according to

$$F(\vec{q},\vec{Q}) = \sum_k \Phi_k^n(\vec{Q})\chi_k^{el}(\vec{q};\vec{Q}), \tag{2.3}$$

where the electronic expansion functions $\chi_k^{el}(\vec{q};\vec{Q})$ are solutions of only the electronic Schrödinger equation

$$\left[\hat{H}_{el}(\vec{q};\vec{Q}) - V_k(\vec{Q})\right]\chi_k^{el}(\vec{q};\vec{Q}) = 0 \tag{2.4}$$

with eigenvalues $V_k(\vec{Q})$ for any fixed nuclear configuration $\vec{Q}$ and index k indicating different electronic states (with $k = 0$ being the ground states). The eigenenergies are called potential energy surfaces (PES) and are fundamental in the semi/classical interpretation of any molecular dynamics.

The physical background of the Born-Oppenheimer approximation is the extreme difference of the electronic and nuclear velocities. Due to their heavier masses, nuclei will move infinitely slowly in respect to the electrons. This means that the electronic wavefunctions will depend only weakly with $\vec{Q}$. This allows to neglect any derivative terms (in respect to nuclear coordinates) on the electronic wavefunctions

and obtain a set of uncoupled equations from (2.2) for the nuclear wavefunctions

$$\left[\hat{T}_n(\vec{Q}) + V_k(\vec{Q}) - E\right] \Phi_k^n(\vec{Q}) = 0, \tag{2.5}$$

where the PES acts as potentials for the nuclei. In particular, the coupling in between different electronic states is absent and therefore the motion of nuclei evolves separately in each electronic state, due to only a single potential energy surface $V_k(\vec{Q})$.

If, on the other hand, two electronic states are very close in energy in some region of the nuclear space $\vec{Q}$, the properties of the electronic wavefunctions strongly depends on $\vec{Q}$ and their derivatives on the nuclear coordinates cannot be neglected. Consequently, non-adiabatic coupling becomes substantial when the energy difference between two electronic PES becomes very small around specific points: the set of molecular geometries $\vec{Q}$ where two PESs have exact degeneracy are called *conical intersection* - or avoided crossings. Near these points transitions between different electronic states becomes possible. Conical intersections are present in polyatomic systems, and they are essential for many fundamental photochemical phenomena.

2.1.1 *Franck - Condon principles*

One of the most important consequences of the Born-Oppenheimer approximation in the photoexcitation experiment is the Franck-Condon principle. The separation of the various degrees of freedom leads to a factorization which is quite useful in the interpretation of every transition, in particular the one among different electronic states, which usually requires the high energy content that only light can provide. In general, the probability of a transition is governed by the nature of the initial and final state wave functions, how they interact with them and the intensity of incident light. The transition probability R^2 can be expressed as the degree of overlap of the wave functions following

$$R = \left\langle F_f \left| \vec{e} \cdot \vec{d} \right| F_i \right\rangle \tag{2.6}$$

where $\vec{e} \cdot \vec{d}$ is the dipole moment operator and F_i, F_f are initial a fine state. In other words, the stronger is the coupling in between different states due to the electric field, the more likely and stronger will be that specific transition. In the context of the Born-Oppenheimer, which allows to factorize the nuclear and electronic degrees of freedom we can express this separation (by including only vibrational transition)

$$R^2 = |R_e|^2 \, q_{v,v'} \tag{2.7}$$

where the first term reflects the electronic dipole transition probability, the second term is associated with the vibrational levels of the lower state v and the excited state, also known as Franck-Condon (FC) factors. In the adiabatic approximation in which electrons react much faster than nuclei, in every electronic transition the most likely transition in between different vibrational (or rotational) states are the one without major changes in the position of the nuclei. In other words, electronic transitions can be considered instantaneous compared to the time scale of the nuclei. In a potential energy diagram, these transitions are represented as vertical line, with no change in the reaction coordinate.

2.1.2 *Different type of transitions*

As already discussed, the probability of a photon being absorbed and the transition in between different states taking place is governed by the selection rules, which determine whether a transition is allowed or not. In absorption spectroscopy, for instance, this probability determines the intensity of the emission lines from an excited state, and it depends on the nature of initial and final state wave functions.

In most experiments of photoexcitation, the initial state will always be the ground state of the molecule. The final state will depend on the photon energy and can determined the following dynamics depending on the properties of the PES. In particular, stationary points on the PES corresponds to physically stable configuration of the molecule or bound state. The shape - or landscape - of a particular PES can also lead to dissociation of the molecule.

As an example, in Fig. 2.1 is reported a representation of a few examples of PESs of a diatomic molecule AB - and its cation AB^+. In this case, the PESs will depend only on the internuclear distance R_{AB}. Depending on the excitation energy, the molecule can undergo different photo-induced processes: photodissociation and photoionization.

2.1.2.1 *Photodissociation*

The molecule is driven by the absorption of a photon of energy D to a repulsive excited state AB^*. Considering Eq. (2.5), this potential will increase the internuclear distance until the molecule breaks apart. This process is called *photodissociation* and is described by the following reaction:

$$AB + \hbar\omega_D \rightarrow AB^* \rightarrow A(\alpha) + B(\beta),$$

where α and β represent a generic quantum state of the single atoms. The dynamical evolution which leads to dissociation is extremely fast (fs) because it follows only the repulsive PES, related only to the antibonding molecular orbital. For instance, the photodissociation of H_2O in the first absorption band is a prototype of this direct dissociation [33].

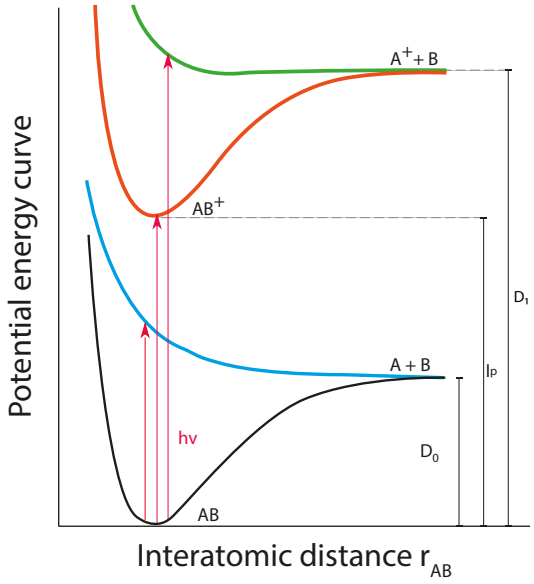

Figure 2.1: Schematic representation of photon excitation in a simple diatomic molecule AB as a function of the interatomic distance R_{AB}. If the photon energy $\hbar\omega$ is resonant to a repulsive potential energy surface AB^*, which leads to dissociation. When the photon energy is higher than ionization potential, an electron will be removed, bringing the molecule to a cationic state AB^+.

Nevertheless, dissociation via a single excited electronic state is the exception rather than rule: many other photodissociation processes, however, proceed via two or even more states with the possibility of transitions from one state to the another in many different ways. In the case of indirect photodissociation, after the excitation the molecule has to face different impediments before the actual bond cleavage. In Fig. 2.2 we reported a few examples.

- In Fig. 2.2 (a), the molecule is excited into a bound electronic state. However, this state is coupled at the same time with another repulsive excited state, through which the molecule can

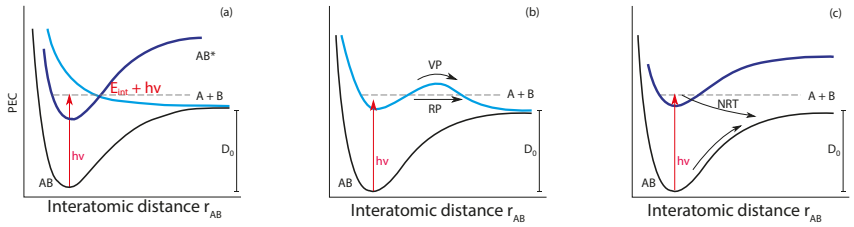

Figure 2.2: Different schemes for indirect photodissociation with the different potential energy curve (PEC) involved: (a) electronic predissociation, (b) vibrational predissociation and (c) unimolecular dissociation.

dissociate. This is called electronic predissociation or Herzberg's type I predissociation. The molecular dynamics depends strongly on the coupling in between the two states, which defines the probability of transition from the bound to the repulsive state.

- The molecule is excited to a quasi-bound state, in which the dissociation does not occur immediately due to the existence of a potential barrier, as depicted in Fig. 2.2 (b). However, due to internal energy redistribution, both vibrational (VP) or by tunnel effect (RP), the molecule can overcome the barrier. This is called Herzberg's type II vibrational photodissociation. The time scale depends on the speed with which the barrier is crossed.
- In the last case, called unimolecular dissociation and represented in Fig. 2.2 (c), the molecule can decay from a bound excited state to the ground state by internal conversion - a non-radiative transition (NRT) - with higher internal (vibrational, usually) energy content above the dissociation threshold.

2.1.2.2 *Photoionization*

If the energy of the absorbed photon is equal to or greater to the ionization potential I_p of the molecule, the removal of one electron from its valence shell can take place, leaving the molecule in its cationic state - in this case the ground state - AB^+ as depicted in Fig. 2.1.

$$AB + \hbar\omega_I \rightarrow AB^+ + e^-.$$

In particular, the emitted photoelectron will possess kinetic energy E_{kin}, which can be easily interpreted through Koopman's theorem [34]: assuming all other electrons in the system are unaffected, the quantity $E_{bin} = E_{kin} - \hbar\omega_I$ is equal to the binding energy of the removed electron and gives information regarding the molecular orbital from which is removed. In a more specific picture, this energy represents the difference in between the ground state energy and the *cationic state* of the molecule.

Photoionization is usually studied through photoemission/photoelectron spectroscopy (PES, also). The energy, abundance and angular distributions of the ejected electrons are a fingerprint of the molecular orbitals from which they are originated and thus, they provide relevant information of the molecular electronic structure and, in its time-resolved version, on the molecular dynamics, as we will discuss in the next section.

2.1.2.3 *Multiphoton process*

In addition to the previous transitions, several photons of energy below the ionization threshold (or the specific excitation energy) may actually be absorbed simultaneously to ionize (excite) the target in what is

called *multiphoton ionization* (excitation). The probability decreases rapidly with the number of photons required, but the use of very intense femtosecond lasers make this process very favorable since it scales with intensity I^N, where N is the number of photons required.

In this context, the selection rules for multiphoton processes differ from the selection rules for single-photon processes: dipole transitions involving an even number of photons are permitted only between states of identical parity, while transitions involving an odd number of photons are permitted between states with different parity. Therefore, measurement of multiphoton processes allows studies of electronic states whose excitation from the ground state is prohibited by single-photon transitions.

2.2 FS TIME-RESOLVED PHOTOELECTRON SPECTROSCOPY

Although the dynamical processes described above have been investigated using spectroscopy techniques such as absorption, emission, or fluorescence spectroscopy in simple targets, photoexcited polyatomic molecules often possess complex dynamics, mostly dominated by nonadiabatic coupling of nuclear and electronic degrees of freedom. In many cases, it leads to complex and broadened absorption spectra, making the investigation of such dynamics extremely challenging in the frequency domain. Femtosecond time-resolved methods, on the other hand, involve a pump-probe configuration in which an ultrafast pump pulse initiates a reaction or, more generally, creates a nonstationary state or wavepacket, the evolution of which is followed as a function of time by means of a suitable probe pulse. These methods offer a complementary view to spectroscopy and can usually yield a more physically intuitive picture.

Time-resolved investigation were typically based on laser-induced fluorescence or resonant multiphoton ionization, and they require the probe laser to be resonant with the targeted transition. They are therefore limited within a small region of the reaction coordinates. On the other end, photoelectron spectroscopy has been able to follow dynamics along the entire reaction coordinate due the very few selection rules required In such experiments, the probe laser generates free electrons through photoionization and the electron kinetic energy and/or the angular distribution is measured as a function of the pump-probe delay. In the following we will introduce the main concepts of this technique, employed in all the experiments reported in this work, for a full review refer to [35].

A molecular wave packet is defined as a coherent superposition of molecular eigenstates. In particular, when employing a laser pulse for the preparation of the molecular system, the amplitudes and initial phases of the wave packet are determined by the amplitude and the phase of the pump laser field $E(\omega_1, 0)$ through the transition proba-

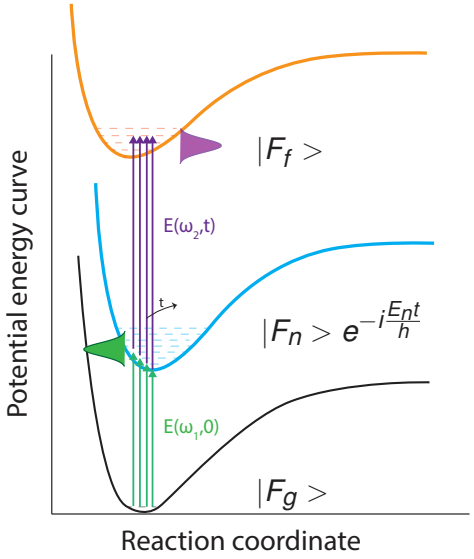

Figure 2.3: Simplified scheme of a wavepackets probing in fs-TRPES: a wavepacket or coherent superposition of excited states $|F_n\rangle$ is excited through a pump pulse ($E(\omega_1, 0)$). When the pump is over, it evolves following the initial phase relationship and the time-dependent Schrödinger equation. A second pulse $E(\omega_2, t)$, the probe, comes after a certain amount of time t favoring the transition towards a final state $\left|F_f\right\rangle$ where all the contribution will interfere.

bilities between the ground state F_g and the excited state of interest, as can be seen in Fig. 2.3. after the pump is over, the wavepacket evolves freely, according to the relative energy phase factors in the superposition. Its evolution after a certain time t is expressed by

$$|\Psi(t)\rangle = \sum_n a_n |F_n\rangle e^{-\frac{E_n}{\hbar}t} \tag{2.8}$$

where the complex coefficients a_n contain both the amplitude and phases of the exact (non-Oppenheimer) molecular states $|F_n\rangle$ and E_n represents the excited state energies. A gaussian wave packet is represented in green in Fig. 2.3. In this case, a coherent superposition of vibrational states on the blue PEC is depicted. The phase relationship is given by the a_n which are related to the electric field of the pump.

After some time t, the probe laser interacts with the wave packet projecting it onto a specific final state which we call $|F_f\rangle$. In general, the properties of the final state are fundamental to probe specific dynamics as it acts as template onto which the particular molecular state is projected. The time dependence of the differential signal $S_f(t)$ related to a single final state can thus be written:

$$S_f(t) = \left|\left\langle F_f \left| \vec{\mu}(\vec{r}) \cdot \vec{E}_{probe} \right| \Psi(t) \right\rangle\right|^2 = \left| \sum_n b_n e^{-\frac{E_n}{\hbar}t} \right|^2 \tag{2.9}$$

where we have defined

$$b_n = a_n \left\langle F_f \left| \vec{\mu}(\vec{r}) \cdot \vec{E}_{probe}(t) \right| F_n \right\rangle . \tag{2.10}$$

The signal can thus be expressed as

$$S_f(t) = \sum_n \sum_{m \leq n} |b_n||b_m| \cos\left(\omega_{nm} t + \phi_{nm}\right). \tag{2.11}$$

We note that the complex coefficients b_n contain both the amplitude a_n from Eq. (2.8) as well as the probe transition dipole moments and all the generalized vibronic overlap factors to the final state $|F_n\rangle$, where all the intermediate states are depicted in Fig. 2.3. More generally, the signal $S_f(t)$ represents a coherent sum over all pump-probe transition amplitudes which are consistent with the pump and probe bandwidth, as it implicitly contains interference terms between the transitions originating from the two pulses. In fact, the modulation of frequency $\omega_{nm} = (E_n - E_m)/\hbar$ contained in (2.11) represents the interference between individual two-photon transitions arising from an initial state, passing through different excited states, and terminating in the same signal final state. In some sense, it can be considered as a quantum beat among a multitude of states. The power spectrum of this time domain signal gives information about the set of level spacings and their respective overlaps factors with a well specific final state $|F_f\rangle$. Different final state will generally have differing overlaps. In particular,

one should consider a full set of final states $|F_i\rangle$ that fall within the finite bandwidth of the probe pulse.

It becomes therefore quite important to differentiate in between integral and differential techniques, i.e., those methods which can resolve or not the different set of final states. For instance, integral detection techniques, such as total fluorescence or total ion yield, measure a total signal which is proportional to the total population in the full set, or $\sum S_i(t)$, where S_i represents the signal relative to a single state. Differential techniques, such as photoelectron spectroscopy or dispersed fluorescence, can also resolve different contributions from different final states.

It is quite clear that the choice of the final state is of high importance as it determines the possibilities of the experimental techniques and significantly changes the information contained in the measurements. In this context, the choice of the molecular ionization continuum as the final state in these experiments has many advantages, since ionization is always an allowed process, with relaxed selection rules due to the range of symmetries of the emitted electron. Any molecular state can be ionized with the right probe and no dark states can obscure the observation of the dynamics of interest. In addition, highly detailed information can be obtained by differentially analyzing the photoelectron as to its kinetic energy and the angular distribution; at the same time the detection of the ion can provide information on the mass channel for the process. For example, in photodissociation problems, the ion-yield can be very helpful for identifying any transient species or monitoring the production of the products.

On a more practical note, charged particle detection is also extremely sensitive and many methods has been developed to measure kinetic energy and angular distributions with high accuracy. In a typical instrumental setup for gas-phase time-resolved photoelectron experiments, a skimmed neutral molecular beam interacts with pump and probe laser pulses in the interaction region of a photoelectron analyzer, which can be a time-of-flight electron spectrometer or a 2D or 3D electron imaging system.

2.3 KINEMATICS OF LASER-MOLECULES INTERACTION

Most processes described here are usually simple two-body events AB (molecular fragments) which finish with the two particles ejected in opposite directions in space with a fixed amount of kinetic energy. The total translational energy is divided between the two fragments to ensure the conservation of momentum and energy. In the case of photoionization, for instance, due to the much lighter mass, the photoelectron essentially receives all of the translation energy, while the ion appears with negligible amount of kinetic energy. On the other

hand, for a photodissociation process, the energy distribution will depends on the ratio between the masses.

In a typical experiment, each photodissociation or photoionization event yields two partner fragments with equal momenta flying in opposite directions in the center-of-mass frame. Under the same initial conditions, a second event will produce a pair of fragments flying in another direction but with the same speed. The sum of all events results in a spherical distribution in the velocity space commonly called Newton sphere. Different momenta contents will generate different spheres: the size of the sphere provides information on the internal and translational energy balance. Instead, the surface pattern of the sphere provides information about the angular distribution of the photoproducts, i.e., it represents the probability of finding the fragments preferentially ejected in certain regions of space.

The distribution on a Newton sphere is anisotropic: it is given, in part, by the direction of the transition dipole moment vector $\vec{d}$ with respect to the coordinates of the molecular system. The transition produced by the absorption of a photon of linearly polarized light takes place most likely when the light polarization vector $\vec{\epsilon_p}$ is aligned to the axis of the transition dipole moment vector $\vec{d}$. This, in turn, gives a preferential alignment to the excited molecules in the laboratory frame.

The distribution of the transition depends on the symmetry of the initial and final states: for instance, for a diatomic molecule we can considered a parallel and a perpendicular transition as two extreme situations. Parallel transitions occur when the dipole moment $\vec{d}$ is parallel to the internuclear axis of the molecule, meaning in transitions between equal symmetry states such as $\Sigma \leftrightarrow \Sigma$ or $\Pi \leftrightarrow \Pi$ transitions. On the other hand, in perpendicular transitions the dipole moment is perpendicular to the internuclear axis of the molecule, which occurs in transitions between different symmetry states ($\Sigma \leftrightarrow \Pi$ transitions).

In both cases, a general expression for the angular distribution of fragments after the excitation with a single linearly polarized photon is

$$I(\theta) = \frac{\sigma}{4\pi}\left[1 + \beta P_2\left(\cos\theta\right)\right] \tag{2.12}$$

where θ represents the angle between the light polarization vector $\vec{\epsilon_p}$ and the velocity of the fragments $\vec{v_l}$, σ is absorption cross-section and β is the *anisotropy parameter* which characterizes the shape of the angular distribution through the second order Legendre polynomial $P_2(cos\theta) = (3\cos^2\theta - 1)/2$.

For a pure parallel transition, the distribution follows $\propto \cos^2\theta$, therefore the anisotropy parameter needs to be $\beta = 2$. On the other extreme, a pure perpendicular transition will lead to the angular distribution $\propto \sin^2\theta$, which result for $\beta = -1$. The shape of the respective Newton spheres is depicted in Fig. 2.4. Depending on

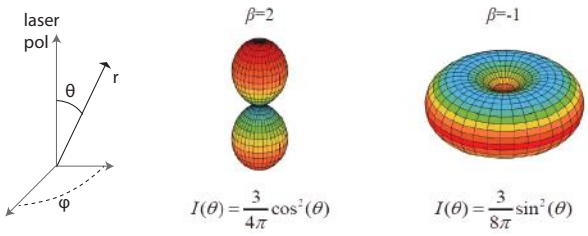

Figure 2.4: Representations of different limiting case for the angular distribution in Eq. (2.12).

the value of β it is than possible to provide information about the electronic transitions and the symmetries of the excited states.

There are many cases, even for single photon absorption in which the Eq. (2.12) does not hold for instance, for orbital angular momentum (atomic) or rotational (molecular) alignments, or particularly when a scheme of (2+1) REMPI scheme is used. Consequently, additional terms need to be included β_{2n}

$$I(\theta) = \frac{\sigma}{4\pi} \sum_{n=0}^{n=N} \beta_{2n}^{N} P_{2n}\left(\cos\theta\right) \tag{2.13}$$

where $P_n\left(\cos\theta\right)$ is the n-order Legendre polynomial. This expansion is also suitable for the cases of multiphoton processes. In most cases, these situations can be approximately studied using only the first two terms of Eq. (2.13), i.e., only two anisotropy parameters β_2 and β_4. In these cases, the two betas will also have limiting values, which is dependent on the different number of absorbed photons.

3

EXPERIMENTAL SETUP

The following chapter includes a detailed description of the instrumentation that has been used for the experiments which are described later in thesis. We will discuss firstly the light source and then focus on the molecular beam source and the charge particles detection system.

Generating few-femtosecond UV pulses stands as one of the most difficult challenges in investigating UV-induced processes in molecules on a few-fs time scale. The generation of femtosecond pulses in the UV spectral range has been achieved over the last decades mostly through non-linear up-conversion processes, normally based on crystal media due to the relatively high conversion efficiency they provide. These methods intrinsically limit the duration of the generated pulses due to high group velocity dispersion introduced showed by solids. In this perspective, a significant effort has been made in the last ten years in order to exploit low-dispersion media, such as noble gases, with the side effect of providing much lower conversion efficiency, at least two orders of magnitudes compared to crystals. For a summary of the different methods to produce few-fs UV pulses, I contributed to a book chapter, to which we refer [30]. In the following chapter, the few-fs UV generation method employed will be described in detail. The beamline in which these novel pulses are integrated will be described, a its combination with two other colors, attosecond XUV pulses and the fundamental few-cycle VIS/NIR pulses will be described.

In the second section of the chapter the double spectrometer for particles detection and the molecular source will be described. The first can detect simultaneously ions and electrons produced in the experiment: the extraction electrodes are installed in the interaction region where the molecular and the laser beam cross. On one side, electrodes accelerate the electrons on a two-dimensional micro-channel plate, coupled with a phosphor screen and the fast camera, realizing a VMI spectrometer. On the other side, negatively charged potentials are extracting the ions from the interaction region and delivered them on a second detectors. From their time-of-flight inside the spectrometer it is possible to measure the mass of the fragments produced in the photoreactions. The molecular source produces molecular beams of the sample to be investigated. It can also be used to evaporate liquid and powder samples. In the last section, the temporal characterization of the UV pulses is reported, by measuring electron kinetic energy and ions in krypton as a function of the UV-IR delay.

The beamline was developed in Politecnico di Milano and then moved in Hamburg in 2018. I contributed to its realization while

working for my master thesis in Milan, particularly focusing on the UV arm. Once in Hamburg, I contributed extensively to re-build it and operate the beamline in Hamburg. I designed and implemented the upgrade with Si-mirrors instead of dielectric separators. I also worked on the pulse characterization in Krypton, by running the experiments, analyzing, and interpreting the data.

3.1 LIGHT SOURCES

A commercial multi-mJ Ti:Sapphire laser system (FEMTOPOWER PRO V CEP) by Spectra Physics seeds the beamline. The system provides an output of 10 mJ energy per pulse at the repetition rate of 1 kHz with a duration of 25 fs centered at a carrier wavelength of 800 nm and it delivers Carrier Envelope Phase (CEP) stable pulses [36].

Briefly, this quantity measures the phase difference in between the carrier oscillation of the electric field and its pulsed envelope. This is an essential property to produce isolated attosecond pulses, in which the relative phase in between the carrier and the envelope strongly affects the XUV spectrum and, consequently, the temporal profile of the generated pulses [37].

The laser system is composed by a two-stages amplifier seeded by a CEP stable oscillator.

The oscillator (Synergy, Spectra Physics) provides broad pulses - around 80 nm bandwidth, circa 8 fs transform-limit - at a repetition rate of 75 MHz and it is CEP stabilized by a second unit (CEP_4) which measures and feedback the CEP using a collinear f-to-2f setup [38]. In respect to previous systems, the feedback is realized through an Acousto-Optic Modulator (AOM) outside the oscillator cavity. The CEP stable pulses are amplified in the following two consecutive stages (pre-amplifier and booster) using the Chirped Pulse Amplification scheme [39]. In particular, the pulses are stretched of about three order of magnitude and amplified first through 10 passes in a first Ti:sa crystal optically pumped by a Q-switching laser. After the 4-th pass, a second AOM (Dazzler, from Fastlite) is used to pre-compensate high-order dispersion and the shape of the outgoing spectrum, in order to reduce the effect of gain-narrowing in the amplified spectrum. In addition, a Pockels cell selects a single pulse from the MHz pulse train. A second Ti:Sa crystal, pumped by a second laser realized the second, single, stage of amplification (booster), delivering more than 14 mJ per pulse which are reduced by 80% in the transmission grating compressor, which recompress pulses down to 25 fs duration at the output.

A second f-to-2f system works as a second stabilization loop for the CEP, correcting for any residual CEP noise present introduced by the amplifier. The final output of the laser shows a CEP root-mean-square (RMS) of 200 mrad over several hours of operation.

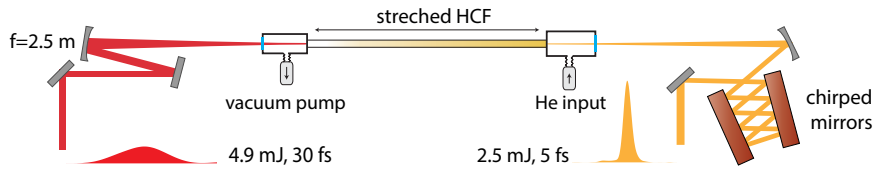

Figure 3.1: Scheme of the pulse compression in a stretched hollow core fiber. The output of the laser is focused by a focal mirror $f = 2.5\,\mathrm{m}$ in a stretched hollow core fiber filled with Helium/ The gas is injected from the output (around 1.4 bar) and pumped from the input, to realize a pressure gradient. The SPM-broadened laser is then compressed with multiple bounces on a pair of chirped mirrors in a V-shape configuration.

Roughly 60% of the main output is sent to a hollow-core fiber setup for pulse compression.

3.1.1 *Hollow-core fiber compression*

In order to generate few-femtosecond UV pulses through Third-harmonic generation, a 25 fs duration is not enough: being a direct third-order process, the estimated duration of a UV pulse through THG would be $1/\sqrt{3}$ shorter than the driver, which for a 25 fs will result only a 14 fs duration [30]. Driving generation employing a few-fs infrared pulse is then needed to achieve few-fs UV pulses.

For this reason, further temporal compression is performed through Self-Phase Modulation (SPM) in hollow-core fiber (HCF) filled with noble gas [40].

The spectral broadening induced by SPM originates by a third-order Kerr effect due to the dependence of the non-linear refractive index $n_2 = n_0 + n_2 I(t)$ on the intensity I of the laser. This produces, after propagation in the medium of length L, new frequencies proportional to the slope of the intensity temporal profile as $\omega_i = \gamma(\partial I/\partial t)L$. Due to the rising and trailing edge of the pulse - these frequencies are above and below the carrier, increasing the bandwidth of the input laser. Because each frequency component is produced at a different time, the resulting spectral content of the pulse will inherently exhibit a linear chirp, which need to be compensated afterwards, usually employing dispersive optics such as chirped mirrors [41].

Fig. 3.1 shows a scheme for the HCF setup used in all the experiments of this thesis. The laser pulses are loosely focused in a fused silica 400 µm-diameter hollow-core stretched fiber. The laser is focused through a focal of 2.5 m to achieve a spot size of 260 µm beam-diameter, correspondent to 64% of the fiber core diameter, optimizing the coupling efficiency. A near-field/far-field two points beam pointing stabilization system (Aligna, Messtechnik GmbH) is

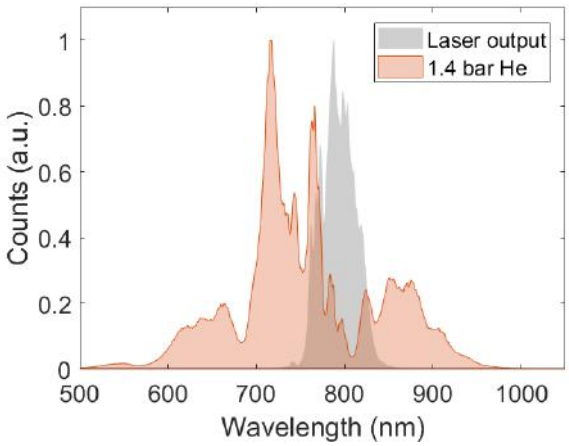

Figure 3.2: A typical spectrum (red) obtained by spectral broadening in our stretched HCF from 5 mJ, 25 fs duration (in input laser (in grey), obtained by injecting 1.4 bar of helium in a pressure gradient configuration. The transform limit of this spectrum is 4 fs.

used to avoid damage at the fiber input, due to the high intensity of the focused laser. Furthermore, for the high intensity, the fiber is embedded in a vacuum system in which the laser enters, through an anti-reflective coated window, much before (1.5 m) the actual focus and fiber tip. This assure that no non-linear self-focusing effect can occur in air, leading to coupling mismatch.

Additionally, self-steeping or ionization can also affect the temporal properties of the compressed pulses. Therefore, SPM is achieved with a pressure gradient configuration by injecting gas at the exit side of the fiber and pumping at the entrance side. In this way, diffusion through the capillary leads to a reduced gas density at the input, minimizing undesired effects where the intensity is highest. The disadvantage is that longer fibers are required in order to acquire the same non-linear phase term. To this aim, we note that the production of straight rigid capillaries longer than 1 m is challenging. In particular, it has been proved that the straightness of the capillary is crucial to achieve the best transmission inside the waveguide, since in HCF the guiding properties depend more on grazing incidence $n_{gas} < n_{glass}$ rather than total internal reflection $n_{core} > n_{ext}$ [42].

To solve this issue, a mechanically stretched flexible fiber can be used as an alternative. It has been shown to provide good transmission even for very long fibers, since its straightness is virtually independent of the fiber length [43]. The fiber used in our lab is a commercial system (few-cycle Fiber) and has a length of 2.3 m and allows a total transmission of around 50% when injecting 1.4 bar of helium. A typical broadened spectrum is shown in red in Fig. 3.2.

The spectrum normally extends from 500 nm to 1000 nm and it is centered at a carrier wavelength of 750 nm, covering almost one

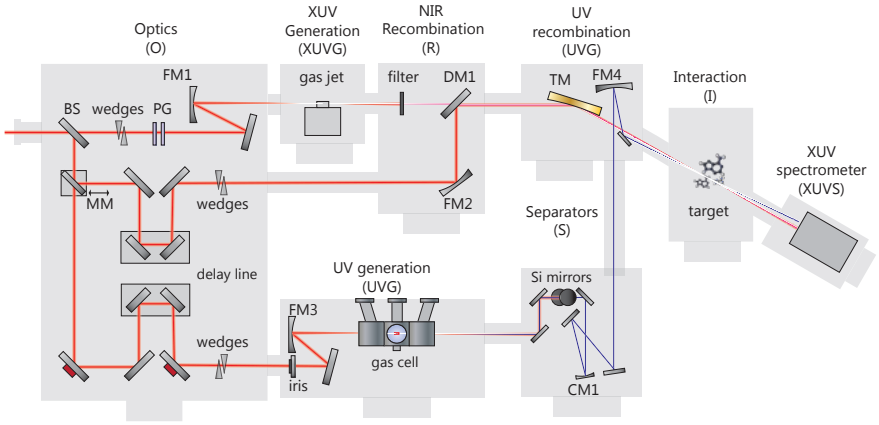

Figure 3.3: Schematic representation of the STARLIGHT beamline. See text for details.

octave. In respect the input laser spectrum, reported as the grey area, the carrier is blue-shifted from 800 nm of almost 50 nm and, in general, we observe more broadening for the blue part of the spectrum. Since pure SPM should lead to symmetric spectra, an asymmetric broadening indicates that other non-linear effects such as self-steepening or ionization cannot be entirely suppressed.

Nevertheless, compression down to 4.5 fs duration is achieved through 10 reflections on a pair of chirped mirrors (Few-cycle) in a V-shaped configuration, as measured in a home-built non-collinear SH-FROG (Frequency-resolved optical grating) [44]. These pulses have been used to seed the attosecond beamline described in detail in the next section.

3.1.2 *Beamline overview*

The STARLIGHT (STeering Attosecond electRon dynamics in bio-molecules with UV-XUV LIGHT pulses) beamline provides light for all the experiments which are included in this thesis. It combines few-fs UV pulses with isolated attosecond pulses in the XUV spectral range or alternatively with few-cycle VIS/NIR (NIR from now) pulses with the possibility of performing pump-probe experiments with very high temporal resolution.

The beamline consists in six interconnected high vacuum chambers as represented schematically in Fig. 3.3. High vacuum is required for two main reasons: firstly, XUV radiation is strongly absorbed and dispersed by air. Secondly, while absorption in the UV spectral region is negligible, the second order dispersion introduced by air is substantial, in particular when pushing the duration to few femtoseconds. Furthermore, charge particle detection in the double spectrometer also requires high vacuum environment.

The beamline follows an interferometric approach. The fundamental NIR pulse, described in sec. 3.1.1 is split in the first Optics (O) chamber by a broadband 1 mm thin beamsplitter (BS). Depending on the experiment, the BS can vary in order to obtain different ratio, ranging from 70% reflection when generating XUV to only 5% when favoring UV generation, as it has been used during the experiments.

The reflected beam is used in the top arm for the generation of isolated attosecond pulses through High Harmonic generation (HHG), a highly non-linear processes obtained by focusing an intense laser in a gas target. The XUV beam goes through a metallic filter, which filters out the co-propagating residual NIR pulses, and through a drilled mirror (DM1) used for the recombination with the NIR probe. Then, it is refocused in the interaction region (I) by a gold-coated $150x20x15$ mm toroidal mirror at grazing incidence (5°).

The light transmitted by the BS can be sent alternatively to two different paths employing a mirror mounted on a automated positioner (moving mirror, MM) in Fig. 3.3. When the mirror is inserted, the beam is sent through a delay line (PiezoSystem Jena) and a pair of fused silica wedges for dispersion compensation and reflected by the DM1 for recombination with the XUV arm. In this way it allows the NIR pulse to be used in combination with the XUV attosecond pulses in the most typical attosecond pump-probe scheme.

Alternatively, when the moving mirror is removed, it can be used for UV generation. The beam is directed towards a second delay line and wedges pair and subsequently sent towards the UV generation chamber (UVG). UV generation is achieved by third-harmonic generation (THG) in a highly-pressurized gas cell which will be presented in detail in 3.1.3. Afterwards, the UV pulses are spectrally separated by the fundamental, by employing a pair of Silicon mirrors at Brewster's angle. The UV beam is collimated and subsequently refocused by a 900 mm, recombined with the XUV arm on target in a narrow-angle (<1° non-collinear geometry. The UV generation can be monitored by extracting the beam after spectral filtering employing a second moving mirror (not in figure), through which the UV pulses are sent out of chamber (S) to a UV-VIS spectrometer (Avantes) and a Optometer (GigaHertz Optik), to measure the spectrum and the power, respectively.

A third moving mirror (not in the figure) is also used to extract the pump-probe beams before reaching the interaction region. This is used for optimization of the spatial and temporal overlap of the arms in use by observing the two foci using a CCD camera.

Finally, a very compact XUV spectrometer, based on the combination of a of a spherical varied-line-space grating and a cylindrical mirror, is used to record the XUV spectrum simultaneously during every experiments.

3.1.3 *UV generation in gas*

For the generation of femtosecond UV pulses, multistage non-linear up-conversion schemes are usually employed, combining the SHG of a 800 nm with sum-frequency generation to obtain the third harmonic of the driving field [45]. The possibility of achieving better phase-matching condition in 2nd-order non-linear crystals results in better conversion efficiency than direct THG [46]. The choice of bulk media, however, poses a strong limitation in the shortest duration of the generated pulses, mostly due to high GDD introduced during propagation in the non-linear crystals and the very large phase-matching bandwidth required. Due to the absence of suitable negative dispersive mirrors in the UV, complex dispersion compensating schemes have been applied in order to reach the sub 10 fs duration [47, 48].

Using gas as non-linear medium allows for other non-linear processes to be employed, such as four-wave mixing in filamentation [49] or cross-phase modulation in waveguide [50]. More recently, the very promising dispersive wave emission in hollow-core fibers [51] has been demonstrated. In 2019, we have demonstrated sub-3 fs UV pulses generation using THG [31]. With the goal of the shortest temporal duration, the almost dispersion-free properties of noble gas make them the most suitable to the task, even at the expense of a much lower conversion efficiency. In order to compensate for the for low efficiency, high pressure gas cells are employed in our setup to increase the number of emitters density in the medium. In the following section we will describe the technical details of the generation setup, while in section 3.3.2 we will discuss about the properties of the generated UV pulses.

3.1.3.1 *Micro-machined gas cell*

In the UV generation chamber from Fig. 3.3, a focal 500 mm focused the driving NIR pulses into a micro-machined fused silica cell, which is shown in Fig.3.4. The cell is produced by a $20x5$ mm fused silica slab, in which a portion is reduced to 3 mm width, in which a channel is produced for laser propagation. The shape of the channel can be controlled very precisely with µm precision through the use of FLICE (Femtosecond Laser Irradiation followed by Chemical Etching) for the manufacturing of the cell. In particular, on the long side of the channel a 3 mm diameter hole allows the connection to a same size metallic tube providing the gas. Instead, the entrance and exit consist of gradually reducing cone-shaped size up to 400 µm to contain the gas in a limited volume and reducing the outflow. The cell itself then acts as a large 3 mm long reservoir of gas for THG. In any case, due to the need in working in high-vacuum, the cell is integrated into a differential pumping system.

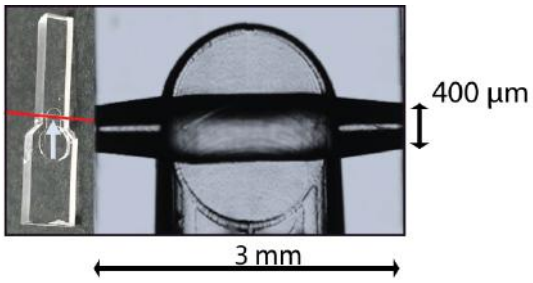

Figure 3.4: Picture of the high-pressure fused silica cell for THG. (a) Left: The red line indicates the laser propagation direction while the white arrow shows the gas flow. Right: A magnified image of the 3 mm long channel acquired with a microscope. The extremities of the channel are reduced in a conical shape with a 400 µm exit aperture in order to reduce the out-flowing gas. Adapted from [31].

3.1.3.2 *Differential Pumping*

To ensure the high-vacuum in the rest of the beamline, the glass cell is placed into a differential pumping system consisting of three sub-chambers, as can be seen schematically in Fig. 3.3 in UVG chamber and more in details in Fig. 3.5. The glass cell is installed in the central cubic section which is connected on the other side to a pump that collects most of the out-flowing gas. The residual gas flows towards two lateral same size chambers through 0.8 mm aperture, which are realized through thin plates that can be easily installed at the interface between the different cubic sections. Similar plate with 1 mm diameter is installed at the interface between the lateral sections and the main vacuum chamber. Each section is heavily pumped through bellows connected to the wall of the main chamber: the central section is pumped by a roots pump of 55 m^3/h which evacuates most of the gas, while a second pump is split in between the two lateral chambers, where the gas density is lower. Additional small-diameter apertures are also installed at the interface between UVG chamber and the Optics chamber, as well as between UVG chamber and the separators chamber, to further reduce the outflow of gas in the beamline. The differential pumping scheme effectively confine the gas only in the region of interest, allowing, for example, the UVG chamber to be in low 10^{-3} mbar level and the separators chamber even at 10^{-5} mbar while injecting up to 8 bar of neon in the cell. However, due to the high consumption (2 bar L/min when operating with 1 bar of argon), the setup has also been equipped with a gas recirculation circuit.

3.1.3.3 *Recirculation system*

The circuit which takes care of the recirculation of the gas is shown in Fig. 3.5. the exhaust of the roots pumps are connected to a diaphragm compressor. In order to collect also the residual gas outflowing in

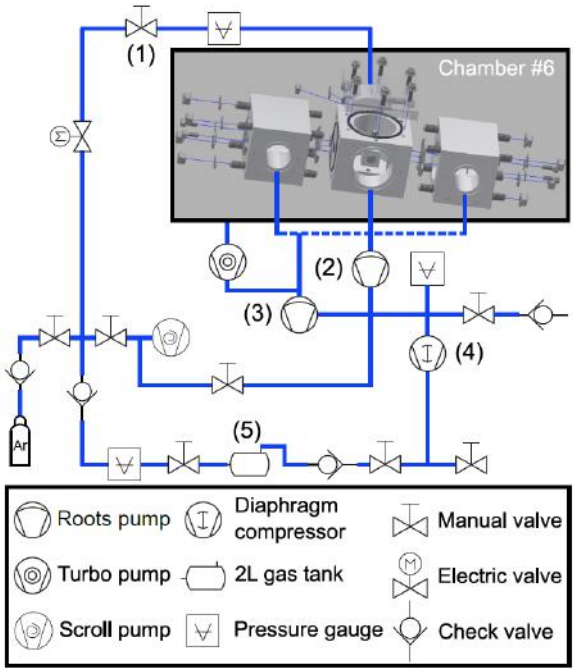

Figure 3.5: Differential pumping setup and recirculation system. (1) manual valve for gas injection in the THG cell, installed in the central section of the cubic differential pumping system (also in figure). (2) and (3) indicates the roots pumps connected to the central and lateral sections of the differential pumping system, including also the gas collected through the turbo. The diaphragm pump (4) compresses the collected gas inside the a 2 L tank (5). Afterwards it can be sent to the manual valve (1) for the generation process. Different valves and pressure gauges are also indicated in figure.

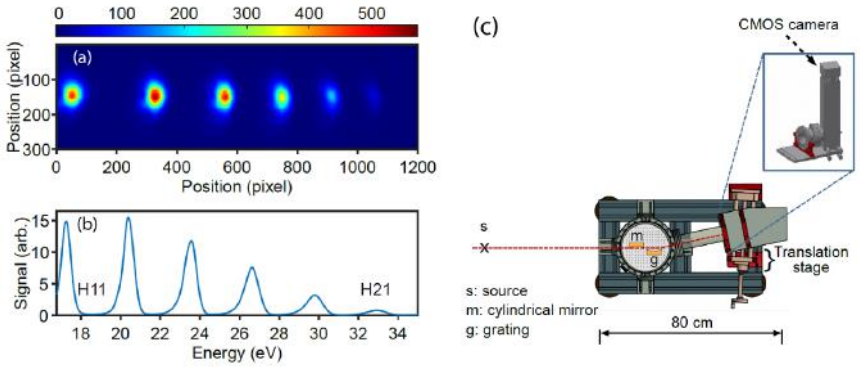

Figure 3.6: High-harmonic generation spectrum obtained in krypton with 0.6 mJ, 5 fs pulses at 780 nm. (a) Raw image showing the spatial profile of the different harmonics. (b) Corresponding spatially integrated spectrum, with energy calibrated axis. Harmonics from 11 to 21 are observed. (c) Top view of the compact XUV spectrometer. The source point is only 750 mm far from the cylindrical mirror, which is combined with a SVLS grating to image the XUV radiation spectrum on a MCP + phosphor screen. The image is collected by a mirror placed at 45° and recorded by a camera. The detector can be translated to acquire a full spectrum.

the chamber, also the exhaust of the backing pump of the turbo is included. The collected gas is then compressed into a 2 L tank to a pressure up to 7 bar. Check valves are placed before and after the tank to assure the right flow direction and to send the compressed gas back to the UV generation cell. Test performed with 1 bar of argon have shown that this system allows for 96% initial pressure to be preserved, which allows, for instance, an operation over 37 h while consuming only 1 L of gas.

3.1.4 *XUV generation*

The first arm - obtained by the reflection of the BS in Fig. 3.3 - is designed for XUV attosecond pulse generation. The NIR pulses are focused by a 700 mm focal silver mirror into a 6 mm channel for HHG. The interaction channel is mounted on motorized actuators, with the possibility of moving three translations and one rotation (Physik Instruments) for better alignment. The gas is provided into the interaction cell by a water-cooled pulsed valve (Attotech) which is synchronized with the laser at 1 kHz. The opening time of the valve is typically adjusted from 120 µs to 150 µs, employing a backing pressure between 1 and 2 bar. Argon, krypton and xenon can be alternatively chosen for the generation, depending on the needed XUV spectral range. In 3.6 a typical XUV spectrum generated in krypton is shown. The spectrum extends from harmonic 11th up to harmonic 21st, with a total photon energy ranging from 17 eV to 33 eV. It has been measured

employing a newly designed compact XUV Spectrometer.

XUV spectrometers usually consist of a grazing-incidence mirror focusing the light source onto a slit placed at a fixed distance from a spherical-line-space (SVLS) grating. This grating allows all the spectral components to be focused onto the same plane, rather than on a cylindrical surface, which allows the use of 2D detector [52]. In addition, the use of the slit improves the overall resolution, at the expense of the photon flux transmitted to the grating. In the case of HHG source, for instance, this limitation becomes crucial.

In most HHG experiments, however, the XUV light is refocused by a grazing-incidence toroidal mirror into an interaction point. If the toroidal mirror acts with a 1:1 refocusing magnification factor, the XUV focus presents minimal aberrations, which makes the use of the slit unnecessary when the spectrometer is placed at a distance which matches its entrance arm . Nevertheless, this scheme usually requires an additional toroidal mirror to refocus 1:1 the interaction point, due to the relatively short entrance arm acceptance of the gratings (350 mm) which would limit the space for large-footprint experimental setups when put directly after the interaction point [53].

An improvement of this scheme, in which we increased the compactness while keeping a long entrance arm, is shown in 3.6 (c). We combined a SVLS grating (Hitachi) with a convex (divergent) gold-coated cylindrical mirror. It is used to create a virtual image of the XUV focus at the source point of the grating, while keeping a relatively long arm. The gold-coated grating has 5649 mm radius of curvature and a central groove density of 600 lines/mm and it provides a flat spectral plane at 469 mm, where a 40 mm MCP detector and a phosphor screen (Photek) is installed. The detector is placed on a translation stage to acquire the full spectral plane. Since the cylindrical mirror does not focus the sagittal direction, the spatial profile of the harmonics can be monitored along the vertical axes and used to measure its divergence. The images are then recorded by a CMOS camera (Hamamatsu), which is mounted perpendicularly to reduce the spectrometer footprint even more. The total length of the instrument is about 80 cm.

3.2 PARTICLE DETECTION AND MOLECULAR SOURCE

Having described all laser sources one can produced in STARLIGHT, all beams discussed until now are combined in the interaction region in Fig. 3.3. In this region, several detection and molecular source schemes can be installed, depending on the particular experiments to perform. For most of the experiments described in this thesis, we have employed a continuous molecular source, interfaced with a double sided spectrometer, which combined an electron VMI together with

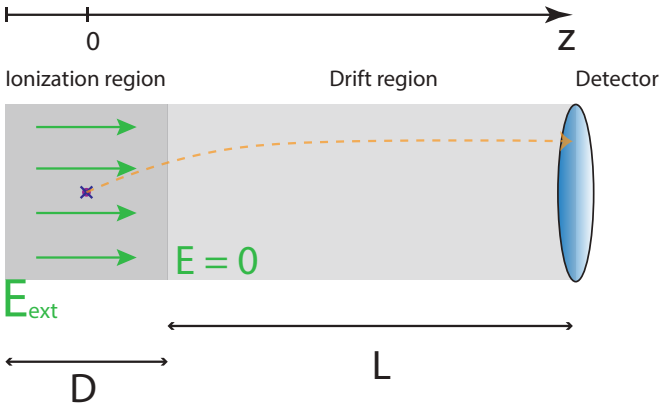

Figure 3.7: Scheme for one-dimensional charged particle spectrometer: the charged particle is produced in the purple spot in the ionization region at $z = 0$. A static external electric field E_{ext} is applied, to accelerate the charged products. In the simplest case, the detector can be put at distance $D/2$ from the origin, or after a drift region without electric field, to increase the resolution. The m/q is measured through the time t it takes to travel in the spectrometer.

an TOF mass spectrometer. We will briefly mention the most basic devices and then we will describe in detail the one employed in this work.

All particles that are charged can be accelerated towards the detectors with the use of electric fields. Specifically, measuring the *time-of-fight* (TOF) which occur in between the ionization event and the arrival on the detector allows to measure either the mass or the kinetic energy of the particle. In addition, if the detectors are able to record also the impact position, under certain assumptions the full 3D momentum distribution can be reconstructed and the angular distribution of the photoproducts can be measured.

One-field spectrometers realizes the first and most simple configuration: assuming the ionization happens at $z = 0$, as depicted in Fig. 3.7 - usually where the molecular beam intercepts the laser beam, a static strong electric field is applied parallel to z which extracts the particles and sends them to a detector at a distance D.

In case of a strong electric field E_{ext}, the initial p_z velocity of the particle can be neglected, resulting in $t = \sqrt{2mD/qE_{ext}}$, in which the TOF will depend only on the mass over charge ratio m/q. However, to access the kinetic energy distribution, one could use weaker field and access p_z as perturbation of t. Additional field-controlled regions can be added in cascade in order to enhance the control over the dispersion of the time-of-flight. For instance, drift tube - a region with no external field - of specific length allows for taking into account the finite size of the ionization region, known as axial-space focusing.

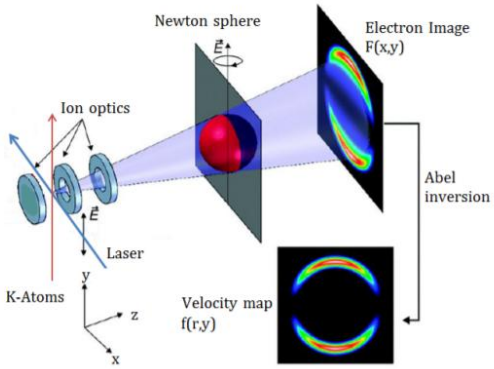

Figure 3.8: Working principle for a VMI spectrometer.

For ions with very high kinetic energies, also the introduction of a decelerating field can be considered.

In general, it is also possible to access the transversal momentum p_x and p_y by recording the position of the impact on the detector. If all the accelerating field are parallel to z, the transversal momentum is preserved. If x_0 is the ionization coordinate, the momentum can be readily measured from $x = x_0 + tp_x/m$ (the same for the y component). In these conditions, the transversal energy resolution will strongly depend on the ionization region size. The resolution therefore can be drastically improved when an inhomogeneous electrostatic lens is applied after the extractor: for instance, a set of two electrode rings put to a repulsive potential. Particles starting closer to the electrodes are deflected more towards the center, so that the same final x is reached, allowing for the transversal energy measurement to be independent on the specific ionization starting position.

This configuration has been developed by Eppink and Parker, improving on previous ion imaging technique, and is called Velocity Map Imaging (VMI) [54]. A typical VMI experiment is depicted in Fig. 3.8: a collimated molecular beam propagates along the direction y and interacts with the laser beam, whose polarization axis ($\vec{\epsilon_p}$) is parallel to y and the detector, oriented as the xy plane.

After the neutral molecular beam is ionized by the laser, the fragments are ejected in opposite directions so that the total translational energy is divided between the fragments - ensuring the energy and momentum conservation. For each event, each molecules generates fragments with same speed but different directions, resulting in a spherical distribution in space, with certain anisotropy.

The charged particles are formed between the electronstatic lens system which usually consists of three plates: from left to right in Fig. 3.8 Repeller (R), extractor (E) and lens (L). The first two electrodes produce the extraction field, accelerating the photoproducts to the detector along the direction z. The voltage ratio between repeller and

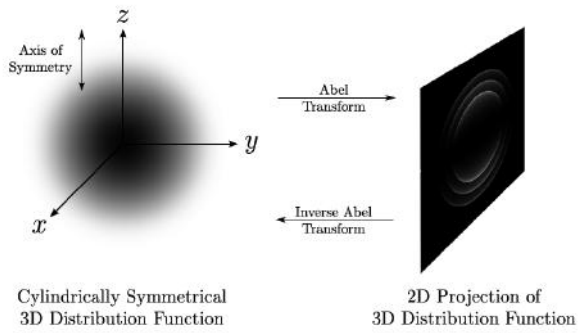

Figure 3.9: Schematic representation of the three dimensional velocity distribution $I(x, y, z)$ of fragments with cylindrical (spherical) symmetry around z axis and its projection $P(x, z)$ in bi-dimensional plane.

extractor must be properly chosen ($V_E/V_R = 0.71$) so that fragments with the same transversal velocity are focused on the same position of the detector independently on their region of formation. The lens is normally grounded, producing the acceleration of the ionized spheres towards the field-free zone, where the particles fly with constant speed and can be differentiate by their different time-of-flight. This can be used to make a selective detection - based on masses - through gating the detector.

The spatial distribution of particles measured by the detector is the projection of a three-dimensional object onto a plane. This means that, for example, photoelectrons emitted with momentum parallel to z will alter the measurement of the transversal component - resulting in a smaller radius in the image. To extract relevant information about the event, a method that allows the reconstruction of the three-dimensional distribution of particle speeds must be applied. The most common of this method or *Abel inversion* assume that, if the original 3D distribution has cylindrical symmetry, then its two-dimensional projection on a plane containing this axis includes enough information to reconstruct the original unambiguously. This condition is ensured, provided that the polarization direction is parallel to the detector plane. Under this condition, the velocity distributions on the cuts of Newton sphere by planes containing the z axis are equivalent. Consider the geometry represented schematically in Fig. 3.9. $I(x, y, z)$ represents the three-dimensional distribution and $P(x, z)$ is its bi-dimensional projection on the detector plane, i.e. xz. Due to the symmetry, we can define the cylindrical radius $\rho^2 = x^2 + y^2$ upon which we can include the x and y dependence $I(\rho, z)$. Mathematically, this projection is called Abel transform and is given by

$$F(x, z) = \int_{-\infty}^{\infty} \frac{I(\rho, z)\,\rho}{\sqrt{\rho^2 - x^2}}\,\mathrm{d}z \tag{3.1}$$

This expression can be easily inverted to obtain

$$I(\rho, z) = -\frac{1}{\pi} \int_{\rho}^{\infty} \frac{\partial F(x, z)}{\partial x} \frac{\mathrm{d}x}{\sqrt{x^2 - \rho^2}} \tag{3.2}$$

which can directly be applied to retrieve the three-dimensional distribution. However, solving (3.2) is not easy due to the singularity of the function $x^2 = \rho^2$ and, applied to experimental images, the fact that the derivative magnifies the noise. Because of this, several mathematical procedures have been developed to better perform the inversion. Among the most recent methods, it is worth mentioning the basis set expansion (BASEX) method [55] and its evolution, the basis set expansion in polar coordinates (pBASEX) [56] and - with a different choice of basis the (rBASEX) method [57]. In each of these methods the data of the projection is expanded in a suitable basis set of functions that are analytical projections of functions similar to Gaussian in the three-dimensional space, avoiding the problem of singularities. The coefficients of this expansion directly provide the information that is required for the reconstruction of the initial 3D distribution.

3.2.1 *Double spectrometer*

The possibility of detecting different particles simultaneously is crucial for photoionization experiments of complex molecules, in particular with the interest of correlated electrons dynamics. In UV pump - XUV probe scheme, for instance, single photon absorption of the XUV has the highest cross-sections, which results in the emission of many electrons for laser shots. The resulting electron VMI images can be hard to interpret, especially if the target is a large molecule (masses > 100 u).

In this perspective, coincidence methods can lead easier interpretation, but their application is limited to light sources at high repetition rate, due to their constrain of single or lower event rate. Attosecond beamline employing XUV are typically limited to a few kilohertz, which would make many coincidence experiments not practical because of the long acquisition times. For this reason, the covariance of the electron VMI and the mass spectra recorded simultaneously can still provide an improved experimental understanding for the particular reaction pathways the molecules undergo. More specifically, covariance mapping expresses the correlation of specific electron distribution to specific molecular fragments detected, overall simplifying the interpretation of the underlying dynamics.

Fig. 3.10 shows the schematics of the internal components of the instruments, with electrodes and supports. The laser beam propagates parallel to the x-y plane and crosses with the molecular beam coming

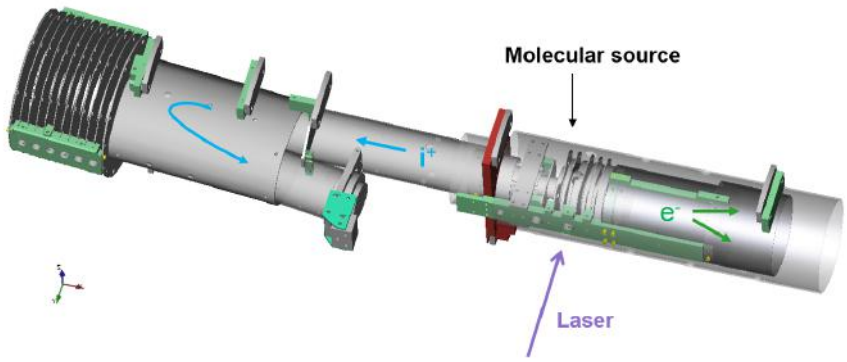

Figure 3.10: Internal schematics of the double spectrometer. The two charged particle path cross perpendicularly the laser beam (which propagates in the x-y plane). The molecular jet intersects both from the z direction. The electrodes accelerate the electrons towards a VMI, while the ions are guided in Reflectron-like mass time-of-flight in the opposite direction.

from above or z-axis. The interaction point is in between the extraction electrodes of the spectrometer, where the photo-products are accelerated along the x-axis. On the right side, electrons are accelerated and focused on a 2D MCP detector, realizing a VMI configuration. On the other side, same electrodes are pushing the produced cations in drift tube, after which additional electrodes are reflecting back the ion beam towards a second detector, which measure the time of arrival of the ions. Both these detectors are optimized to acquire single shot TOF and VMI images, with the use of a fast acquisition card (SPDevices ADQ14AC) and camera (Optronis P70-1-M-1000). As we will see in the following sections, this configuration allows a very high mass resolution and mass range(1 u over 10×10^4 u range), while keeping the real drift-tube length quite short. The total footprint of the spectrometer is only $1x0.5$m.

3.2.1.1 *Mass spectrometer*

In sec. 3.2 we have already discussed how the most basic time-of-flight detector is realized by accelerating the product particles by using a strong static parallel field towards the detector. If the particle is starting at rest, the time of flight is kinematically calculated through $t = \sqrt{2mD/qE_{ext}}$, where D is the distance to the detector, E_{ext} the constant electric field along z and m/q is the mass over charge ratio. A slightly more complex configuration is realized by introducing a field-free region of length L, called drift-tube, in which the particle will travel at constant speed $v_d = \sqrt{2DqE_{ext}/m}$, which enlarges the flight time before reaching the detector increasing the resolution.

More in general, the mass resolution of a certain time-of-flight instrument can be analyzed as the variation on the arrival time, as a function of certain parameters, in particular the spread in the ions starting position x_0 and their initial velocity v_x [58]. Since the arrival time can be expressed by the following

$$t(v_x, x_0) = \frac{1}{f(v_x, x_0)} \frac{L}{v_d} + 2\frac{D}{v_d}\left(f(v_x, x_0) - \frac{v_x}{v_d}\right) \tag{3.3}$$

where $f(v_x, x_0) = \sqrt{1 + v_x^2/v_d^2 - x_0/D}$ express the main dependence on the starting velocity and offset starting position, t increase the mass resolution, the $\partial t/\partial x_0$ and $\partial t/\partial v_x$ should be minimized.

In a common experiment, the range of different starting positions is dependent mainly on the intersection in between the optical beam width (or Rayleigh range) and the molecular beam width. When the ion starts closer to the extracting electrodes, it will need less time to reach the drift tube, a condition which we define as negative dispersion in x_0. At the same time, the same ion will also start at a lower electrical potential, which means that it will gain less acceleration and will be travelling more slowly in the drift tube. This condition is called positive dispersion. These two contributions can be made to compensate each other by choosing specific length ratio between D and L : for instance, in a simple geometry, the Wiley - McLaren condition $L = 2D$ cancels out completely the deviation due to a spread in x_0. A particular choice of length ratio in between the extracting and drift regions can therefore minimize the overall dispersion of the ions. This has a large effect in particular for cold ion (where the spread to v_x is intrinsically minimized) where it can enhance the resolution from 100 u up to 10×10^4 u [59, 60].

On the other hand, the dispersion attributed to the initial kinetic energy v_x is originated mostly from thermal energy in the sample and the kinetic energies content in the fragments due to photodissociation. In the first case, it can be reduced by employing molecular beam techniques for gas-expansion into vacuum or the use of buffer atomic gas. Employing cold molecular beam reduces most of the effects and it is easily achievable when investigating simple molecules. Significantly higher kinetic energy is carried by the ions in the case of photodissociation. In such cases, higher extraction voltages need to be employed, in order to minimize the v_x/v_d ratio in Eq. (3.3). An additional solution could be to design a longer drift tube L: in particular, the condition $L \gg D$ assure that in Eq. (3.3) the first term becomes dominant and therefore the arrival time will not depend strongly on v_x.

The two cases described above show that different length ratio L/D are needed to minimize different aspects of the instrument, in particular resulting with conflicting conditions. In addition, since a velocity map imaging spectrometer for electrons is needed on the opposite side of the mass spectrometer, the shared extraction region is

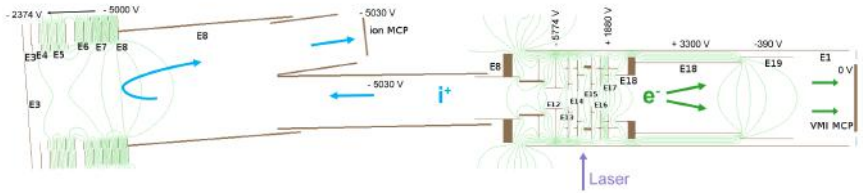

Figure 3.11: Double spectrometer schemes with particles path, electrodes and laser propagation direction. The interaction region is in between E14 and E15. Ion extraction occur at electrode E12, while reflectron is composed of electrodes from E3 to E8. Electrodes E16 and E17 acts as extractor for electrons, which are decelerated by E18 and E19. Only a few example voltages are indicated here.

also constrained in size and voltages to produce high resolution VMI images.

The best way to achieve both the conditions is to insert a *reflectron* where ions are decelerated and reflected by a set of electrodes as seen in Fig. 3.7 (blue arrows). The reflectron introduces an additional electrical field E_{refl} in the expression (3.3), which can now be written

$$t\left(v_x, x_0\right) = \frac{1}{f\left(v_x, x_0\right)} \frac{L}{v_d} + 2\frac{D}{v_d}\left(\left(1 + \frac{2E_{ext}}{E_{refl}}\right) f\left(v_x, x_0\right) - \frac{v_x}{v_d}\right) \quad (3.4)$$

The presence of an additional term allows additional control over the time of arrival: in particular, it can be used to minimize the spread due to different starting positions even when using long drift tubes, to minimize both $\partial t/\partial x_0$ and $\partial t/\partial v_x$.

Normally for spectrometers with long drift tubes, electrostatic lenses are required to keep the transverse collimation of the ion beam. Due to the low density of our sample, however, one would like to avoid the use of grids to make the fields parallel in order to maximize the transmittance of each electrode. In this picture, the reflectron can be used additionally to collimate the ion beam towards the ion MCP and allows its usage without grids.

Fig. 3.11 represents a simplified scheme of the double spectrometer, where one can observe the different electrodes for both the ions and the electrons side.

In terms of ions, a very strong field is needed to extract them form the interaction region - in between electrodes E14 and E15. In the figure also the 6 electrodes which constitute the reflectron are visible on the left side. The inhomogeneous field created slows down the ions and send them back to MCP, from which we measured the time-of-flight signal.

3.2.1.2 *Electron velocity map imaging*

As discussed more generally in 3.2 a Velocity Map Imaging spectrometer is basically a device which accelerates charged particles, in our

case electrons, towards a 2D detector. From the position of impact on the detector, one could estimate the transversal momentum possessed by the electrons when it is emitted. More precisely, if the detector is oriented in the yz plane, an inhomogeneous electrostatic lens is applied after the extraction field in order to focus all electrons with the same initial velocity to the same position (y, z) on the 2D detector independently of the position in which they are generated.

Normally, this condition is realized by the use of three electrodes, named repeller, extraction and ground (see Fig. 3.8). The first electrode is normally flat, while the others are ring shaped, which allows the electrons to pass through. The interaction region where the electrons are generated is in between the repeller and the extractor. In order to accelerate the electrons towards the detector, both repeller and extractor are put to negative voltages (positive in case of ions) with the first put to the lowest. The last electrode is instead grounded, which allows the electrons to travel field-free towards the detector. A specific ratio in between the repeller and extractor voltages realizes a particular configuration in which the electrons beam is focused, mapping each initial transversal velocity to a different position of the detector. The first application of velocity map imaging was performed using this configuration [54].

Indeed, a flat repeller cannot be used if both ions and electrons need to be collected. Therefore, this simple design for the VMI cannot be use in our case and we require a more complex configuration of electrodes as can be observed in Fig. 3.11, right side, where many more than 3 electrodes are present. Basically, the electrodes in between E12 and E16 are tuned in order to attain an almost parallel field in the interaction region to acts as an extractor. Since the ions and electrons possess very different kinetic energies, this is not applied directly at the interaction region, but the extraction region is extended in between the electrodes from E12 to E17. In particular, due to high voltage required to accelerate the ions towards the left side, a very high potential up to 20 kV would be needed for the ground electrodes to focus the electrons. In order to keep all the voltages in a reasonable range (up to 6 kV), additional electrodes are used to realize the VMI condition: in particular, E18 and E19 acts as decelerating field which allows reasonably good resolution for electrons with kinetic energy up 30 eV, which is the kinetic energy expected when ionizing molecules with our attosecond pulses. We note that VMI energy resolution is somewhat worse than what one would get with the common repeller, extractor and ground design. The current electrodes configuration acts then as a compromise in being able to detects both particles at the same time.

3.2.1.3 *Covariance mapping*

For photoionization experiments of complex molecules, the requisite of measuring both produced ions and electrons is fundamental for a clear understanding of the underlying dynamics. In particular when using XUV attosecond pulses, many fragments of the molecule are produced in the process. The corresponding photoelectron spectra is therefore very complex, since it will be the sum of all fragments' contribution. In this sense, correlation method can be used to elucidate which fragment correlates with a specific kinetic energy electron, indicating the specific ionization event or, in other words, the particular fragmentation path.

We should distinguish in between two main correlation techniques: coincidence and covariance mapping, which are both based on the broad statistical concept of covariance. In photoelectron - photonion coincidence, the detection of a much faster electron provides the start time from which the TOF of the subsequent fragment ions is measured. When used together with a pulsed laser, this will produce the required photoelectron-photoion coincidence map, which gives information about electrons and ions pair produced per each event. For this specific reason, coincidence techniques are able to produce clean maps only when the counting rate is low enough that the probability of more than one event occurring within the specific TOF window is negligibly small. Experimentally, this means that no more than one molecule needs to be ionized in a given laser shot. Any extra event will ruin the map by creating a background of false coincidence. This strong requirement makes this technique not suitable for kHz laser based setup, since it increases the acquisition time for each experiment dramatically and it will require to reduced laser intensities very low, which makes its application not very sustainable with these systems.

Nevertheless, it is relatively easy with lasers (and even more with the high flux Free Electron Laser) to end up in the complete opposite condition where many events are produced for a single event. Covariance mapping is based on this condition. Basically, covariance mapping looks at correlation in between two random variables [61]. In the contest of photoionization experiment, our variable will be a function $\mathbf{X} = \{X_n\}$ of the energy, i.e., a electron kinetic energy spectrum. $\mathbf{X}$ represents a collection of n spectrum, one for each shot acquired. Mathematically, if we consider two sets of variables $\mathbf{X}$ and $\mathbf{Y}$, the covariance matrix can be calculated by

$$\operatorname{cov}(\mathbf{Y},\mathbf{X}) = \langle (\mathbf{Y} - \langle \mathbf{Y} \rangle)(\mathbf{X} - \langle \mathbf{X} \rangle) \rangle = \langle \mathbf{YX} \rangle - \langle \mathbf{Y} \rangle \langle \mathbf{X} \rangle \tag{3.5}$$

where

$$\langle X \rangle = 1/n \sum_{i=1}^{n} X_n \tag{3.6}$$

The first term of Eq. (3.5) is a measure of how often the variables are correlated. This term, or matrix, includes also many events that

are not really correlated, and therefore needs to be corrected by the second term, which measures how often both variables are observed to be independent to each other, and therefore might cancel out the false covariance. In terms of photoionization experiments, all positive value in the covariance matrix represents correlation in between two variables - i.e. different region of the electron spectrum or part of the electron spectrum and a particular fragment in the mass spectrum. In addition, also the area under each correlated island encodes the probability of that correlated channel, per shot.

False covariance can occur also because of some change in experimental condition which favors particular channel. For instance, laser intensity fluctuations or a change in the target density, time jitter in FEL can always induced these indirect correlations which needs to be corrected in order to obtain clean covariance maps. Methods such as partial covariance aim at estimating this false covariance with the use of additional fluctuating parameters which can be used to measured and subtract the false correlation from the covariance map and undisclosed the correlations coming from the target [62].

3.2.2 *Molecular source*

Molecular sample is introduced in the experimental chamber in Fig. 3.10 from the top. Fig. 3.12 includes a scheme of the molecular source itself.

The source is composed of a service chamber or cross, which is connected to the double spectrometer chamber through a gate valve. The gate valve can be close in order to preserve high vacuum in the experimental chamber when access to the source chamber is needed - i.e., refill the powder sample. Our source can work both with powder, gas or evaporating liquid samples.

Vapor or gas sample is generally injected from the gas inlet on top through a 6 mm stainless steel tube, which is connected to a regulating valve. The sample is free to expand down in the 6 mm tube (contained in the service chamber) which goes down towards the oven. At the edge of the oven a skimmer over 1 mm diameter sprays out the molecular jet towards a 2 mm skimmer which collimates the molecular beam going towards the experimental chamber.

Alternatively, powder sample can be loaded inside the oven, which can be heated with the use of resistors. Using a buffer inert gas, such as helium the evaporated powder can be then pushed towards the nozzle and sent to the experiment. Lastly, the oven can also be easily replaced with a needle with size of usually around 400 µm to act as a nozzle depending on the experiment.

A XY Manipulator can be used to adjust the alignment in between the oven/needle and the skimmer, while a Z manipulator is used to change the distance in between the nozzle and the skimmer to adjust

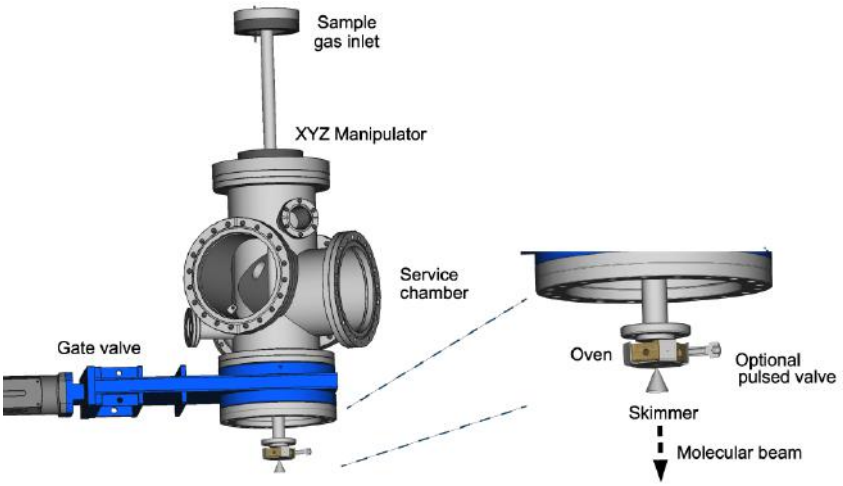

Figure 3.12: A scheme of the main components of the molecular source. Vapor or gas sample is delivered through a 6 mm tube inside the service chamber, which is connected to an additional oven (for powder sample, not used) and sprayed out of the oven towards a 2 mm skimmer, which collimated the molecular jet towards the experimental chamber. An XYZ Manipulator can be used to optimize the alignment in between the oven and the skimmer, while a gate valve is used to isolate the service chamber without venting the experimental chamber.

the collimation of the molecular beam and the amount of sampled delivered to the experimental chamber.

3.3 SCALING UV GENERATION

3.3.0.1 *Previous work*

In Sec. 3.1.3 we discussed several schemes for the production of UV pulses. Crystal-based scheme, such as achromatic phase-matching [47, 48] has demonstrated sub-10 fs duration, but they require careful chirp-management to compensate for second order dispersion. On the other hand, different schemes employing non-linear processes in gas has also been demonstrated: methods based on four-wave mixing [49] or cross-phase modulation in gas [50]. Among these, THG based methods achieved the best pulse duration [63, 64] due mostly to the larger phase-matching bandwidth and low dispersion provided by noble gases as non-linear media, at the expense of conversion efficiency. Employing THG, our group demonstrated the possibility of generating sub-2 fs UV pulses, with a precise optimization of the generation cell, from which typical spectra are reported in Fig. 3.13 [31].

Briefly, 5 fs NIR pulses has been focused in a gas cell filled with argon, using a focusing mirror of focal $f = 80$ cm. The micro-machined glass cell, which is currently employed in the setup and is described in

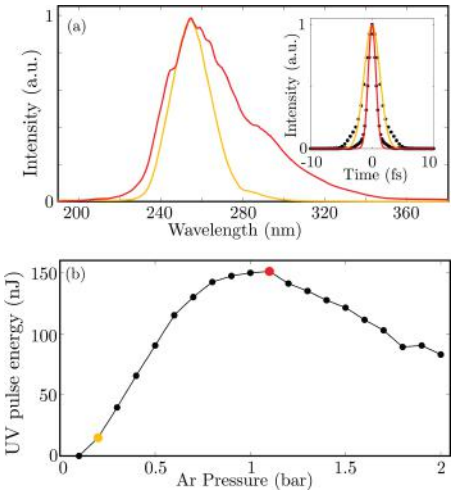

Figure 3.13: (a) THG obtained by focusing 250 µJ energy per pulse, 5 fs few-cycle NIR pulses centered at 700 nm in a laser-machined gas cell filled with 0.2 bar (yellow line) and 1.1 bar (red line), with a transform limit duration of 3 fs and 1.45 fs, respectively. The inset shows the corresponding Fourier transforms and the Gaussian fitting functions. (b) UV pulse energy measured as a function of the gas pressure. The red and yellow dot corresponds to the gas pressure values used for the two spectra in (a). Adapted from [31].

a previous section (3.1.3.1), represents a key aspect of the generation, since it allows a very precise control on the gas distribution. The possibility of carefully limit the gas density to a small volume was fundamental to control several non-linear processes at play, such as ionization, which is strongly competing with the THG. In other words, the creating of ionized gas in the interaction region reduces the number of emitters available for the up-conversion, affecting the overall efficiency. However, this process can also be exploited to increase the output bandwidth and reducing the pulse duration of a pure THG process, as it has been studied experimentally and theoretically in [64]. In this work, Reiter *et al.* have demonstrated that ionization is able to further increase the UV spectrum by means of an ultrafast reshaping of the spatio-temporal profile of the driving field. In particular, the up-conversion is temporally confined to the leading edge of the fundamental pulse, resulting in a temporal gate for the generation.

This effect can be observed in Fig. 3.13(a), where the yellow and red spectra are obtained for 0.2 bar and 1.1 bar, respectively. For low argon pressure, the corresponding transform limit of the spectrum is 3 fs, which is the expected duration of a purely up-converted 5 fs pulse. When the pressure is increased up to 1.1 bar, the resulting spectrum has almost twice the bandwidth of the previous one, with a transform limit duration of only 1.45 fs. Most notably, this value of pressure represents also the optimum for the conversion efficiency (Fig. 3.13 (b)), after which the UV yield starts to decrease, suggesting

that ionization is becoming detrimental for upconversion efficiency. This optimal value therefore represents the best trade-off ionization level in order to favor UV duration, while not affecting the efficiency.

3.3.0.2 *Spectral separators*

For an input energy of 250 µJ, the maximum conversion efficiency obtained in this scheme is 0.06 %. Due to collinear generation geometry, the residual NIR beam has to be removed, however, the spectral separation is not trivial when dealing with few-fs UV pulse duration. In [31], the separation is performed by custom-made dichroic optics (Layertec). Dielectric coatings allow particular tunability and they have been designed in order to maximize UV reflectivity and NIR transmission and minimize the GVD introduced to the UV pulse. In this specific case, the UV reflectivity is above 95 %, while achieving $< 5\%$ reflectivity of for NIR pulses. Three reflections are needed in order to reduced NIR pulses of 4 orders of magnitude to an energy of 28 nJ.
In spite of high reflectivity for UV, the reproducibility of the coatings remains the main drawback of employing dielectric mirrors. In particular at short wavelength manufacturers need to operate at the very limit of their technological capabilities, resulting in several batch with very different performances. This is due to the strong UV absorption of most materials commonly used for producing the coating in dielectric optics. In particular, we found that the GDD introduced by the dichroics is far larger than the one specified by the producers: the error bar for the GDD provided by the company (around 10 fs^2) is too large for few-fs UV, despite being low enough for many other applications. Even 5 fs^2 would stretch a 2 fs to more than 3 times its duration. After different coating runs, we decided to implement a more reliable solution based on Brewster angle reflection on bulk materials. This method has been widely used for VUV pulses [65] and it relies on the intrinsic properties of many materials. When used at Brewster angle for the fundamental ($\theta_B = 74.8^\circ$ at 800 nm), the reflectivity for NIR light theoretically goes down to zero. In reality, the extinction ratio can easily reach 1 : 1000, which is comparable to the dichroic mirrors. In addition, the GDD introduced by reflections on metals or semi-conductors is $< 2\,fs^2$ for the visible and ultraviolet spectral range, compared to dielectrics. Seminal work on UV generation [63, 64] employed this scheme with Silicon bulk polished mirrors and achieved a suppression of 3 to 4 order of magnitude by using one or two reflectors. The disadvantage of this is method is that Silicon shows a much lower reflectivity for the UV, because the Brewster angle for the NIR and the UV spectral range is very close.

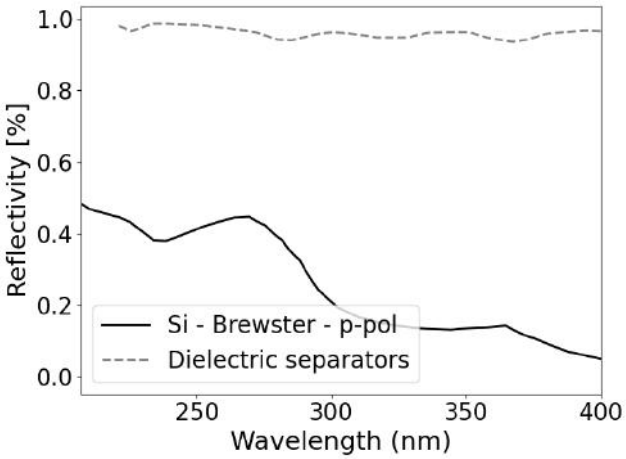

Figure 3.14: Comparison between reflectivity of different spectral separators: solid line indicates bulk polished Silicon substrate, calculated for a p-pol incoming beam at an angle of incidence of 74.8°, which corresponds to the Brewster angle for 800 nm; dashed line is the calculated reflectivity for the Layertec dielectric spectral separators.

In Fig. 3.14 we have calculated the reflectivity of a Silicon surface for a p-polarized incoming beam, with an angle of incidence equal to the Brewster angle for the NIR pulse, which shows a maximum reflectivity of the order of 40 %. In our setup we obtained a suppression of 6.5×10^{-4} of the fundamental down to the 20 nJ level by using two Silicon polished substrate (G & h). Residual NIR energy is attributed to a residual orthogonal polarization component, which is reflected by the mirror. The addition of one more mirror does not increase the suppression factor, because the orthogonal polarization is insensitive to the Brewster angle. To further reduce this number, more sophisticated polarizer scheme could be introduced, to reduce the orthogonal component even further. In order to not affect the UV flux, we employed only 2 mirrors considering that 20 nJ level of residual IR is reduced even further due to the slightly less reflectivity for NIR in respect to UV of the aluminum mirror employed after generation, which result in additional separation. In conclusion, the use of Silicon mirrors assures a very low GDD, at the expense of having available around 20 % the amount of UV flux in respect to dielectric mirrors. Coupled to the very low yield of the UV generation in THG, the low reflectivity of the Brewster Angle separators leads to a very strong reduction of the UV flux available for experiments. For this reason, a modification which increases the UV efficiency is needed.

Table 3.1: List of nonlinear medium and their relevant properties for the generation of UV pulses via direct THG. GVD values are taken from [66]. Third-order susceptibilities for He, Ne, Ar, Kr, Xe and beta barium borate (BBO) are given for a 1055 nm driving laser [67, 68]. $\chi^{(3)}$ for fused silica is given at 1065 nm [69]. Table adapted from [70].

Nonlinear medium	Ionization potential (eV)	GVD at 266 nm (fs^2/mm)	$\chi^{(3)}$ (m^2/V^2)
He	24.59	0.0036	3.43×10^{-28}
Ne	21.56	0.0091	6.17×10^{-28}
Ar	15.76	0.082	8.06×10^{-27}
Kr	14.00	0.192	2.20×10^{-26}
Xe	12.13	0.59	6.46×10^{-26}
Fused silica	–	197.53	2.0×10^{-22}
BBO	–	524.76	4.4×10^{-23}

3.3.1 *Scaling the UV generation*

In our scheme, the gas pressure represents the perfect control parameter for the generation, allowing the increase of the number of emitters and therefore the final yield for UV photons. As discuss in the previous section, the maximum density is limited by ionization in this regard, because it leads to sudden drop of the UV yield after an optimum conversion efficiency is reached (Fig. 3.13. A medium with different ionization potential could indeed allow us to increase the UV flux and overcome the low reflectivity of the separators employed. Seminal work for few-fs UV generation investigated the use of different gas medium [63]. In the following table the relevant properties of non-linear gas medium used for THG generation are reported, while bulk medium is added as reference. We notice that the GVD introduced by the noble gas is almost 3 orders of magnitude lower than bulk medium, which confirm their choice as a non-linear media. In terms of ionization, lighter gases are favored because of the higher ionization potential, as they allow higher pressure and therefore higher UV yield.

For instance, in Fig. 3.15 we reported the UV energy per pulse obtained as a function of gas pressure for the neon and argon. In both tests, 250 µJ of 5 fs driving NIR pulses are focused with a 50 cm focal mirror. The UV and the fundamental are separated by the dielectric optics and after which the energy is measured. The choice of a tighter focus geometry in respect to the previous setup is fundamental in order to account for the different $\chi^{(3)}$ of neon, which is almost 1/12 times the $\chi^{(3)}$ of argon, requiring higher intensity for the THG. In

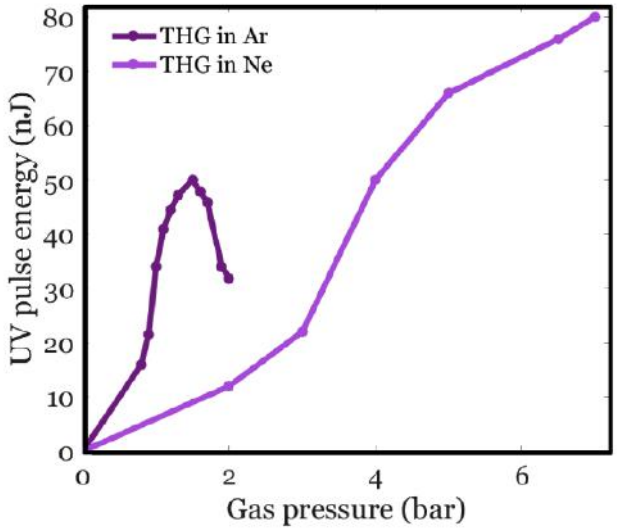

Figure 3.15: Pressure dependence of the UV pulse energy obtained through THG by a 5 fs NIR pulses in argon and neon focused by 50 cm focal mirror. While for argon it is possible to observe a saturation pressure, it is not the case in neon.

argon, the UV pulse energy reaches a maximum of 50 nJ for a pressure of 1.25 bar. After reaching the optimum, it suddenly decreases.

The lower optimum value in respect to the previous geometry can be attributed to ionization, which is favored in the case of a tighter focus. Neon, instead, despite showing lower yield below in the argon optimum, allows increasing the pressure much further with an increase of the UV efficiency, resulting in almost two times the UV flux obtained in argon. The different behavior of the two gases is clearly explained in by the different ionization energy: in neon the optimal pressure value for which ionization starts to reduce significantly the UV yield is much higher than argon and it allows an efficient generation up to 6 bar where we reach almost double the maximum efficiency of argon. At the same time, since the susceptibility $\chi^{(3)}$ of neon is almost 1/12 then argon, for similar pressure the yield in neon is much lower than argon. We note that, the saturation pressure for neon is not observed because it is higher than the investigate pressure range, which was limited by the correct functioning of the turbopumps employed during the tests.

Additionally, to further increase the UV yield, the input power of the driver has also been increased. Having higher intensities for the non-linear processes is an alternative way of observing the saturation of the process, and therefore the maximum UV yield.

450 µJ can be sent to the UV generation by using a 50/50 BS in the first chamber of the beamline. Paired with the 50 cm focal mirror, it corresponds to an increase in intensity of almost one order of magnitude, up to $2.0 \times 10^{15}\,\mathrm{W\,cm^{-2}}$. In addition, the pumping speed of

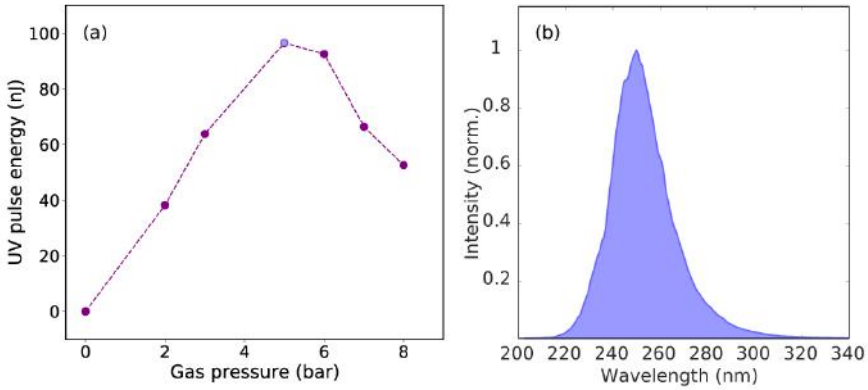

Figure 3.16: (a) UV energy per pulse as function of the neon gas pressure, obtained with 450 µJ input energy per pulse, 5 fs NIR pulses, focused with a 50 cm focal mirror. Power has been measured after reflection on 2 Si mirror at Brewster's angle for spectral separations. (b) Spectrum obtained for the maximum value of pressure 5 bar.

the differential pumping has been increased, for having the possibility of exploring the full range of pressure, with the system being able to reach 10 bar.

In Fig. 3.16(a) the UV yield in the current setup as a function of the neon pressure is reported. In this case, the UV yield is measured downstream the generation, when the separation is performed with a pair of Si-mirrors. The UV efficiency follows a similar behavior as the one reported previously for argon (Fig. 3.13. It increases up to a maximum value, while it decreases immediately for higher gas pressure. For neon, the maximum gas pressure corresponds to a 5 bar. In respect Fig. 3.15 where the maximum was not observed, the optimum value has been shifted towards lower pressure value, due to the increased generation intensity.

We note that the maximum yield is 100 nJ and it is lower than what we achieved previously in argon [31]. This discrepancy can be attributed to the different separator employed. In the case of argon and dielectric mirrors, considering a reflectivity of 0.95 for each separator, the estimated UV energy at the generation is 215 nJ. In the upgraded setup, which includes the pair of silicon separators, lower reflectivity of 0.40 is estimated (Fig. 3.14), which results in a much larger energy at the generation of 700 nJ for the optimum of neon. We can therefore conclude that employing neon has increased the generation efficiency of almost four times in respect to argon.

From this perspective, employing the spectral separators in combination with a tighter focus and higher pressure of neon, resulted in producing a similar UV flux in respect the previous setup, with the advantage of not relying on dielectric optics. This assure that no unknown GDD is introduced in the optical path.

3.3.2 *Temporal characterization*

Established pulse characterization techniques such as FROG [71] or SPIDER [72] are typically based on non-linear conversion of the unknown pulses with a replica or a gate pulse. When applying these techniques to extremely short UV pulses, the lack of suitable medium for UV generation affects also the possible methods to characterize few-fs UV pulses. Due to the short duration, as mentioned earlier, a direct measurement to minimize dispersion introduced on the pulses. Additionally, since the generation of few-fs UV is also strongly inefficient, producing UV in the 0.2 µJ to 1 µJ range, characterization methods which require high photon flux are also not recommended.

The lack of suitable non-linear medium limits especially those methods which allows full reconstruction of amplitude and phase of the pulses. In particular, these methods require broad phase-matching condition for SFG or SHG in the non-linear conversion step, which in the case of ultrashort UV pulses can be achieved only with unrealistically thin non-linear crystals, below 5 µm. For instance, Borrego-Varillas *et al.* characterized 8.4 fs pulses through two-dimensional spectral shearing interferometry (2DSI) [73], employing difference frequency generation (DFG) because it provides broader phase-matching bandwidth compared to the typical SFG [48]. For < 5 fs UV pulses, Self-diffraction FROG (SD-FROG) have been adapted in vacuum [63], to drastically reduced the second order dispersion. To this aim, a very thin < 15 µm fused silica plate need to be employed to assure that the pulses are not chirped significantly during the propagation in the non-linear medium. An in vacuum cross-correlation FROG has been used [74] which was specifically designed to overcome the many limitations of measuring a few-fs UV pulse, which in this case were produced by resonant dispersive wave in HCF are combined with a narrow gate pulse in a BBO crystal for DFG. The phase matching condition are provided by a very thin 5 µm thick of the crystal, whose angle is adjusted in different acquisitions in order to cover the complete UV spectrum. Furthermore, this method relies on advanced retrieval algorithms such as ptychographic techniques [75], which do not depend on independent characterization of the gate pulse.

Ionization-based cross-correlation methods represent an alternative approach. In such methods, multiphoton absorption in gases replaces the non-linear interaction in between the pulses, providing less limitations in terms phase-matching bandwidth. Basically, the two pulses interact and ionize the target, producing a two-colors ion yield signal, which is proportional to the cross-correlation function of the pump

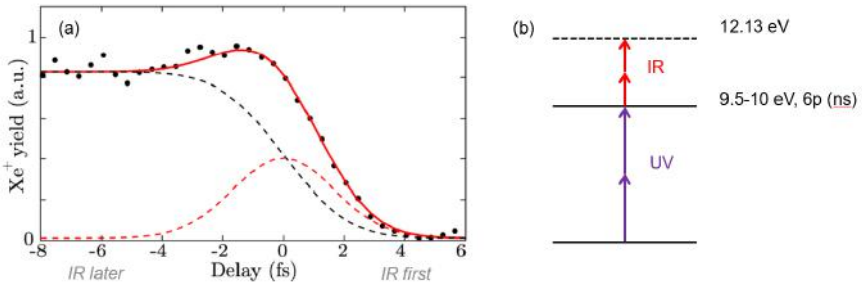

Figure 3.17: (a) Photoionization yield of xenon as a function of the UV and NIR delay (black dots). The trace has been fitted with a direct 2UV+2IR contribution (red dash line) and REMPI through a long lived Rydberg state (black dashed). The final fit is the red solid line. (b) Simple schemes of the energy level involved in the 2UV+2IR photoionization of xenon. Adapted from [31].

and the probe, typically shaped as a Gaussian function. In the most general case, from the cross-correlation width

$$\sigma_{CC} = \sqrt{\frac{\sigma_{UV}^2}{n_{UV}} + \frac{\sigma_{ref}^2}{n_{ref}}} \tag{3.7}$$

the UV duration σ_{UV} is estimated from the duration of a reference pulse, whose width is σ_{ref}. The number of photons involved in the photoionization are expressed by n_{UV} and n_{ref} for the UV and the reference, respectively.

Due the vacuum requirements of particle detection, such methods have the advantage that they can be realized virtually dispersion free, if the GDD introduced by the target itself is negligible. However, they do not carry information regarding the phase, making a full reconstruction of the pulses not possible. Additionally, since they are based on photoionization, they possess a strong dependence on the energy structure of the target, which should be taken into account, and it should allow an ionization channel given by the absorption of the two pulses. In this context, single atoms, such as noble gases, should be favored, because more complex energy structures could influence the ion yield through intermediate states. In any case, a detailed characterization of all the possible ionization channel is required. For instance, UV-UV autocorrelation in krypton has been used to characterize a 2.8 fs pulse generated through THG in neon [64].

Previously, in [31] we employed xenon atoms as a target and the resulting Xe^+ yield as a function of the UV - NIR delay is shown in Fig.3.17 (a).

The cross-correlation shows a step-like behavior, in which the ionization stabilizes to a maximum level and remain constants after the time overlap, when the NIR pulse arrives much later than the UV. The signal can be interpreted, by considering the presence of a long-lived

6p Rydberg state in the electronic structure of xenon. This state is populated by the absorption of 2UV photons [76, 77] (Fig. 3.17 (b)) and the target is then ionized by the absorption of additional 2 NIR photons (REMPI). Additionally, a second Gaussian contribution represents the direct absorption of the two colors. Both direct and REMPI contribution needs to be included (dashed lines, red for direct and black for REMPI) to obtain a good estimation of the width. From the width σ_{cc} it is then possible to apply Eq. (3.7) to extract the UV duration. The NIR pulse duration was independently measured to a FWHM of 5.2 fs through a SH-FROG before the beamline. Therefore, we can extract an UV FWHM duration of 1.95 fs, which in 2019 was the shortest UV pulse ever generated.

In this thesis, we combined the UV pulse with the NIR pulse coming from the first arm (Fig.3.3) to ionize krypton gas, as an alternative to xenon.

3.3.2.1 *Krypton*

Measuring the ion yield is an integrated measurement and therefore it lacks information in respect to the different ionization channels involved, which are all contributing to the final signal. Photoelectron spectroscopy, however, is able to separate the different contributions by accessing the kinetic energy of the emitted electrons. In respect to xenon, krypton stands as a good alternative because it shows a similar ionization energy as xenon, but a much simpler electronic structure.

The two pulses, UV and NIR, are combined in the interaction chamber, following the same tight-angle non-collinear geometry as in [31]. The very small angle of less than 1 degree in between the UV and NIR pulse has a very small effect ($< 2\%$ longer) on the cross-correlation signal.
The krypton gas is diffused through a needle in the experimental chamber and the resulting photoelectrons are collected on the VMI side of the double spectrometer described in 3.2.1. For the characterization, the UV energy is kept at 80 nJ for the whole experiment, which gives an estimated intensity of $I = 2 \times 10^{12}\,\mathrm{W\,cm^{-2}}$ on target. The NIR pulses intensity can be adjusted by using a motorized aperture, but it has been kept at $9 \times 10^{12}\,\mathrm{W\,cm^{-2}}$ due to the high order of photons required. Fig. 3.18 shows the angular photoelectron kinetic energy distribution obtained in krypton, when the UV and the NIR pulse are at time overlap. For the rest of the discussion, all the images have been acquired over 30 000 shots, they are symmetrized along both y and x axis and Abel inverted with the Rbasex method implemented in PyAbel [57]. The VMI image shows many broad peaks parallel to the laser polarization, in particular for energies lower than 1 eV. We observe three main peaks for energies 0.14 eV, 0.37 eV and 0.71 eV. The small energy separations in between the peaks are not compatible with our photon energies and therefore might indicates the presence

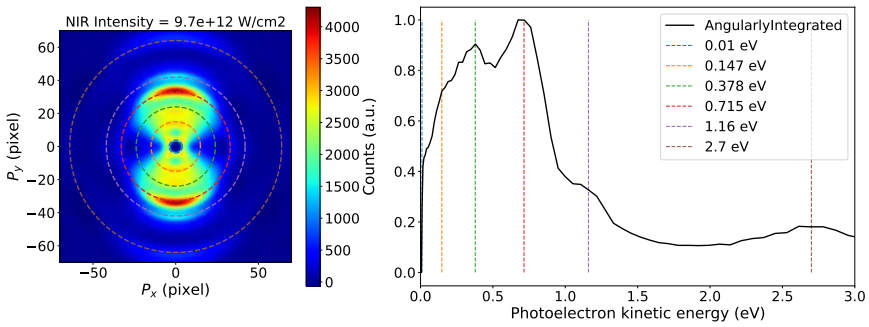

Figure 3.18: *Left*: photoelectron angular and energy distribution of krypton obtained with both UV and NIR pulses at time Overlap. UV intensity is estimated $I_{UV} = 2 \times 10^{12}\,\mathrm{W\,cm^{-2}}$, while NIR intensity is $9.7 \times 10^{12}\,\mathrm{W\,cm^{-2}}$. Laser polarization is parallel with the y-axis. Circles indicates specific energy peaks (see legend on right). The experimental VMI image is obtained over 30.000 shots, is symmetrized along x and y and then Abel inverted. *Right*: Angularly-integrated photoelectron spectrum.

of intermediate states. For higher energies, weaker peaks at 1.16 eV and 2.7 eV are observed, whose separation of 1.54 eV is compatible with 1 NIR photons. Therefore, they might be assigned to ATI peaks. In general, since the resulting kinetic energy obtained by ionizing with 3UV + 1NIR photons would be much higher, the UV photons number observe by ionization with the two colors should be 2. As a first approximation, it is also possible to exclude single UV absorption, because it would require a large (> 5) number of NIR photons to ionize and therefore it will be less favorable. A schematic representation of photoionization process is shown in Fig. 3.19, where the main energy levels of Kr and Kr^+ are reported, based on [78].

The lowest number of NIR photons required for ionization is 3, if one consider the lower $j = 3/2$ cationic state. By assuming a photon energy of 4.9 eV for the UV photon and 1.65 eV for the NIR photon, we can estimate an excess photoelectron kinetic energy of 0.7 eV. This corresponds to the strongest peak in the spectrum 3.18 (red). Due to the strong spin-orbit splitting of 0.6 eV, ionization from the state $j = 1/2$ will result to a kinetic energy of 0.1 eV, which is also observed in 3.18 (orange). We note that, as far as our interpretation goes, since there are no Rydberg states involved the expected shape for the cross-correlation should be similar to Gaussian function.

In order to confirm the number of photons involved, we acquired different VMI images as a function of the NIR intensity, while keeping the UV constant. The results can be observed in Fig. 3.20 (left).

Overall, we do not observe the appearance of new peaks for this specific intensity range. For low kinetic energies, the peak at 0.15 eV becomes dominant in the spectrum for the highest intensity of $1.2 \times 10^{13}\,\mathrm{W\,cm^{-2}}$, while for lower intensities the maximum is observed for

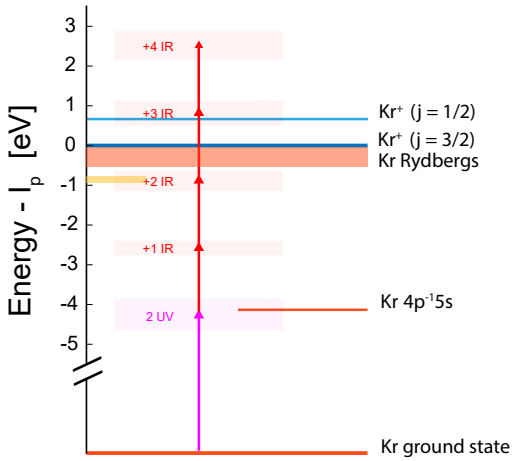

Figure 3.19: Schematic representation of electronic energy levels in krypton. The energy axis is relative to the ionization potential $I_p = 13.99\,\text{eV}$ of the $j = 3/2$ ionization limit energy. The $j = 1/2$ is separated 0.6 eV higher, the Rydberg states are indicated with a large red area. The arrows represent the different number of photons involved in the photoionization. The shaded area for each arrow represents the range of photon energies available, renormalizing the spectrum by a factor $\sqrt{n}$, with n is the number of photons. The yellow shaded area indicates probable intermediate states for REMPI.

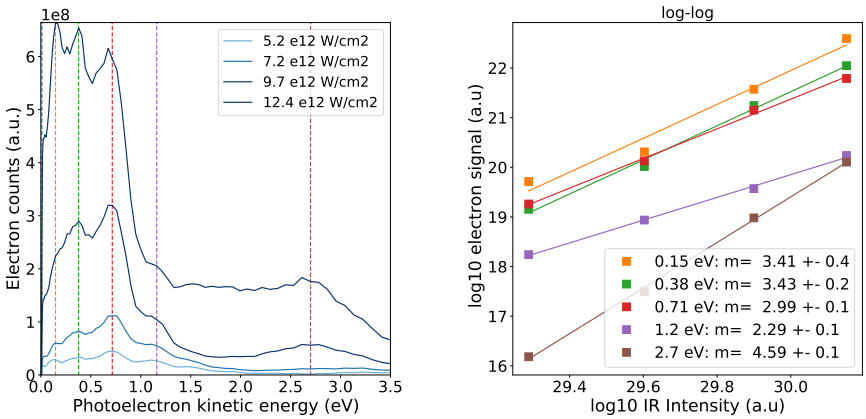

Figure 3.20: *Left:*Angularly integrated photoelectron kinetic energy spectrum obtaining while varying the intensity of the NIR probe. UV is kept at $2 \times 10^{12}\,\text{W cm}^{-2}$. Vertical dashed lines indicate assigned peaks, as depicted in 3.18. *Right:* Log-log plot of integrated electron counts around the peaks (width $= \pm 0.1\,\text{eV}$): solid line indicates the best fit $mx + q$ performed to obtain the slope, which is reported in the legend together with the standard deviation of the fit.

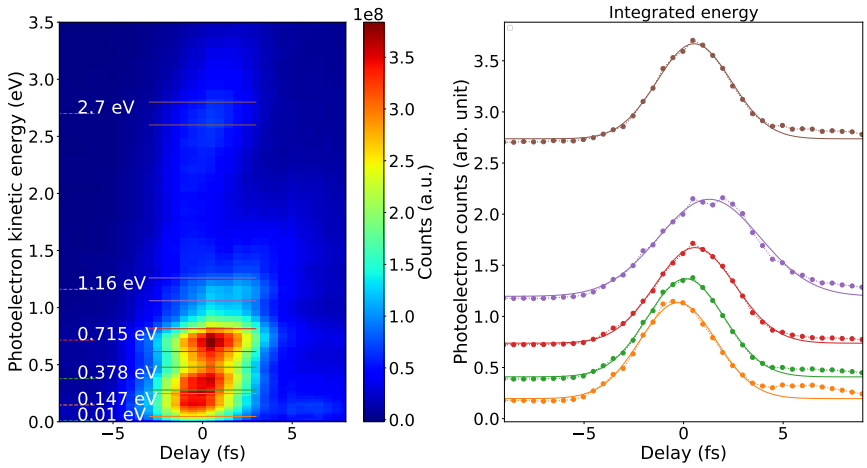

Figure 3.21: *Left:* Angularly integrated photoelectron energy distribution as function of the UV-NIR delay. Positive delay indicates NIR after. Energies corresponding to assigned peak from 3.20 are reported as horizontal dashed line, while solid line indicates energy bin (width ± 0.1 eV) considered for energy integrated signal. *Right:* Energy integrated signal, color code following 3.20.

0.7 eV. For kinetic energies above 1 eV, the amplitude of the peak at 2.7 eV rises very fast with the intensity.

To determine the nonlinear order of this dependence, the spectra are integrated over an energy region of width $= \pm 0.1$ eV around each peak, and then plotted on a bi-logarithmic scale (Fig. 3.20 right). We fitted each peak independently with a line $\log_{10}(y) = m \log_{10}(I_{IR}) + q$. The low kinetic energies peaks below < 1 eV all show slope compatible with third-order dependence, confirming our previous interpretation based only on energy conservation. The lowest peaks 0.1 eV and 0.3 eV follow poorly at lower intensities, which, together with the fact that they become dominant for high intensity, could suggest the presence of coexisting ionization channels for the same kinetic energies. For instance, their separation in energy could indicates that the photoionization is not direct but mediated by resonant states. In Fig. 3.19, the yellow shaded area indicates the presence of possible intermediate states. The 2.7 eV peak possesses a higher slope which is compatible with 4 or 5 photons, confirming our previous interpretation for this energy range. Instead, the intermediate peak at 1.16 eV is very much underestimated through the scaling, since it should obey to a third order exponential.

Having assign specific number of photons on each peak, a sequence of photoelectron spectra has been acquired by varying the UV pump - NIR probe delay, with a step of 0.5 fs. The corresponding photoelectron energy map as a function of the delay is reported In Fig. 3.21, where positive delays indicate NIR pulses after the UV.

Table 3.2: Fit results of the time dependent signal in Fig. 3.21 (right). σ_{cc} represents the width of a Gaussian centered at t_0. Standard deviation for the fit results is 2%. The estimated FWHM for the UV has been calculated from a FWHM 5.6 fs NIR pulse using Eq. (3.7), considering the number of photons extracted from 3.20. The error on UV duration has been propagated and is estimated to be 5%.

Energy (eV)	σ_{cc} (fs)	t_0 (fs)	FWHM UV (fs)
0.14	1.91	-0.28	4.44
0.38	1.92	0.11	4.51
0.715	2.01	0.57	4.92
1.16	2.55	1.13	7.19
2.7	1.86	0.53	4.8

All the peaks show a Gaussian-like time profile. The dynamics is mostly confined in a 10 fs windows, with only a very weak tail for positive delay. In addition, the different energy region shows a clearly visible shift in time: the time peak from the low kinetic energies (0.1 eV and 0.3 eV) is 0.2 fs earlier than the one for 0.7 eV. Higher energies are synchronized to this last peak, although the energy peak at 1.16 eV is harder to measure, since it is longer than the others. Nevertheless, a very weak signal which is shifting towards positive time is also observed in between the two highest peak. The presence of this time dependence in the peaks could be an additional indication that the low kinetic energy channel involves intermediate states, which could alter the cross-correlation. Alternatively, it could be due to intrinsic chirp of the pulse.

Each peak has been integrated in the same energy range with a width ± 0.1 eV. The resulting time dependent signal is reported in the right panel of 3.21. The width σ_{cc}, has been extracted by fitting each time signal with a Gaussian function, in which peak time t_0 has been left as free parameter. The result of the two fitted parameters are reported for each energy range in 3.2.

Although peaked at different time, the low kinetic energy electrons show very similar cross-correlation width. Even though the precise assignment cannot be done on these states, the estimated number of photons can still be applied, by assuming no intermediate dynamics. The 1.16 eV peak is sensibly longer. Instead, the peak at 2.7 eV shows the shortest width, as expected by a higher number of photons. The fit also confirm that the 0.7 and 2.7 eV are well synchronized in time. By measuring the NIR pulses independently with a FROG before the beamline and obtaining $\mathrm{FWHM}_{NIR} = (5.6 \pm 0.2)$ fs and considering the number of photons estimated previously, it is possible to extract the UV duration using (3.7), as reported also in Tab. 3.2. All the UV

duration, expect the channel at 1.16 eV which could not be assigned, can be averaged to obtain a final measurement of (4.6 ± 0.2) fs. The generated UV pulses are definitely in the few-fs range, but the estimated FWHM are longer than the transform limit of the spectrum 3.16 (2.3 fs). Considering the short duration of the UV pulses, we estimate that a total of only 3.2 fs^2 GDD is needed to stretch the pulses. This residual GDD can originate in the generation cell, due to the high pressure or afterwards, due to some residual GDD in the optics. Additionally, the estimated UV duration is very much dependent on the NIR duration. The independent characterization performed with FROG is performed before entering the beamline, and although the optics and the compression along the propagation are optimized to not alter the spectrum and duration of the NIR pulses, the delivered probe pulses can differ from the measured one. In principle, an independent characterization of the reference pulse *in-situ* would be needed.

For such experiment, at the moment, it is not possible to exclude that those specific resonant states are reached during the photoionization step. For instance, we already noted that the low kinetic energies peaks show a very small separation compared to the photon energies. At the current state, one would need to characterize specifically the temporal properties of these states, such lifetimes and dynamics occurring in krypton. For instance, one could apply time-dependent simulation of electron wavepacket in the atom, which should provide a more reliable answer to the internal dynamics after the UV excitation, which could prevent us a correct estimation for the UV duration. In conclusion, the estimated UV duration of (4.6 ± 0.2) fs should be considered as an upper limit duration of the generated pulse, which is however sufficient to exploit the temporal resolution of such pulses for time-resolved experiments in molecules, which will be described in the rest of the thesis.

4

STUDY OF METHYL-IODIDE DISSOCIATION IN THE A-BAND WITH FEW-FS RESOLUTION

In this chapter we will present a time-resolved pump-probe experiment which exploits the few-fs UV pulse described so far. We focused our investigation on molecules which are extensively studied in such spectral range, with the goal of exploring the initial instants after the UV excitation, so far not accessible because of the duration of the pump pulses. The first molecule is methyl-iodide, or iodomethane.

Methyl-iodide (CH_3I) is a well-known target, typically employed for testing theoretical and experimental techniques. It shows an excited state dynamics which is initiated by the absorption of a single UV photon at 260 nm. It is a widely employed target because of its balance amount of complexity, while still being a relatively easy to model molecule under the appropriate approximations, as we will discuss here. This molecule also shows the strongest cross-section in the spectral range of the few-fs UV spectrum. Additionally, recent investigation of its most known dynamics in the A-band have also estimated to show a very fast dynamics, on the order of tens of fs [79].

The experiment was performed in spring 2021. I performed the literature research, designed the experiment with the aid of my supervisors and run the experimental campaign. I analyzed the data. The theoretical calculation has been realized by Dr. Jesús González-Vázquez from Universidad Autónoma de Madrid. The interpretation of the results has been carried out by me and Dr. González-Vázquez.

4.1 INTRODUCTION AND PREVIOUS WORK

Methyl-iodide, or iodomethane, is the simplest of halide alkane or halogenated molecules. As such, it presents the same structure of methane, with a hydrogen replaced by a heavier iodine atom (Fig 4.1 *inset*). Although its intrinsic interest in atmospheric chemistry, CH_3I has served for many years as a prototype for investigating photodissociation dynamics of polyatomic molecules, due to its simplified structure.

In particular, its relatively low number of atoms and its seemingly simple dissociation dynamics involving an avoided crossing, makes CH_3I an ideal target in order to understand dynamics occurring in more complex molecules. Its particular structure also simplifies the theoretical treatment for the molecule. Due to the heavier mass of iodine compared to the three hydrogens, typically CH_3I is modelled as a triatomic linear molecule, with the hydrogen atoms replaced

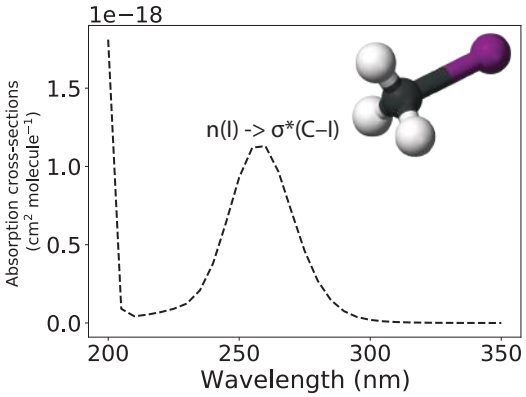

Figure 4.1: Absorption cross-section of methyl-iodide in the ultraviolet, adapted from [80]. The A-band is a broad featureless continuum ranging from 230 nm to 300 nm. *Inset:* ball and stick model of methyl-iodide with iodine (purple), carbon (black), hydrogen (white).

with an effective third atoms in their center of mass, reducing the complexity of the problem. Even since the sixties, methyl-iodide has been extensively studied, both experimentally and theoretically on many of its properties, such as internal energy distribution after dissociations, crossings in between different potential energy surfaces or investigation of the different electronic transitions.

Several studies have been conducted on the UV photodissociation of CH_3I via the first absorption band, also known as the A-band, whose absorption spectrum is reported in Fig. 4.1. The subsequent evolution gained huge interest as an example of very quick dynamics which leads to the C-I bond cleavage. Additionally, the dynamics is occurring in the presence of a conical intersection.

The A-band appears as a broad absorption continuum with a maximum around 260 nm, extending between 220 nm to 300 nm. Gedanken and coworkers have assigned it to a $n(I) \rightarrow \sigma^* (C-I)$ transition where a non-bonding p electron of iodine is promoted to the lowest available antibonding molecular orbital [81]. Due to the strong spin-orbit coupling, due to iodine, this transition comprises of a total of 5 states, which in Mulliken notation are addressed as $^3Q_2$, $^3Q_1$, $^3Q_{0+}$, $^3Q_{0-}$ and $^1Q_1$ [82]. Among these, only $^3Q_1$, $^3Q_{0+}$ and $^1Q_1$ are dipole allowed, with $^3Q_{0+}$ contributing up to 98% of the band [81]. In particular, $^3Q_0$ is the only parallel transition. In the dissociation limit, the $^3Q_{0+}$ (from now on $^3Q_0$) correlates with the formation of a methyl and iodine $CH_3 + I^*(^2P_{1/2})$, where iodine is in the first excited state. The higher energy state $^1Q_1$ (in general, all the other states) also lead to dissociation, but they correlate instead with iodine in the ground state $CH_3 + I(^2P_{3/2})$. Between $^3Q_0$ and $^1Q_1$ there is a conical intersection, which allows the formation of a substantial number of products from

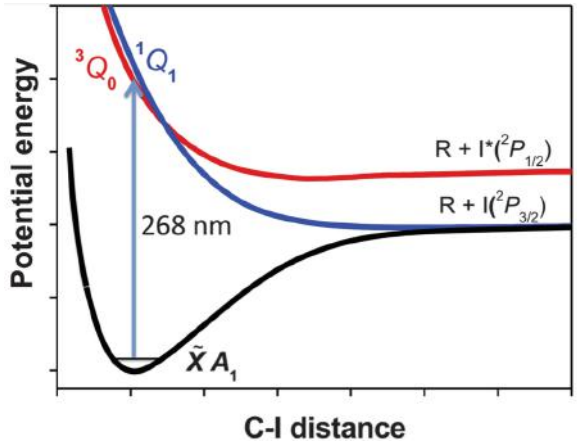

Figure 4.2: Scheme of selected potential energy curves along the C-I bond. The most favorable transition 98% after the absorption of a 266 nm photon is towards the $^3Q_0$ (red line) which correlates in the dissociation limit with $CH_3 + I^*(^2P_{1/2})$. There is however a substantial high amount of iodine ground state produced in the other channel $CH_3 + I(^2P_{3/2})$ (blue line). The increase of ground state iodine is explained by the conical intersection in between the two curves, which allows part of the population of $^3Q_0$ to produce unexcited iodine. Adapted from [83].

the $^3Q_0$ to the $CH_3 + I(^2P_{1/2})$, via non-adiabatic transition. A simplified scheme of the process is represented in Fig. 4.2. More specifically, after the absorption of one UV photon at 266 nm a transition from the ground state to mostly the $^3Q_0$ is expected. The evolution of the molecule on this potential energy surface will result in C-I cleavage, with methyl CH_3 and iodine excited I^* in the first spin-orbit level as products. The presence of the conical intersection with the $^1Q_1$ state decrease the yield of excited iodine, since this state correlates with iodine ground state. Measurement of the branching ratio 0.79 between excited iodine and the iodine [84], state that the dissociation mainly occurs on the $^3Q_0$ curve with the production of iodine in its excited state, while only a small amount passes through its ground state through $^1Q_1$. Furthermore, this interpretation is also verified by looking at anisotropy parameter for each transition: the dissociation via the $^3Q_0$, which again correlates with $I^*(^2P_{1/2})$ iodine, possess $\beta \approx 2$. A similar value is also measured for the ground state iodine $I(^2P_{3/2})$, therefore, since the transition to $^1Q_1$ is perpendicular, $I(^2P_{3/2})$ fragments must come predominantly from the absorption to $^3Q_0$, followed a transition to $^1Q_1$ through the conical intersection. Still, a small contribution from direct dissociation on the $^1Q_1$, observed in the small perpendicular character.

Several time-resolved investigations of the photodissociation in the A-band has been performed through many experimental schemes. Ion-VMI techniques give access to the kinetic energy of the photoproducts, which allows to distinguish the two dissociation pathways by looking

at iodine and at the same time measure the branching ratio of the reaction [84]. The reaction times and vibrational dependence have been investigated through (2+1) REMPI [85] or non-resonant probes [86], with spectral selection inside the A-band [87]. The observed sub-100 fs dynamics have been assigned through wavepackets evolution on the available *ab-initio* PES, obtained with increasing numbers of degrees of freedom. In the following, we will describe other studies which, by using shorter pulses, have attempted to track in real time the fast dissociation dynamics after excitation in the A-Band.

Attar *et al.* measured the transition-state dynamics at 266 nm using femtosecond XUV transient absorption (TA) spectroscopy by real-time evolution of core-to-valence transition near the iodine N-edge in the 45-60 eV range [88]. New core-to-valence electronic states appears during the C-I cleavage, which decays simultaneously with the atomic iodine resonances assigned to $I(^2P_{3/2})$ and $I^*(^2P_{1/2})$. These resonances are reach in 40 fs and decays in 90 fs. More recently, Chang *et al.* improved the time resolution to map the wavepacket evolution passing through the conical intersection by measuring the so-called bifurcation time of (14 ± 4) fs, or the time in which the wavepacket splits in between the $^3Q_0$ and $^1Q_1$ [79].

Photoelectron spectroscopy has been employed by Warne *et al.* using as probe multiphoton ionization at 400 nm [89] and more recently XUV femtosecond pulses [90]. In the first work, they investigated different dynamics by exciting different region of the A-band, observing different dynamics. In the second work, in which they limit the investigation to a 269 nm pump, they show features in the photoelectron spectrum that undergo large shifts in binding energy with time, through which they map the extending C–I bond as the molecule dissociates. A cross-correlation of 60 fs limits any insight on shorter time range.

Lastly, Baumann *et al.* performed ion time-of-flight measurement using a single-shot UV pump - VUV probe scheme, investigating simultaneously valence and Rydberg excitation [91]. The very short cross-correlation of 30 fs allow them to follow the wavepacket dynamics in the FC region in the time-resolved signal of the parent, methyl and iodine ions. In particular, time constant of 98 ± 2 and (28 ± 2) fs were assign to $^3Q_0$ and $^1Q_1$ respectively, mediated by the VUV ionization window.

Despite the methods employed, real time tracking of the very quick dynamics underlying the photodissociation of CH_3I has been still difficult to reach. Powerful transient absorption schemes such in [79] are still operating at the limit of their capabilities if the pump pulse is not shorter than the time the wavepacket takes to evolve on the PES. In particular, their estimation is limited mostly by the duration of the UV pump (20 fs), which might still affect the undergoing dynamics while the CI is reached. Our work, which uses a pump pulse with

sufficient duration of 2-4 fs represents the first attempt at investigating the initial steps of such dynamics.

4.2 EXPERIMENT AND RESULTS

Our investigation is performed using the UV described in the previous section 3.1.3 in combination with the NIR pulses as a probe. 3.1.1. The UV spectrum used is reported in 3.16(b). In terms of photon energy, it is centered at 4.9 eV and extends from 4.4 eV to 5.6 eV, full range. It is therefore 16 nm shifted towards higher energies in respect the A-band reported in 4.1. Although the peak wavelength is not matching precisely, the bandwidth supported by our pulse is covering almost the full absorption band [84]. UV duration has been estimated to be 4.6 fs in the previous chapter 3.1.3. The energy of the pump was varied by controlling the generation gas pressure, but it has been kept fixed at 90 nJ, which corresponds with an estimated intensity on target of $3.8 \times 10^{12}\,\mathrm{W\,cm^{-2}}$.

A typical probe spectrum is reported in 3.2. Its carrier wavelength corresponds to 1.65 eV, with a bandwidth of around 0.6 eV. It is delivered on target by means of the golden toroidal mirror and its intensity can be controlled in a range of $9.2 \times 10^{11}\,\mathrm{W\,cm^{-2}}$ to $1.2 \times 10^{13}\,\mathrm{W\,cm^{-2}}$, through a motorized iris installed before focusing. The lowest value was chosen for the time-resolved scan, because it gives negligible signal level for the probe-only (less than 0.05 % than the two colors). Low intensities are also needed to avoid strong field effect in the analyzed target, while having enough to observe high-order multiphoton ionization. The probe duration is independently compressed by using fused silica glass wedges and looking at the NIR only signal of the target in the spectrometer. Pulse duration is estimated to be 5.5 fs with SH-FROG measurements obtained before the beamline.

CH_3I vapor is delivered to the interaction chamber through the molecular source. A 3 mL stainless steel container has been filled with liquid methyl-iodide (Sigma-Aldrich). The sample delivery system has been kept at room temperature due to the high enough vapor pressure of the target. Indeed, a flow valve is used to limit the flow towards the experiment and keeping the pressure in the interaction chamber to a value 2.2×10^{-6} mbar (background pressure with no sample is 3.1×10^{-7} mbar . The double spectrometer was set to detect ions mass spectrum and photoelectron VMI images for covariance analysis, which we will not discuss in this thesis. Both sides of the spectrometer are calibrated using simulation in SIMION.

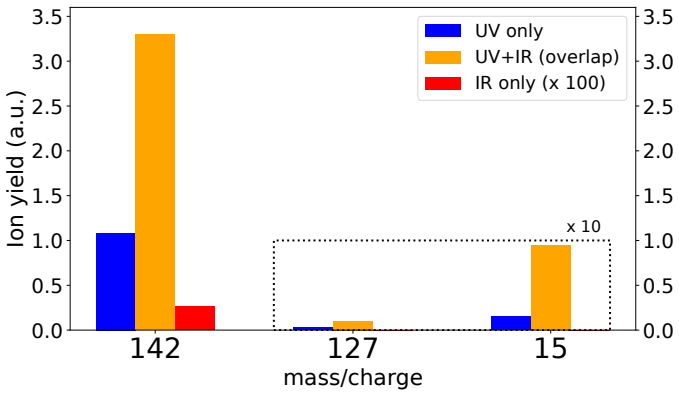

Figure 4.3: Ion yield for the parent (mass = 142 u), iodine cation (127 u) and methyl (15 u) when ionized by only the pump (UV only) , probe (IR only) and both overlapped in time.

4.2.1 *Static mass spectra*

Typical mass spectra obtained for different pump and probe combinations are shown in Fig. 4.3, comprising of pump only, probe only and the two pulses at time overlap. Every point has been obtained by integrated 60 000 laser shots. Only three fragments are detected: the parent ion CH_3I^+ of mass/charge 142 and the two fragments iodine I^+ (mass 127) and methyl CH_3^+ (mass 15).

The probe pulse gives a negligible yield of the parent, more than 3 order of magnitude in respect the pump-probe signal, indicating that the ionization probability from the probe is much lower. The pump only signal shows the presence of the parent, but also the two fragments. Signal from the pump only is also observed, and it can be assigned to multiphoton ionization by the absorption of 2 UV photons, as it is expected if we compare the condition with work with similar pump intensities, for instance [79, 91]. Lower UV intensities have also been investigated without observing substantial differences in the dynamics. For the UV only signal, observation of the two fragments methyl and iodine can be assigned to multiphoton absorption towards higher dissociative cationic states, which are reached by absorption of 3 UV photons. When both pump and probe interact at time overlap, we observe an increase of 3 times the parent yield in respect the pump only, and an increase of almost 1 order of magnitude for the two fragments. A complex combination of the two colors contributes to these ionization channels, but due the broad nature of our pulses a clear assignment is not trivial, as it requires the support of theory be explained.

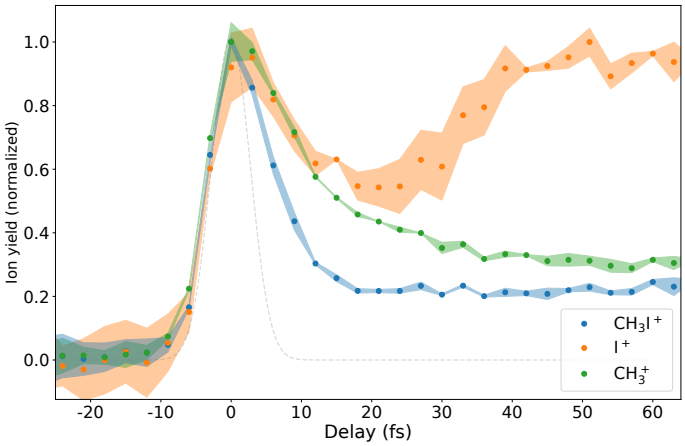

Figure 4.4: Ion yield for the parent CH_3I^+ (blue dots) and the fragments CH_3^+ (green) and I^+ (orange) as a function of the pump - probe delay. The baseline has been subtracted and each signal has been normalized independently to the maximum. Shaded area represents the standard deviation over two measurements. Grey dashed line represents the cross-correlation function with a width estimated for a 1 UV + 3 NIR photons and measured pulse durations.

4.2.2 *Time-resolved ion yield*

A series of mass spectra have been acquired while varying the pump - probe delay with step of 3 fs. Each data point is accumulated over 60 000 shot and each full time range scan has been performed 2 times scanning forwards and backwards in time. Each scan has been normalized over the total yield, in order to minimize slow sample depletion or laser drifts. In Fig. 4.4 we reported the time dependent signal for the three ions. The error bars, represented as shaded area, represent the standard deviation obtained by the two scans. Time zero is shifted to match the parent ion maximum.

All the fragments show a clear maximum for the time overlap. In the figure, we reported as a grey line the expected cross-correlation Gaussian function with a width of 2.3 fs obtained by using Eq. (3.7) and considering the minimum combination of photons for ionization 1 UV + 3 NIR photons. The rise time follows reasonably well the expected cross-correlation for all the ions, which represents a signature of the very fast time resolution we can achieve employing 4-fs UV pulses. In addition, the fact that we are exploiting high order multiphoton process for the probing additionally decreases the cross-correlation width. We note that, to our knowledge, the lowest resolution previously reported was in [79], corresponding to 20 fs.

The parent ion signal is rising to the maximum and decreasing over around 10 fs towards a constant value 0.2 times the peak. In terms of fragments, methyl shows a similar trend, but it takes more

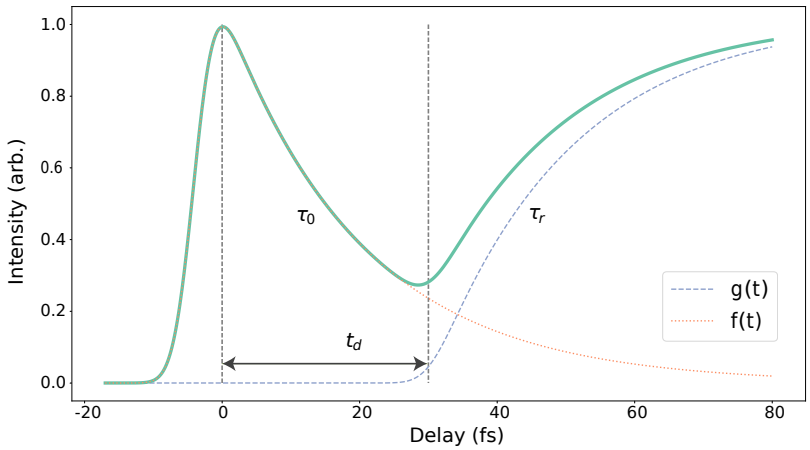

Figure 4.5: Example of the general curves model to describe the experimental results as a sum of two function $f(t)$ and $g(t)$ described in the text. Here we used parameters $\tau_0 = 20\,\text{fs}$, $t_d = 30\,\text{fs}$ and $\tau_r = 20\,\text{fs}$.

time to reach its constant value. Methyl and iodine decrease after the overlap with the same speed, suggesting that the two fragments ions are produced by the same dynamics. More surprisingly, the iodine signal rises again up to the same maximum observe at time overlap after around 20 fs. The second rise time appears much slower than the first, ranging around tens of femtoseconds. In the following we will first introduce the model used to fit these signals and then discuss about the interpretation with the support of the theory.

Model and fit

To model we used is the sum of two functions $f(t)$ and $g(t)$. It can be considered as a sum of different decaying curves, both convoluted with a gaussian instrumental function, which is dependent on the two pulses durations through its width. An example is reported in Fig. 4.5.

The first curve $f_{\tau_0}(t)$ is based on a single exponential decay and it is used to indicate the depopulation of a single state. The curve can be expressed analytically [92] by the following equation

$$f_{\tau_0}(t) = \text{erfc}\left(\frac{\sigma}{\tau_0\sqrt{2}} - \frac{(t-t_0)}{\sigma\sqrt{2}}\right)\exp\left\{\frac{\sigma^2}{(2\tau_0^2)} - \frac{(t-t_0)}{\tau_0}\right\} \quad (4.1)$$

The decay rate is expressed by the parameter τ_0, and it is convoluted with the cross-correlation term of our pulses, represented by the parameter σ of the cross-correlation width. t_0 represents the time origin. In Fig. 4.4, it is clear that the first peak in all fragments at the time overlap does not have a Gaussian character (represented by the grey dotted line), but it actually decays exponentially. The function $f(t)$ is used to model such behavior.

Table 4.1: Result of the main parameters for each fragment

	A_g/A_f (arb.)	τ_0 (fs)	τ_r (fs)	t_d (fs)
CH_3I^+	$\frac{4.8\times10^{-3}}{3.7\times10^{-2}} = 0.13$	5.5 ± 0.3	0.1 (fixed)	0 (fixed)
I^+	$\frac{6.31\times10^{-5}}{8.2\times10^{-5}} = 0.76$	29 ± 4	14 ± 2	27.3 ± 1.3
CH_3^+	$\frac{2.5\times10^{-4}}{1.03\times10^{-3}} = 0.24$	18.0 ± 1.7	23 ± 11	19 ± 5

The second contribution in Fig. 4.5 $g(t)$ needs to take into account the finite rise time of the second peak, which is observed in the iodine signal, after which it stabilizes to a constant value. To this purpose, due to the linearity of the convolution, we can use a combination of $f(t)$ functions to parametrize it

$$g(t) = A_g (1 - f_{\tau_r}(t - t_d)) \tag{4.2}$$

This equation expresses an exponentially rising curve, with rise time constant τ_r, which reaches a maximum constant value expressed by the parameter A_g. The time t_d indicates a shift in time in respect the half point of the rising in respect to the time origin. With a particular choice of parameters this model can applied to all the fragments: for instance, assuming the rising to be very short ($\tau_r \to 0$) the second curve can be used to parametrize a constant background switching on at certain time, to replicate the behavior of the parent.

The results of the best fit for each fragment are shown in Fig. 4.6 and summarized in Table. 4.1. In here, we will briefly describe the result of the fit, while we will give more details about the interpretation in the theory section. We have reported the ratios in between the two peaks (or constant background), as well as all the time constants and time delayed. The σ have been kept fixed in all the fit to the estimated width obtained by the known pulse durations. All the errors reported needs to be considered as standard error provided by the fit routine. For the parent the first curve $f(t)$ describes a very fast decays, decreasing over only 5.5 fs. In the case of the care, the curve $g(t)$ represents a constant background and for this reason the rising time τ_r has been fixed very close to zero. Such model describes a static reservoir of molecules which can be ionized and produce a stable parent ion. As we will describe in detail later with the theory, there are very few channels which can produce the parent ion, after the ionization, if we consider that the parent cation dissociates very easily. The constant background can, however, be easily explained if we include also 2UV photon excitation, which populates very high Rydberg states close to the ionization potential [93]. These states, mostly bound, possess a lifetime much longer than the time scale explored in this work, of the

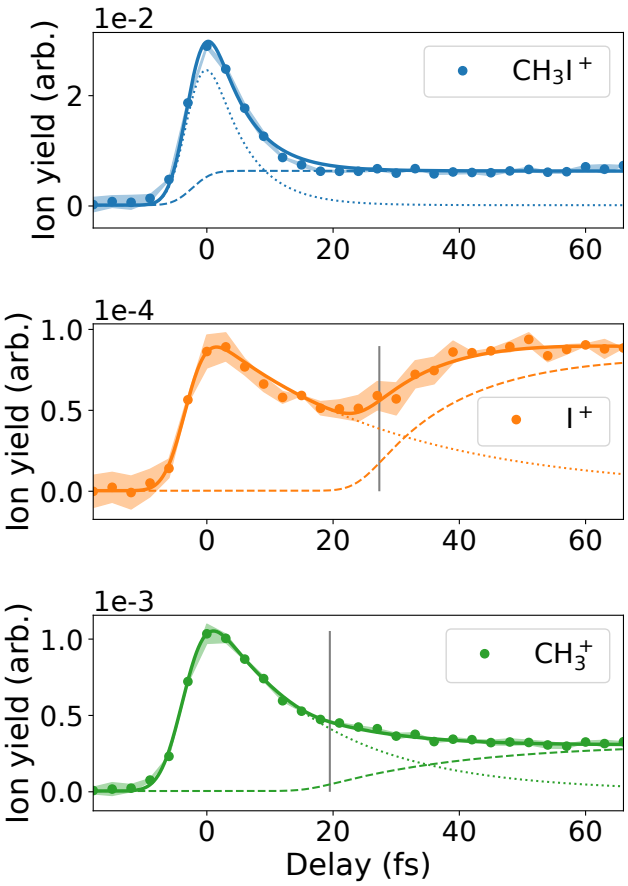

Figure 4.6: Experiment data (dots) for each fragment detected as a function of the pump-probe delay (absolute signal). Solid line in each plot represents the best fit obtained using the model described in text. Dotted line indicates the first term $f(t)$, dashed line indicates the second contribution $g(t)$. Grey dashed line in iodine and methyl signal indicate the time delayed estimated by the fit. See text for details.

order of ps. They will act therefore as a constant background, which is switched on only the 2 UV photons from the pump are absorbed.

The iodine fragment expresses at best the two contributions given by $f(t)$ and $g(t)$. The first decay is fitted well with a time constant of $\tau_0 = (29 \pm 4)$ fs. After $t_d = (27.3 \pm 1.3)$ fs, which is indicated in the figure by a grey line, a new contribution arises followed by exponential growth with a rising time of (14 ± 2) fs. This curve reaches a value which is 0.7 % of the initial peak.

For the methyl fragment, a similar dynamics can be observed. The signal rises to its maximum at the time overlap and then decays in the same order of magnitude as iodine, with a time constant of 18.0 fs. At a certain time delay ((19 ± 5) fs) a second channel appears, with a very slow rising time of $\tau_r = (23 \pm 11)$ fs. We note that the fit here gives a very high relative error.

The approach in the fit has been motivated by the following theory arguments, through which more detailed understanding of the neutral wavepacket dynamics can be obtained.

4.3 THEORY AND DISCUSSION

The potential energy curves for methyl-iodide have been calculated for the neutral with MOLCAS [94, 95] and optimized at CASSCF level. Relativistic effects are included by using a second order Douglas–Kroll Hamiltonian [96] formalism in combination with the ANO-RCC [97] basis set contracted to a triple zeta polarized (ANO-RCC-TZVP) basis set. The active space used in the CASSCF calculations is composed of 6 electrons in 4 orbitals. Specifically, the set of orbitals considered in this study contains two lone pairs of the iodine atom, σCI-bonding and σCI-antibonding. Finally, the energy was corrected by perturbation theory in its extended multi-state CASPT2 (XMS-CASPT2) formalism [98] with an imaginary shift of 0.3.

The result is reported in Fig. 4.7. In the neutral potential energy surfaces, the two main dissociative $^3Q_0$ and $^1Q_1$ are crossing, leading the well-known neutral photo-dissociation dynamics mediated by the conical intersection. The $^3Q_0$ correlates in the dissociation limit with I^*, while $^1Q_1$ correlates with I. The two main cationic states are highlighted: the ground state $X^2\,E_{3/2,1/2}$ shows a very steep potential barrier in respect the Franck-Condon region, of more than 2 eV which leads to dissociation towards CH_3^+ ion. The first excited cationic state, instead, shows a much weaker potential well and it leads to dissociation in I^+.

Absorption of 1 UV photon leads to the manifold of excited states associated to the A-band and it is responsible for the photo-dissociation dynamics. Since our bandwidth cover almost entirely the A-band, we do expect contribution by all the states. However, it is well known that the most favorable state is the $^3Q_0$ with a probability of 98 % [81].

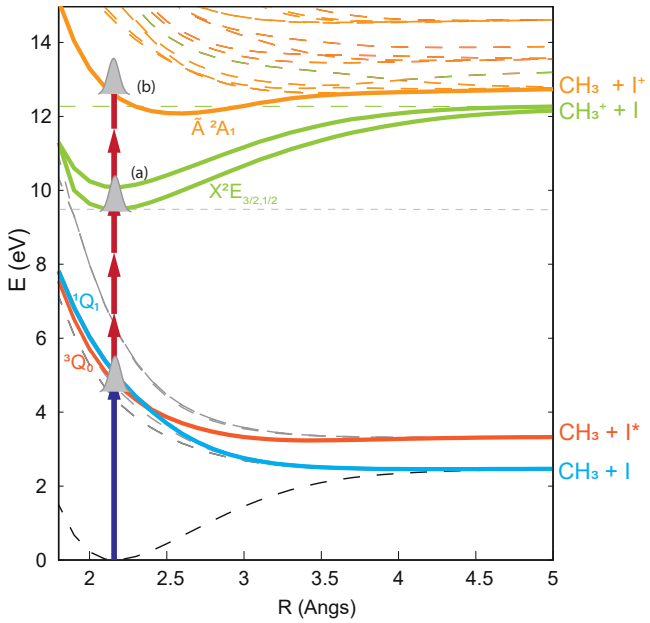

Figure 4.7: One-dimensional potential energy curves calculated for methyl-iodide, in the neutral and the for the lowest cationic electronic states. The neutral dynamics is occurring mostly on the two dissociative curves $^3Q_0$ and $^1Q_1$ to which we excited by the absorption of 1UV photon (blue arrow). Fragment production can occur by the absorption of either 3 or 5 NIR photons, reaching (a) the ground state of the cation $X^2\,E_{3/2,1/2}$ or (b) the first excited state $\tilde{A}^2A_1$.

Once the molecule has been excited the lowest amount of NIR photons required to ionize in the probing step is 3, resulting in the energy needed to reach the $X^2\,E_{3/2,1/2}$. Due the very high potential barrier required to dissociate after ionization, this channel is responsible for the production of the parent ion at time overlap and it has indicated by (a) in Fig. 4.7.

The observation of both methyl and iodine fragments at time overlap, however, suggest the presence of additional photoionization channels. In order to reach the first cationic excited state $\tilde{A}^2A_1$ at least 5 photons are required: it is known that this state correlates with the production of both fragments. It can lead to a minor production of I^+ because of the very low potential barrier - as shown in Fig. 4.7, but it also led to very slow (µs) internal conversion towards the lower ground state. In particular, this relaxation pathway transfer energy from the first excited state towards the vibrationally excited continuum of ground state $X^2\,E_{3/2,1/2}$. In this way, it has enough energy to overcome the barrier and produce the CH_3^+ fragment, as was addressed in a previous work [99]. Therefore, although 5 photons of the probe are populating the $\tilde{A}^2A_1$, due to the finite time spent in the mass spectrometer drift tube (also µs) the molecule will have enough time to transfer the energy and dissociating to the methyl fragment.

To address the time-dependent signal, full-dimension classical trajectory calculations were performed using a modified version of the surface hopping including arbitrary couplings (SHARC) method [100], which includes the surface hopping algorithm and the spin-orbit coupling. In this approach, the gradient of spin-orbit states is calculated as linear combinations of the spin-free gradients, neglecting the gradient of the spin-orbit coupling. Moreover, in the present case, the contribution of the non-adiabatic coupling to the gradient was also neglected. With this method, a large set of trajectories are calculated from the states corresponding to the A-band. Due to lower accuracy in calculating the transition moment in this band, all trajectories are launched with equal probability and are later weighted by the experimental UV spectrum. This is a good approximation, considering that transition moment has similar magnitude over this energy range [101]. Moreover, intrinsically in the surface hopping algorithm we can analyze the trajectories which goes specifically towards I (crossing on) and the one which lead to I^*.

To include in our model the multiphoton probing step, we estimated for each trajectory the ionization energy which would be needed to reach each specific cationic state. For each specific point in the neutral PES, it is possible to express the ionization energy. In other words, as the wavepacket evolves after the absorption of 1 UV we can quantify the amount of energy needed in the probing step, which will result in the production of each fragment. Calculating the probing step

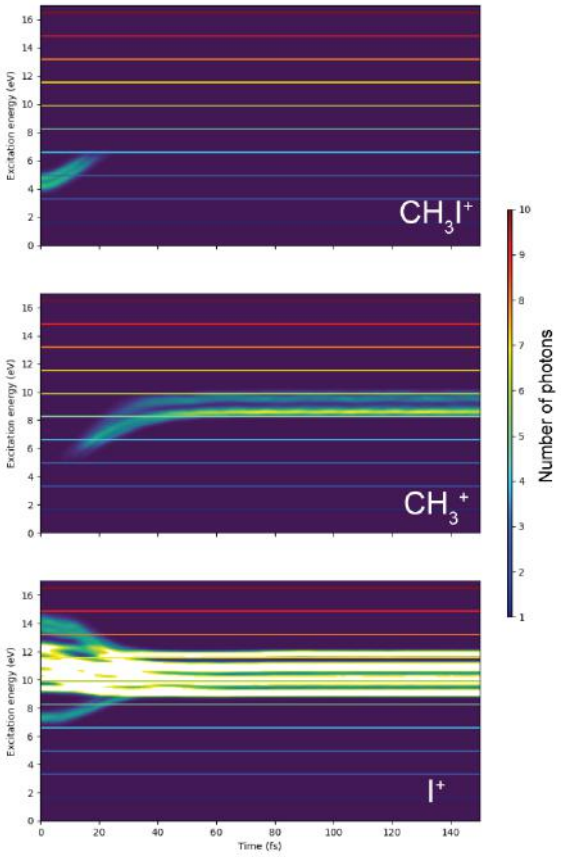

Figure 4.8: Number of trajectories obtained by full dimensional semiclassical calculation in the neutral as a function of time and ionization energy required for photoionization for each fragment. From top to bottom the panels show the available trajectories which can produce the parent, the methyl and iodine ions. Horizontal lines indicate effective energies available in the multiphoton probe step with increasing number of NIR photon (1.65 eV).

in the case of 3 or 5 NIR photons is not feasible for this molecule and therefore we will rely on such energetic argument to assign the observed signal.

Additionally, through this method, we compute the total energy acquired by the nuclear wavepacket during evolution. If the total energy is higher than the dissociation energy required to overcome the barrier in the cation, a specific fragment will be produced after the ionization, as stated in the following

$$E_{kin} + E_{pot} \geq D_i \tag{4.3}$$

where the sum of E_{kin} and E_{pot} represents the total energy and D_i the dissociation energy for a specific fragment.

The results of these calculations are reported in the three panels of 4.8. The color bar measures the number of trajectories, as a function

of time and ionization energy (energy difference in between the actual PES and the respective cationic state), in which the total energy is above the dissociation energy, i.e., have enough energy to dissociate after ionization. The central and bottom panels indicate the trajectories which possess enough energy to dissociate - after ionization - towards methyl CH_3^+ and iodine I^+. In other words, they represent the trajectories for which Eq. 4.3 is satisfied. The top panel, instead, is obtained by the total number of trajectories by removing the previous and indicates the number of trajectories which produce a stable parent ion.

To understand the parent, we focus on the first panel. The absorption of 3 NIR photons is required to reach the ground state of the cation ($X^2E_{3/2,1/2}$), which can produce either parent or methyl depending on the total energy acquired through the evolution. At time overlap, when the probe pulse arrives before the evolution has started, it has not enough kinetic energy to dissociate after ionization. For this reason, most of these trajectories will produce a stable parent ion. After around 20 fs there are no more trajectories which can produce the CH_3I^+ since all the trajectories have acquired enough kinetic energy.

As the molecule evolves in the neutral, the parent shows a very rapid decay < 10 fs (Fig. 4.6, left). This decay time represents the convolution in between the steepness of the neutral curves and the steepness of the cationic states. Since the neutral potential is very steep, when we let the molecule evolve on the neutral PES, it will require more and more energy to reach the ground state of the cation, decreasing the number of ionized molecules. At the same time, the same transition towards the ground state of the cation will produce methyl fragments, as can be observed from the central panel.

The bottom panel instead shows all the trajectories which can produce iodine ions. It shows several overlapping trajectories, which are all contributing to the production of the fragment depending on the number of photons required. To obtained a clearer understanding, we integrated the different trajectories contribution by considering the different number of NIR photons required to reach a specific cationic state. We must stress that this calculation no information regarding the probe cross-section is available and therefore all of these contributions will not contribute equally.

Firstly, we observe that for the parent a signal is produced only with the absorption of 3 and 4 photons. In particular, only the 3 photons signal matches the very rapid decays observed experimentally.

For methyl, the slow rising component which is observed experimentally is clearly matching the integrated curves matching 6 photons. The time delay we extracted from the experimental was giving a value of $t_d = 19$ fs (Fig. 4.6), which is very close with the starting time in the theory.

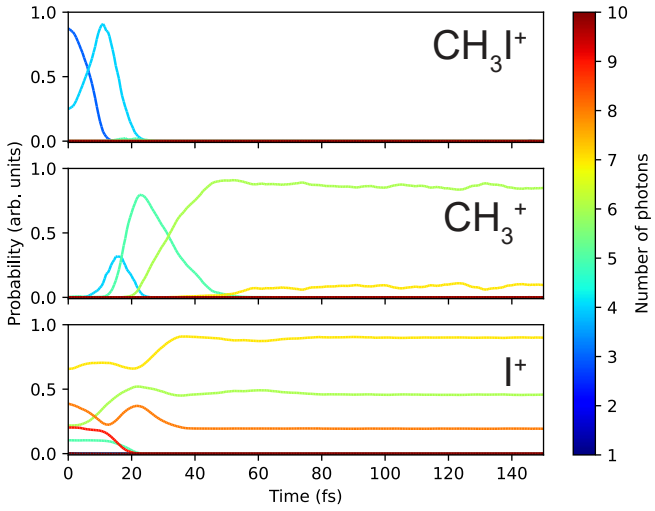

Figure 4.9: Integrated number of trajectories for each number of photons. The different panels represent the integrated signal for each fragment, as shown in figure 4.8.

For iodine instead, we do observe several and very different curves. In particular, we see relatively fast decays before 20 fs, and very late rising such as the yellow curve for 7 photons. Experimentally, the second rising from Fig. 4.6(central panel) was $t_d = 27.3$ fs, which indicates the starting time for the second rising in the orange curve. Although we have no information about the weights all the different contribution in Fig. 4.9 should be combined to obtain the experimental signal, we can clearly state that the 7 photons contribution appears to be dominant, since it is the one which shows a strong second rising at the same time of the experimentally observed curve.

When looking at the neutral potential energy surface, the extracted time delay occurs after the neutral molecule has reached the conical intersection, therefore we might conclude that what we are probing is happening after the CI.

5

ULTRAFAST RYDBERG STATES DYNAMICS IN ACETONE

A main aspect of using few-fs UV pulses is the possibility of triggering ultrafast electronic dynamics by coherently exciting several electronic states of a molecule. The work included in this chapter regards the dynamics which is triggered by exciting a coherent superposition of Rydberg states in acetone.

This experiment was performed in spring 2021. I did extensive research for using acetone as target, conceived the experiment and run the full experimental campaign with . I took care of data analysis presented, except for the covariance mapping analysis which has been carried out by my colleague Krishna Saraswathula.

5.1 INTRODUCTION AND PREVIOUS WORK

The second investigated molecule is acetone $(CH_3)_2CO$, also known as dymethyl ketone, represents the simplest structure of the ketone, a functional group with the structure R_2CO. Acetone has a total mass of 58 au and an ionization potential of 9.71 eV. The photophysics of the molecule is characterized by a relative strong single photon UV absorption band (cross-sections around $1 \times 10^{-20}\,\mathrm{cm}^2$), as a transition from the ground to the first excited state, S_1 [102]. The subsequent induced dynamics is known in literature as Norrish Type-I cleavage of the $\alpha - CC$ bond, as it is quite fundamental in many aspects of organic chemistry, such photooxidation of polymers. The breaking of one of the two $C - C$ bond in acetone creates an Acetyl $(CH_3)CO$ (mass 43 au) and a Methyl CH_3 (mass 15 au).

Several ultrafast studies focused their attention on the dynamics in highly-excited states, close to the ionization potential of the molecule. In particular, since the molecule is considered relatively flexible, in this region it possesses many different dissociation pathways which have been extensively investigated both theoretically [103] and experimentally [104]. These excited electronic states, which are usually assigned to the Rydberg manifold, are strongly observed via VUV absorption, with the first transition of the series observed at 194 nm. Without going too much into details of the structure of these states, CC bond cleavage can be observed after excitation to any of those states, as the result of very complex and intertwined electronic structure.

In addition to single photon VUV excitation, multiphoton excitation has been used to access these states. In [105], study an underlying femtosecond dynamics on the S_1 states towards CC bond cleavage,

they additionally excite the molecule with different wavelengths across the S_1 absorption band in 250 nm to 320 nm. What they surprisingly reported is that the S_1 dynamics is hidden by another evolution which was triggered by the absorption of two photons, which they assigned to transition towards different Rydberg states, depending on the excitation wavelength. They also state that previous interpretation of the S_1 dynamics might have been affected by the two photons absorption [106]. More favorable two-photons excitation is attributed to a lower absorption cross-section to the S_1 and the cumulative very large cross section to the Rydberg manifold, which might even enhance when using femtosecond pulses with high peak power.

For pump wavelength shorter than 306 nm the two photons excitation towards the $3d_{yz}$ showed the presence of a small potential energy barrier of 0.4 eV, which is formed by an avoided crossing with the valence $\pi\pi^*$, which is observed for the first time experimentally, but it was previously reported theoretically [107]. In this theoretical and experimental work, they calculated the different potential energy surfaces in the energy region from 7.0 eV to 10 eV, which we also reported in Fig. 5.1 as a function of the $C-O$ reaction coordinate.

From the calculated potential energy surfaces, the dynamics is very well justified by the presence of several conical intersections in between the $4^1A_1\,(\pi\pi^*)$ and the Rydberg states. Depending on the different Rydberg state reached, the crossing the valence state can bring the molecule very easily to different configuration.

In 2017, using 8 eV VUV excitation and Photoelectron-photonion Coincidence (PEPICO) detection, Couch *et al.* have been able to identify the relation in between the $3p$ Rydberg and $4^1A_1\,(\pi\pi^*)$ in a time scale of hundreds of femtoseconds [108]. They exploited high energy photons for probing towards higher cationic states. In this way, they are able to observe the π character of the valence state. Additionally, time-resolved spectra revealed that this state decays in 330 fs, either towards a low-lying state or fragmenting into acetyl.

Precise excitation to the valence $4^1A_1\,(\pi\pi^*)$ was attempted by Uenishi *et al.*, where they increased the excitation pump energy to 9.3 eV and probe with 4.7 eV [109]. To our knowledge, it is also the experiment performed with the shortest time resolution of 25 fs. By measuring time-resolved photoelectron VMI images they separated the two contributions, in particular based on the broad bandwidth and low anisotropy of the valence state in respect to the Rydberg states, while exploiting a forbidden transition in between the Rydberg and the highest cationic states D_1. The photoionization signal associated to the $4^1A_1\,(\pi\pi^*)$ exhibited a very fast decay of 8 fs. The experiment is also able to resolve many Rydberg states which shows a peculiar flat-top shape, of duration of around 50-100 fs which is attributed to

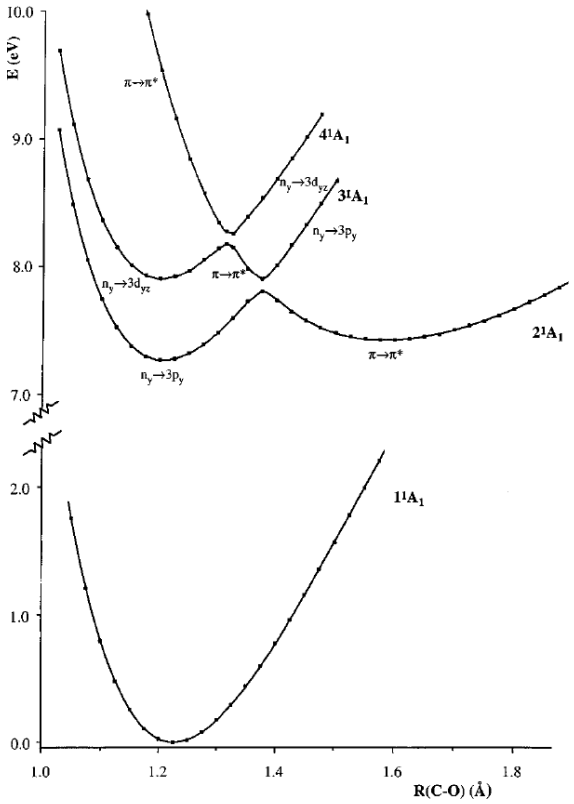

Figure 5.1: Potential curves for the highly excited states of Acetone of ${}^1A_1$ Symmetry, which express in particular the interaction in between Rydberg states ($3p$, $3d_{yz}$) and the valence 4^1A_1 ($\pi\pi^*$) state through the presence of Conical intersection (represented here with a small energy gap, for clarity). Ionization potential for acetone is 9.7 eV. Adapted from [107].

intramolecular vibrational redistribution and cannot be resolved with their time resolution.

Very recently, Forbes *et al.* claimed that $4^1A_1\,(\pi\pi^*)$ cannot be detected with probe photon energies below 8 eV and they attributed the broad low kinetic energy in their photoelectron experiment (pumped at 8.09 eV) to a previously not observed $A_2(n\pi^*)$, with the support of advanced quantum dynamics simulations. They propose a dynamical relaxation mechanism in which the prepared $3d_{yz}$ and $4^1A_1\,(\pi\pi^*)$ ensue internal conversion to intermediate Rydberg and towards the $A_2(n\pi^*)$.

Our work focuses on addressing the highly excited states of acetone with the use of the few-fs UV pulses. Its bandwidth allows to excite the molecule and probe the dynamics with unprecedented time resolution.

5.2 EXPERIMENT

The experimental pump-probe scheme is the following. Acetone molecules are excited through 2 UV photons at 250 nm absorption. Since the molecule is excited to states which are close to the ionization potential, a single NIR pulse is used to ionize and probe the dynamics. The UV pulses used for the excitation are the same as discussed in Ch. 3.1.3. Briefly, the photon energy is centered at 4.9 eV and it has a FWHM of 0.8 eV. In a very simplified picture, simultaneous absorption of two photons will have an effective energy of 9.8 eV, which is higher than the ionization potential of acetone. In all measurements, it will create a static contribution of direct pump-only photoionization. The low energy part of the two photons spectrum, however, matches the energies of the highly excited states shown in Fig. 5.1. In particular, it will be comparable to the spectrum used in [109] and therefore we do expect to populate similar states.

These Rydberg states are shown in Fig. 5.2, where we compare the tail of the 2 photons excitation to published synchrotron 1 photon cross-section. In black, it is represented the absorption spectrum of vapor acetone obtained by synchrotron measurements, adapted from [110]. The different Rydberg series with a minimum $n = 5$ up to $n = 14$ are assigned to several peaks observed here. The blue line represents the tail normalized 2 UV photons excitation. The effective 2 photons spectrum is obtained by doubling the UV spectrum characterized in sec. 3.3.2. In this way, even if the two photon transition is not available, we are able to narrow down several states which might be involved in the triggered dynamics. These states will be of higher energies (high n) than previously reported in literature, especially the ones with pump energy in the region of 7.0 eV to 8.0 eV [108]. Among these states we expect to reach the valence $4^1A_1\,(\pi\pi^*)$, for which the vertical

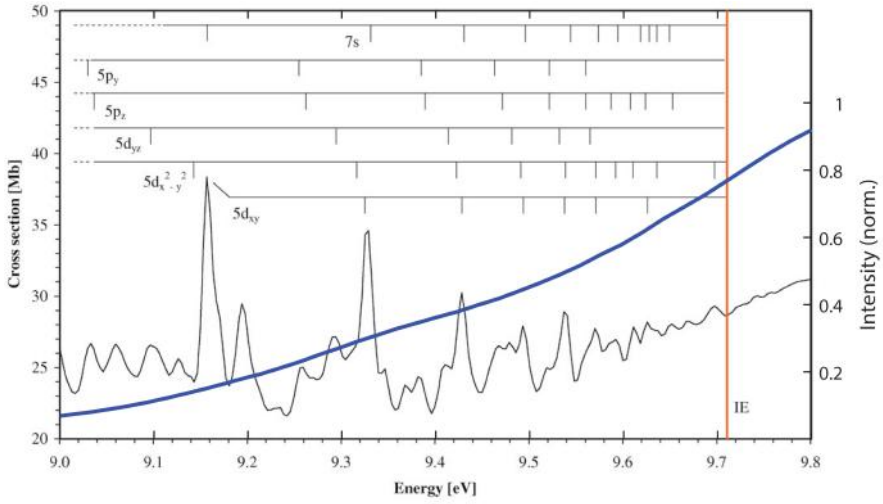

Figure 5.2: In black, the absorption spectrum of acetone in gas phase in the 9.0 eV to 9.8 eV region and assigned Rydberg states from Synchrotron measurements. Adapted from [110]. The solid blue line represents the tail of the effective two photons excitation spectrum, which is obtained from doubling the spectrum in Fig. 3.15 (b). The region of interest for the excitation step in this simple picture starts with the $n = 5$ Rydberg states and goes up to the ionization potential, which is marked by the vertical orange line.

excitation energy was estimated to be at 9.2 eV, as also reported in [109].

The probe spectrum employed is reported in Fig. 3.2. In terms of photon energy, it is centered at 1.65 eV extending from 1.2 eV to 1.8 eV. Being very close the ionization potential basically every component of the NIR probe can lead to ionization, due to the very small distance of the Rydberg states from the cationic ground state, for which the maximum energy difference is0.6 eV.

Experimentally, acetone vapor (purity 99.9%) was delivered to the experimental chamber by exploiting free vapor expansion at room temperature through a needle and a skimmer, without using a buffer gas. The distance in between the needle and the skimmer, and additionally with a variable leak valve can be used to control the amount of vapor diffused in the experimental chamber. Good signal was achieved with a pressure of 2.49×10^{-6} mbar (baseline pressure without target 1×10^{-7} mbar).

20 nJ to 60 nJ energy per pulse UV are focused in the interaction chamber with a 90 cm focal length, which corresponds to intensity in between $1.0 \times 10^{12}\,\mathrm{W\,cm^{-2}}$ to $7.0 \times 10^{12}\,\mathrm{W\,cm^{-2}}$, if we consider a pulse duration of 4 fs. Several pump-probe acquisitions have been performed in this intensity range with no change in the actual dynamics, therefore the highest intensity has been chosen in order to provide the highest number of excited molecules and therefore the best signal-to-noise ratio.

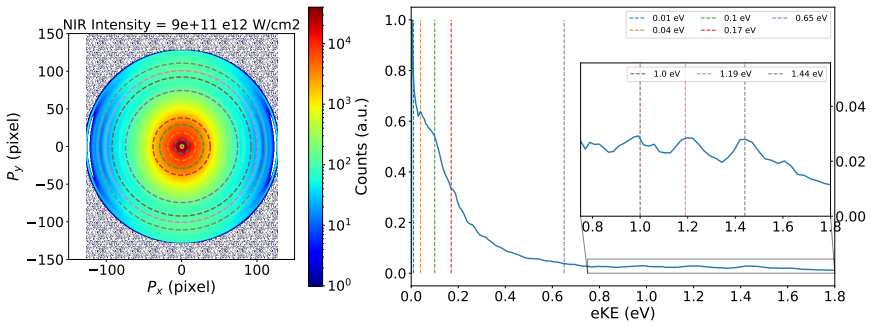

Figure 5.3: *left*: Photoelectron angular distribution obtained in acetone when pump and probe overlap in time. Pump and probe intensity were $3 \times 10^{12}\,\mathrm{W\,cm^{-2}}$ and $9.0 \times 10^{11}\,\mathrm{W\,cm^{-2}}$ respectively. Photoelectrons counts in a logarithmic scale to enhance the feature at higher kinetic energy. Circles depicting different kinetic energy region follows the color code in the legend of the right figure. *right*: angularly integrated photoelectron kinetic energy distribution of the left VMI image. Dashed lines identify specific energy values associated with peaks of interest.

The probe pulse was focused by a toroidal mirror (see 3.1.2) non-collinear with the pump. The intensity of the probe could be varied with a motorized iris in between $9.4 \times 10^{11}\,\mathrm{W\,cm^{-2}}$ to $1.23 \times 10^{13}\,\mathrm{W\,cm^{-2}}$. The lowest intensity value provides negligible counts when ionizing the NIR only. This value has been chosen for the time-dependent scans to provide a probe-free background. The probe duration has been independently compressed by using fused silica wedges and looking at the NIR only ionization signal for high intensities. The optimum duration is estimated before the beamline with an SH-FROG setup, resulting in 5.5 fs. Estimated cross-correlation FWHM for the two pulses is 6.5 fs when considering a 2UV + 1NIR process, estimated using the expression (3.7) and the pulses durations reported previously.

For the experiment we recorded simultaneously and single shot mass spectra and electron velocity map imaging to perform covariance analysis on the fragmentation path. Both sides of the spectrometer are calibrated using simulation in SIMION.

5.3 STATIC

As a typical measurement, Fig. 5.3 reports the velocity map image acquired when pump and probe overlap in times.

All of the images discussed in the following are acquired integrating over 60 000 laser shots. They are symmetrized along the top-bottom and left-right direction. A median filter and baseline subtraction is performed before Abel inverting using the r-basex method from the

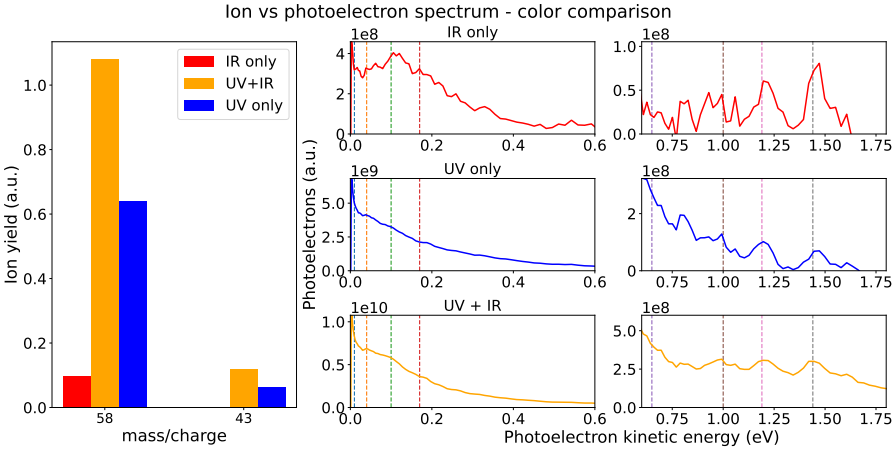

Figure 5.4: *left*: ions yield of the parent (mass 58 au) and acetyl fragment (mass 43 au) when ionized with IR only (red), UV only (blue) and both temporally overlap (orange). Laser intensity is the same as Fig. 5.3. *right*: Associated angularly integrated kinetic energy spectra for the same acquisitions. Energy regions are separated to enhanced high kinetic energies features. Both ions and electrons are recorded simultaneously. Dashed vertical line indicates the same energies identified in Fig. 5.3.

PyAbel package. The overall area covers an energy range of around 1.8 eV. Considering the probe energy and the targeted states, this is enough to observe the dynamics induced by the absorption or 1 or 2 NIR photons. Due to the very high density of Rydberg states, in addition to the very large bandwidth from the short pulses no clear peaks are visible, but we can distinguish two main kinetic energy regions: most of the signal is enclosed in a 0.8 eV energy radius, while a higher energy band is visible for energy above 1 eV.

The intensity of the latter is almost two orders of magnitude lower than the low kinetic energy region. For the same condition (UV+IR), both the parent (mass 58 au) and the acetyl (mass 43 au) ions are detected, with the latter being only 10% of the former, while Methyl ions yield is negligible.

Fig. 5.4 shows the yield for the two ions detected for pump and probe at time overlap and for each individual pulse as well, by keeping the same conditions. On the right side of the figure, the corresponding angularly integrated photoelectron spectra are reported. Signal level for IR only is almost one order of magnitude than the two colors signal. Single NIR ionization requires 6 photons, and it is therefore not very likely. No additional fragmentation is observed in this case. Pump only signal is mostly due to two photon ionization, since, as we discussed part of the 2UV excitation spectrum is higher the ionization energy. The acetyl fragment is also observed in this case, suggesting that it also accesses a higher dissociative cationic state, which would require a higher number of photons. By using pump and probe

together both the yield of the parent and the acetyl are enhanced, with the latter twice as the single color yield. Similar information can be deduced by the electron spectra. Considering the total signal, two colors signal is increased by almost two orders of magnitude. Low kinetic energy electrons are observed in the three cases: UV only and UV+IR shows matching peaks, whose height decrease with the kinetic energy, while for IR only the structure is different, peaking at 0.118 eV. The behavior at the high kinetic energy region shows similar behavior in which very lower signal is observed for IR only and UV only, and signal is enhanced when both pulses are present. In this region, however, we observe similar peaks in all the three cases.

5.4 PROBE INTENSITY SCALING

In order to identify the correct photoionization process at play, ions mass spectra and electrons VMI have been acquired by keeping the pump fixed and varying the probe intensity, with no delay in between the two. UV intensity has been fixed to $3 \times 10^{12}\,\mathrm{W\,cm^{-2}}$, while NIR intensity is varied in between $9.4 \times 10^{11}\,\mathrm{W\,cm^{-2}}$ to $1.23 \times 10^{13}\,\mathrm{W\,cm^{-2}}$. To evaluate the particular number of photons involved, we measured from the mass spectra the yield of each fragment and from the photoelectron spectra the integrated yield in two energy regions of width $= 0.4\,\mathrm{eV}$, centered at 0.1 eV and 1.4 eV for the low and high kinetic energy electrons, respectively. Each intensity values have been repeated, resulting in standard error of 1% for the ions and 0.04 % for the electrons. For each one of this signal s (parent, fragment yield, electron yield in low and high kinetic energy regions) we reported the value $y = \log_{10}(s - s_{UV})$ as a function of $x = \log_{10}(I)$ where I is the NIR intensity in Fig. 5.5, together with a linear regression $y = mx + q$.

All the different signals rise with an angular coefficient very close to one, which validates our initial guess of a single NIR photons needed for ionization. This result also indicates that the target is excited to states which are very close to the ionization potential, confirming at the same time the 2UV photons excitation [105]. We note that for electrons we decided to limit the analysis only on two regions to increase the signal to noise, but the results are consistent also for the individual peaks identified before.

5.5 TIME RESOLVED MASS SPECTRA

For the time-resolved scan, UV intensity has been set for the maximum ($3 \times 10^{12}\,\mathrm{W\,cm^{-2}}$), while the NIR probe for the minimum value of $9.4 \times 10^{11}\,\mathrm{W\,cm^{-2}}$. It has been chosen to avoid multiphoton ionization through from the probe only. In fact, the signal produced only by the NIR pulses is almost one order of magnitude lower than the two colors (Fig. 5.4).

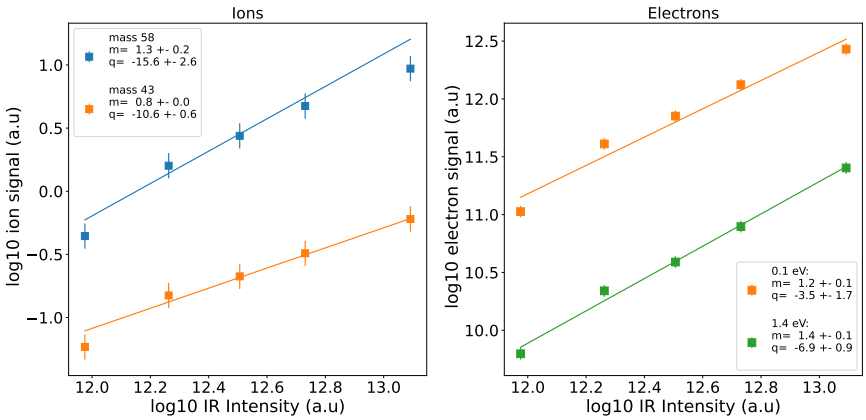

Figure 5.5: Fragments and electrons yield scaling with the probe intensity, at time overlap between UV and NIR. NIR intensity is varied in between $9.4 \times 10^{11}\,\mathrm{W\,cm^{-2}}$ to $1.23 \times 10^{13}\,\mathrm{W\,cm^{-2}}$. UV intensity was kept fixed at $3 \times 10^{12}\,\mathrm{W\,cm^{-2}}$. Pump only signal is subtracted by each point. On the left, error bar shown corresponds to 1%. Electron yield is obtained by energy integrating the photoelectron distribution around the energy value shown in figure, with a width $\pm 0.4\,\mathrm{eV}$, with an error bar of 0.5%. The results of a linear regression, including standard deviation for the parameters are shown. Both the fragments and the electrons confirm the 1 photon probe interpretation.

We will first focus our discussion on the dynamics of the fragments.

A series of mass spectra have been acquired with a time step of 3 fs for the pump - probe delay, which has been computer controlled through a piezo. Each time point is the result of integrating over 60 000 shots and each full time range scan has been performed going forward and backward to average out sources of slow external systematic error, such as pressure change for the target or laser fluctuations. The error bar reported in the following figures represents the standard deviations in between scans. We reported in Fig. 5.6 the results of such acquisition, where we have represented the signal associated with the Parent and the Acetyl fragments. Positive delays indicate probe pulses coming after the pump.

The baseline for the negative delay has been subtracted to each ion signal, since it mostly contains UV only contribution. Time origin has been shifted to match the maximum of the parent signal.

The behavior observed in the two fragments is very different: where the two pulses are overlapping, they both rise very quickly to the maximum, while as soon the pump-probe delay is increased the parent yield decays and the Acetyl fragment stays stable. This behavior has been observed already previously for longer time [105], in which the parent ion showed always a faster decay than the Acetyl fragment. To evaluate the fast decay, the two traces have been independently fitted to a function model which comprises two contributions: (i) a gaussian

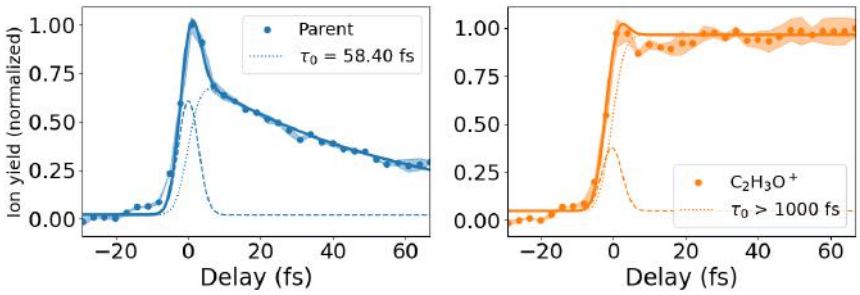

Figure 5.6: Time resolved ions yield for the parent ion (left) and Acetyl fragment (right) of acetone as a function of the UV pump -NIR probe delay. Positive time means the probe is arriving later. Shaded area represents the standard deviation of repeated measured. Solid line in each plots represents the best fit obtained as a sum of a Gaussian contribution (dashed line) and an exponential decay with time constant τ_0 (dotted line), see text for details.

function of width σ and (ii) an exponential decay of time constant τ_0, which can be expressed by the following

$$\begin{aligned} f(t) =& A_0 \exp\left\{-\frac{(t-t_0)^2}{2\sigma^2}\right\} + \\ &+ A_1 \operatorname{erfc}\left(\frac{\sigma}{\tau_0\sqrt{2}} - \frac{(t-t_1)}{\sigma\sqrt{2}}\right) \exp\left\{\frac{\sigma^2}{(2\tau_0^2)} - \frac{(t-t_1)}{\tau_0}\right\} \end{aligned} \tag{5.1}$$

where t_0 and t_1 represents independent starting time for each contribution, and A_1 . The first term represents direct photoionization given by simultaneous absorption of 2 UV + 1 NIR from the ground state and it is often recall as the cross-correlation term. The second term represents an exponential decay with time constant τ_0 which has been convoluted with the gaussian of width σ, representing the instrument response function. This analytical expression has been used to optimize the evaluation, instead of using convolution methods [92]. We note that in our fit routine the width σ is the same in both terms and it has been fixed to the expected width as one would obtain estimating it through equation (3.7) and assuming a 2 UV + 1 NIR and including our pulse durations. We note that in this way the only free parameter of the Gaussian term is the amplitude. In particular for the parent, the estimation of the width matches very well the first term, confirming once again our interpretation of the pump-probe excitation scheme.

In a very simplified picture, the parameter τ_0 represents the decay time of the state which is populated by the pump, and which is then probed by the second pulse. In our case, the second pulse ionizes the molecule with a transition from the excited state to a cationic state. The cationic state involved can undergo its own dynamics after the probe has removed the electron: it can be stable, for instance, in which

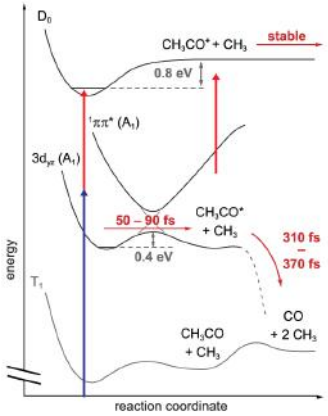

Figure 5.7: Proposed scheme for the interpretation of ions signal for acetone: ionization with the NIR pulse when the pump and probe are overlapped in time leads to a bound region of the cationic ground state, and therefore we observe a maximum for the parent signal at time zero (left red arrow). When the NIR pulse comes at later time, the molecule has evolved and the absorption of a NIR photon (right red arrow) leads to a part of the potential which is dissociative producing charge acetyl, therefore leading to a decay in the parent signal. PES positions are not on scale, adapted from [105].

case the parent ion is preserved all the way to the detection or it can be dissociative, i.e., favors the breakage of the molecule. Since the detection of ions occur after several microseconds - due to the drift tube - ion yield measured here is the results of the pump - probe dynamics, certainly, but also the subsequent cationic outcome.

Indeed, what we observe is that the parent signal is decaying within (58 ± 2) fs from the excitation, while the Acetyl signal rises and then remains constant over more than 60 fs. In terms of cationic dynamics, this means that after 58 fs the evolution of the excited acetone molecule has reached a point from which the subsequent absorption of 1 NIR photon brings the molecule in a dissociative region of the cationic potential. In turn, less and less parent ion will be detected, because by the time they reach the detector they have already dissociated to acetyl ion. To stress this point, acetyl ion cannot be produced by the neutral photodissociation process [108].

To qualitatively support this interpretation, potential energy surfaces of acetone in the Rydberg region are reported in Fig. 5.7 [105]. For simplicity we only consider the Rydberg $3d_{yz}$ and the valence $4\,^1A_1(\pi\pi^*)$ as an example of our interpretation, although they are not the state excited during our experiment. If the probe comes at the same time as the pump (left red arrow) the molecule is promoted to a bound part of the potential curve of the cation, which allows us to observe a strong signal for the parent at time zero. If the probe comes at a later time, however, the molecule has time to evolve, in particular

going through the conical intersection in between the Rydberg state and the valence moving away from the Franck-Condon of the ground state. The absorption of a NIR photon from this position (right red arrow) brings the molecule in a part of the ground state cation which is dissociative, producing acetyl ion and neutral methyl, and therefore reducing the yield of the intact parent.

Therefore, through this proposed scheme the parameter τ_0 is related to the evolution of the neutral wavepacket from the FC to a region from which the probe can access directly a dissociative part of the cationic potential. In particular, the value we obtained agrees with the range 50 fs to 90 fs proposed by Huter *et al.* in [105], in which they estimated this time as a delayed rise time of the acetyl signal in a 2UV + 1 VIS experiment for lower Rydberg state.

This interpretation should be reflected as well as a delayed rise time for the acetyl, which we do not observe in our experiment. In our case (Fig. 5.6), instead both the acetyl and the parent reach the maximum signal simultaneously. This could easily be interpreted by the very small potential barrier in the cation (0.8 eV) which can be overcome through the higher energy component of the probe pulse. In addition, from 5.2, we identified a Rydberg states region which is higher in energy than the one investigated in [105], which in turn would increase even more the excess energy of the molecule after the removal of the electron. The fact that the decay measured matches the range observed even with different excitation range might indicate that the overall decays does not depend on which particular Rydberg state is populated, but more on the position of the crossing or the steepness of the cationic state reached. Certainly, understanding which states contributes to the overall dynamics is not possible without a full simulation considering at least the 2 UV excitation. On this matter, full *ab-initio* calculation is currently on going, in collaboration with the group of Fernardo Martin García from IMDEA Nanociencia. Nevertheless, experimentally, more information can be provided by analyzing the photoelectrons distribution.

5.6 TIME-RESOLVED PHOTOELECTRON ENERGY DISTRIBUTION

One of the main advantages of photoelectron spectroscopy is the possibility of resolving in energy (see Sec.2.2), which reveals the energy structure of the target.

A series of Velocity map images of the emitted photoelectrons have been acquired simultaneously with the mass spectra shown in the previous section. As such, each VMI image has been integrated over 60 000 shots and the full scan has been repeated backward-forward to averaged out any slow drift in the signal. Each image has been symmetrized top-bottom, left and right, and a median filter and baseline subtraction is applied. Abel inversion is performed with the

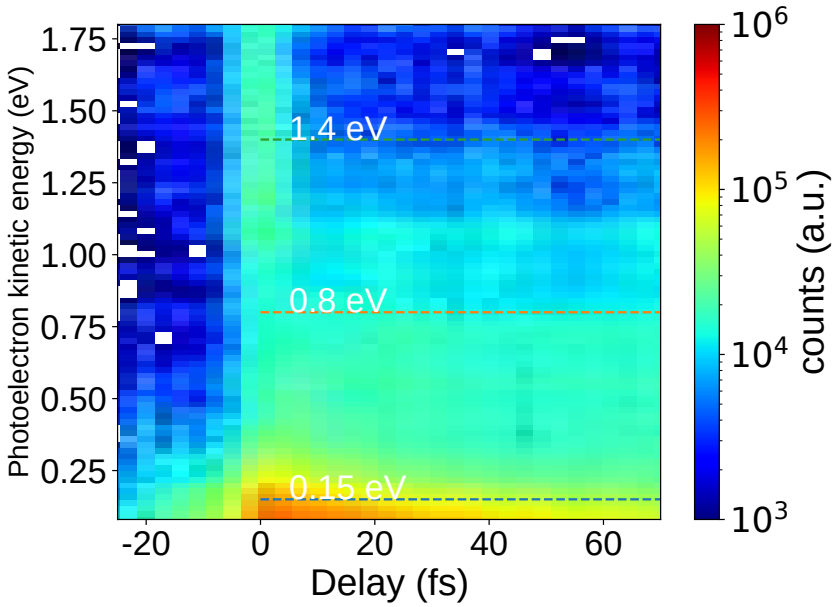

Figure 5.8: Angularly integrated photoelectron energy distribution as a function for the pump-probe delay. We can distinguish three distinct energy regions with different dynamics: a quick decaying low kinetic energy centered at 0.15 eV, a slower intermediate region at 0.8 eV and a sharp high kinetic energy at 1.4 eV. For energies around 1.1 eV the electrons show clear modulations for positive delay. Positive delay indicates probe after. The first negative delay spectrum has been subtracted from the map to enhance the time dependent signal.

r-basex method from the PyAbel package. Afterwards, the VMI image is integrated angularly and plotted as a function of pump-probe delay, as shown in Fig. 5.8.

Three regions can be distinguished in the map. The first one, where most of the signal is observed, covers the low kinetic energy range from 0 eV to 0.35 eV. As a function of time, it rapidly increases up to the maximum at time overlap and decreases immediately with a very quick decay of around 50 fs. A second intermediate region, which is less intense, is centered at 0.8 eV. It presents a slower rising in respect to the previous and stays almost constant after reaching its maximum at time overlap. Lastly, a higher kinetic energy range, extending from 1.2 eV to 1.75 eV, is characterized by a sharp peak around the time overlap.

In order to extract quantitative information on the decays, the three regions have been energy-integrated with a width of ± 0.2 eV). The integrated signal is reported in Fig. 5.9, where each trace has been fitted with the model described before for the ions (Eq. (5.1)).

Indeed, the low kinetic energy region shows the fastest decay with the best fit curve providing a decay (49 ± 3) fs. This decay value is

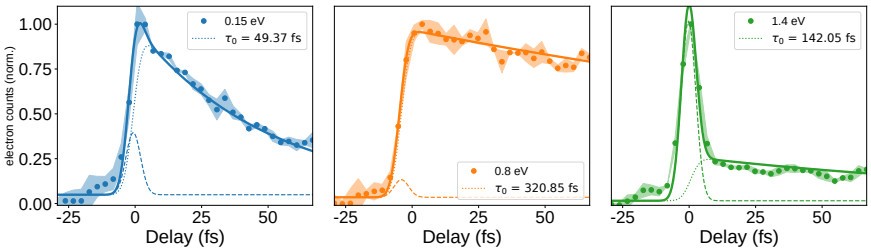

Figure 5.9: Integrated electron spectra in the three energy regions centred at 0.15, 0.8 and 1.4 eV, respectively (dots). Shaded area represents the standard deviation over 2 scans. Each trace has been normalized to the maximum. Solid line represents the best fit function using expression (5.1), consisting in a Gaussian and an exponential decay term.

similar to the one observed for the parent and, even though in the case of the photoelectrons the Gaussian term is less strong, it is a first suggestion that these electrons might be related to the parent (as it will be confirmed with covariance 5.7). The second region, centred at 0.8 eV shows the longest decay of (320 ± 44) fs. We note that this value is affected by a strong error because of the time range chosen for the scan and it can be intended as an indication only. The last region of interest, for high kinetic energy shows a very strong Gaussian component, which is fitted quite well by our independent estimation of σ_{cc}. This contribution might be related to the direct ionization from the ground states, for which a specific cationic state is accessed only when the two pulses are overlapped. The most exciting observation, in particular for at the intermediate and high kinetic energy curves, is that after excitation, the decay is strongly modulated.

5.6.1 *Coherent dynamics*

Several scans have been performed in a larger time interval reaching roughly 160 fs from the overlap, with step of 3 fs. We will first identify more clearly the energy range where we observe oscillations. NIR probe intensity was kept $1.2 \times 10^{12}\,\mathrm{W\,cm^{-2}}$, as the minimum value available for these measurements. Two scans have been acquired (forwards and backwards), with each point of the scans acquired over 60 000 shots. VMI have been processed as previously described and the result of these acquisitions is reported in Fig. 5.10 (a).

We still distinguish the same energy region described in the previous section. The low kinetic energy electrons, up to 0.3 eV, are decaying very quickly after a very fast rise time. We note that the Gaussian component in this scan is more easily observed, most probably because due to the higher probe intensity. The intermediate region at 0.8 eV shows still the slowest decays of the three, appearing almost constant

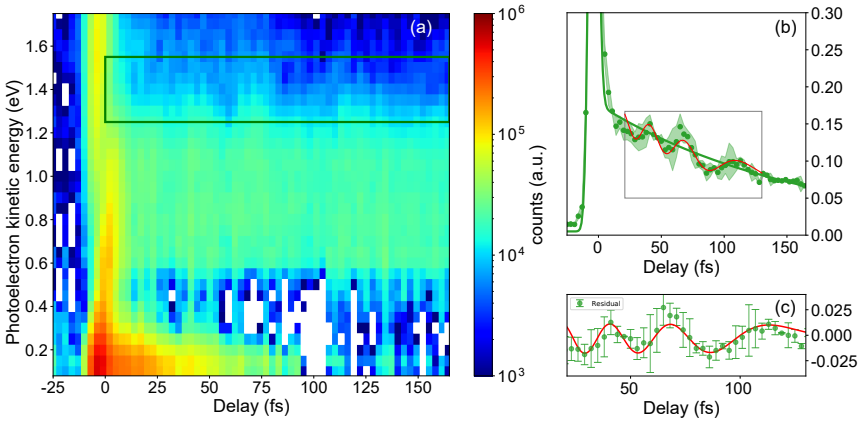

Figure 5.10: Long range acquisition with a focus on vibrational oscillations of acetone (a) Angularly integrated photoelectron energy distribution as a function of the pump-probe delay (extended range). NIR intensity was $1.2 \times 10^{12}\,\mathrm{W\,cm^{-2}}$. Early negative delay spectrum has been subtracted from the map to enhance the time dependent signal. (b) Normalized energy integrated in the region 1.25 eV to 1.55 eV (green box in Fig.(a)) are displayed as dots, standard error obtained from 2 measurements is reported as shaded area; best fit, following eq. (5.1) is reported as solid line. (c) Experimental data subtracted by the fit in a specific time range (grey box in (b)) displayed as green dots. Solid line indicates the best fit of a sinusoidal as described in text.

on this time range as well. The most interesting part is the high kinetic energy region, marked as a green box in Fig. 5.10 (a), where we observe very pronounced oscillations in the electron yield. Fig 5.10 (b) shows the normalized energy-integrated signal in this region, from 1.25 eV to 1.55 eV. Part of the oscillations are also visible for lower energies, but we choose this energy interval for higher contrast. By looking at the integrated signal, a decay of around 100 fs is observed, which is strongly modulated up to 120 fs. The slow decay has been fitted using Eq. (5.1) retrieving a time constant of (166 ± 33) fs. In Fig 5.10 (c) we calculated the difference between the experimental data and the best fit, in a time interval which goes from 25 fs to 80 fs to enhance the oscillatory component. This time region has been selected to increase the contrast of the oscillatory signal, although from Fig. 5.10 we can observe the oscillation period is increasing after 100 fs. Therefore, we performed a best fit of sinusoidal signal expressed by Eq. $Ae^{-t/\tau}\sin(2\pi\nu(t)t + \phi_0) + c$ with time-dependent frequency $\nu(t) = \nu_0 + bt$. The amplitude of the signal is damped in time by the exponential factor $e^{-t/\tau}$. If we limit our analysis to the time range from 25 fs to 80 fs the FFT and the sinusoidal fit gives a fundamental period of $1/\nu_0 = (24 \pm 1)$ fs. This period corresponds the umbrella mode in CH_3, suggesting that the observed coherence can be assigned to vibrational modes. Additionally, it is the same order of magnitude

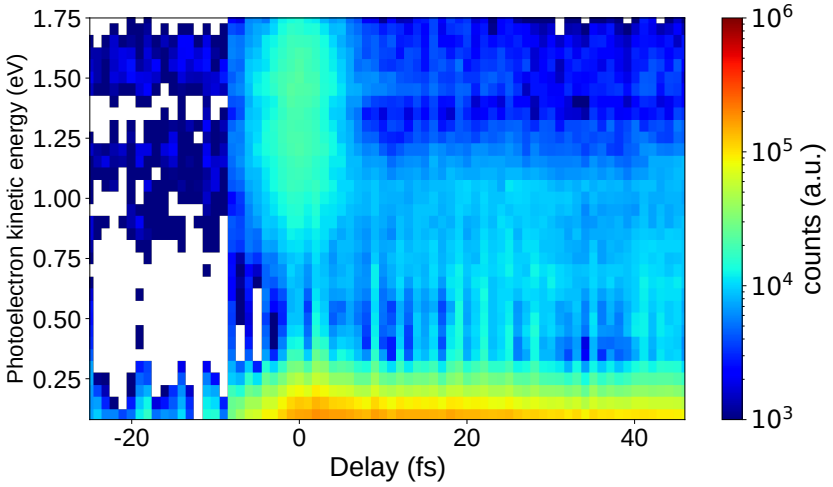

Figure 5.11: Finer scan performed with 1 fs step. Angularly integrated photoelectron energy distribution as a function of the pump-probe delay. Early negative delay spectrum has been subtracted from the map to enhance the time dependent signal. NIR intensity was $9.1 \times 10^{11}\,\mathrm{W\,cm^{-2}}$.

as the difference in energy between several Rydberg states (~ 0.1 eV). When including a chirp in the frequency and extending the range up to 130 fs, we obtain a larger error on the fundamental $1/\nu_0 = (21 \pm 3)$ fs. We also obtain a chirp parameter $b = (-0.018 \pm 0.040)\,\mathrm{THz\,fs^{-1}}$, which increase the period up to 35 fs at the end of the range.

The presence of this modulation in this energy region suggests that the pump excites a coherent superposition of either vibrational state of a single electronic state, or alternatively a superposition of different Rydberg states. Certainly, to address this issue simulation needs to be performed to assign the excitation step in a more quantitative fashion. Here, what we can speculate is that the oscillations are observed only in a specific time windows from 25 fs to 80 fs, after which the period gets longer and then fades. Nuclear vibrational wavepackets possess normally much longer coherence time. Relatively short decoherence time, less than 100 fs could indicate that the oscillatory behavior could be originated from an electronic wavepacket.

Scans with a step of 1 fs was performed in a time range of 40 fs. The angularly integrated photoelectron distribution as a function of the delay is represented in Fig. 5.11. The finer step reveals a much more interesting structure in the energy region from 0.3 eV to 1.1 eV. The slow modulation previously observed for higher energies (5.6.1) appears also in this intermediate energy range. In addition, faster oscillations modulate the signal.

In Fig. 5.12 (a) we reported the energy integrated photoelectron signal in the three regions defined earlier (Fig. 5.9) centred at 0.15,

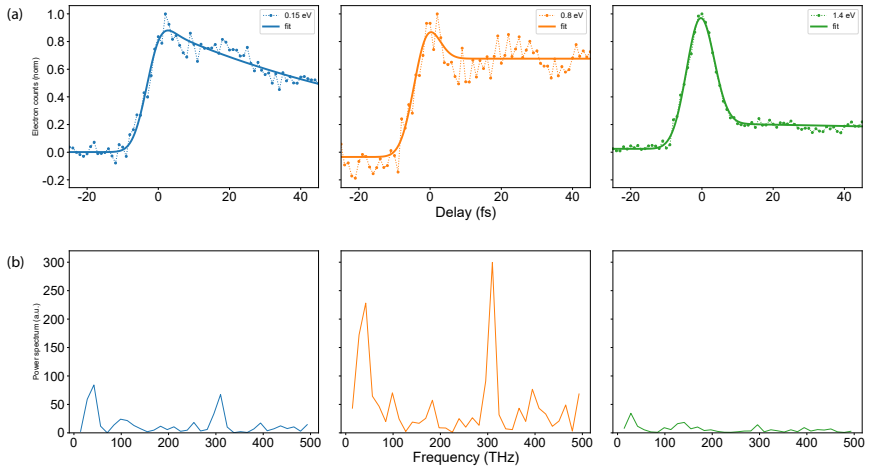

Figure 5.12: *(a)*: energy integrated signal for a fine scan performed with 1 fs step. The three region corresponds to the energy interval centred at 0.15, 0.8 and 1.4 eV specified in Fig. 5.8. Best fit is shown as solid line. *(b)*: Fourier spectrum of the signal in the three regions, with the low frequency components removed. For the intermediate region, a strong fast 310 THz component is observed in top of the slow 40 THz described previously. Higher energy components are flat, but a glimpse of the fast modulations is observed also in the low-kinetic energy region.

0.8 and 1.4 eV, with a width of 0.3 eV. On top of the main curves we have observed previously, we can now resolve faster modulations. In particular, the low kinetic energies electrons show a modulated decay, while the intermediate region presents even higher contrast once it reaches its constant value after the overlap. The higher kinetic energy region, instead, presents less contrast than the previous scan.

We retrieved the best fit from each energy region using Eq. (5.1) in order to remove the slow components of the signal. In particular, the low kinetic energy region is fitted with a decay constant to $\tau_0 = 75$ fs, while the intermediate and high energy regions with no decay. The difference in respect the estimation for the decay can be attributed to short time range explored (almost half in respect, for instance, Fig 5.9). With the use of the best fit curves, we calculate the difference in between the experimental data and the fit, in order to calculate the Fourier transforms of the curves, which are reported in Fig. 5.12 (b). From the Fourier spectrum, we can distinguish two components, at low and high frequencies, specifically for the low and intermediate kinetic energy regions. For the third region, instead, only a very small peak, slightly above the noise level is distinguished below 100 THz, which corresponds to the 24 fs discussed previously. In the first two panels, the low frequencies peaks at 39 THz corresponds to a period of 24 fs, which was observed in the previous scan, but in a region of higher kinetic energies. In the intermediate energy region, an

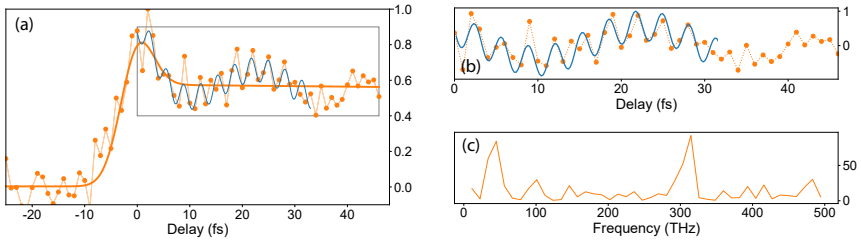

Figure 5.13: Finer scan performed with 1 fs step. (a) Normalized energy integrated in the region 0.25 eV to 1.1 eV are displayed as dots. Solid line indicates the best fit for the slow components, following eq. (5.1). (b) Experimental data subtracted by the fit in a specific time range (grey box in (a)) displayed as green dots. Solid line indicates the best fit of two sinusoidal functions with period 25.5 fs and 3.2 fs. (c) Discrete Fourier transforms of the experimental curve. Two components at 39.9 THz and 310 THz are visible, which corresponds to the 2 periods in (b), respectively.

additional peak appears at higher frequency at 310 THz. It is also visible in the low energy electrons, with less amplitude However, it is completely absent in the higher kinetic energy region. The latter is also the region with the lower signal to noise level, ruling out the possibility that this modulation can be induced by a fast source of noise in the experimental setup.

From Fig 5.11 we notice that this fast modulation is observed for a much broader energy region. The signal obtained by integrated from 0.3 eV to 1.1 eV is reported in Fig. 5.13(a)as orange dots, together with the best fit for the rising components as a solid line. The difference between the experimental data and the fitted envelope is reported in Fig. 5.13 (b). Two sinusoidal functions with frequency 39.9 THz and 310 THz are also reported as guide to the eye up to 32 fs. After this value the contrast of the fast modulation starts to decrease. The Fourier transform of the difference is instead reported in Fig.5.13 (c), showing the same frequency peaks discussed previously. This fast modulation corresponds to a period of 3.2 fs, which is not possible to assign to any vibrational mode. A frequency of 310 THz corresponds in energy to a $\Delta E = 1.28$ eV, which does not correspond to any photon energy of the light source, and it is larger than the typical energy difference in between different Rydberg states in this region. Indeed, theoretical calculation is needed to address the different state involved in these dynamics. At the moment, one can speculate that several Rydberg states with high n number are coherently populated by the UV pump. Due to the presence of the $\pi\pi^*$ valence state, this coherence is carried over an energy region spanning around 1 eV. This is possible because of the presence of the conical intersection in between the valence and the Rydberg states (See. 5.2) and due to the very steep potential of the $\pi\pi^*$ at Franck-Condon region. Without the theory we cannot provide

a specific assignment, but one could justify it that that very intricate state configuration in this region could make a few states interfere, even states which are energetically far, since the coupling in between the different states is mediated by the presence of the many conical intersections.

5.7 COVARIANCE MAPPING

Despite the simplicity of the fragmentation pathways offered by acetone and observed in 5.5, it is still fairly complex addressing the specific excited state dynamics which leads to the parent or the acetyl fragments, in particular when the dynamics is occurring in the Rydberg states. As a matter of fact, an integrated measurement such mass spectroscopy includes all possible production channel for a specific fragment. At the same time, energy resolved measurements, such as photoelectron spectroscopy carries information regarding the initial state of the emitted electrons into its kinetic energy, but at the same time provide no indication towards the fragmentation path. Here, we will show that the combination of the two techniques in the covariance mapping (3.2.1.3) allows us to overcome the intrinsic limitation of both techniques, gaining more insights into the specific dynamics observed.

The acquisition of single shot and simultaneous mass spectra and VMI images let us perform statistical analysis on each dataset. Following the introduction Sec. 3.2.1.3 each dataset $\mathbf{X}(\tau) = \{X_n(\tau)\}$ and $\mathbf{Y}(\tau) = \{Y_n(\tau)\}$ composed of $n = 180 \times 10^3$ shots have been acquired by varying the time delay, with the same experimental condition reported in sec. 5.6.1. In this case X_n represents the n-th single shot acquisition of a mass spectrum, while Y_n indicates the two dimensional velocity map images. In order to reduce the amount of false covariance, laser fluctuations have been acquired through the signal amplitude of a photodiode installed before the beamline. This allows to remove false covariance introduced by the fluctuation of the laser source, by subtracting a partial covariance matrix which contains this information. By binning the TOF signal in the two regions of interest, relative mass 58 for the parent and mass 43 for the acetyl fragment, it is possible to compute 2D VMI image through the covariance in respect each mass bin and the different coordinate of the 2D VMI images. This value can be interpreted as the statistical correlation in between ion in the TOF, and electron in a specific pixel of the VMI image. Essentially, one can produce two different sets of VMI-covariance image, distinguishing the electrons contribution for each mass. Angularly integrating these images will produce 1D photoelectron energy distribution for each mass, which can then be used to compute 2D maps as a function of the time delay in between the two pulses.

The result of the covariance analysis is reported in Fig 5.14. In panel (a) we show the covariance maps of the photoelectron energy

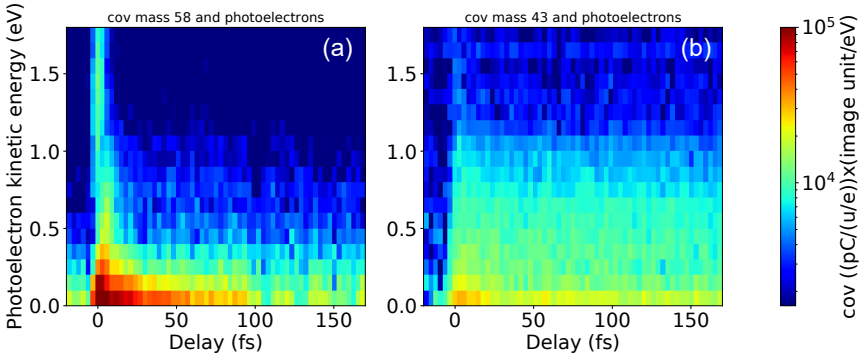

Figure 5.14: Results of the partial covariance analysis in between the yield of the two fragments and the one dimensional photoelectron spectra as a function of the time delay. (a) map shows the energy of the photoelectrons which correlates with the acetyl fragments, while (b) shows the same for the parent. covariance signal below 10^{-2} of the maximum is not shown.

associated with the parent ion. In panel (b), instead, we observe the photoelectron energies in covariance with the acetyl fragment. We note already that the two maps combined cover the entire kinetic energies observed previously, in particular Fig. 5.10(a) which corresponds to the same acquisition but not analyzed in covariance. We observe a significant difference in between the 2 maps and therefore the contribution correlated to the two ions. The parent correlates mostly with electrons with low kinetic energies and also a contribution for the high kinetic energies before 10 fs. However, Acetyl correlates mostly with the intermediate energy electrons. Additionally, the low kinetic energies show a much faster decay time of around 50 fs, while the acetyl electrons signal lasts much longer, remaining almost constant up to 150 fs. Through the covariance analysis, we can therefore assign the three energy regions (0.3, 0.8, 1.4 eV) experimentally defined before to the two ion products. Low kinetic energies (0.3 eV) and high kinetic energies (1.4 eV) correlates mostly to the parent, while the intermediate region at 0.8 eV represents mostly the acetyl fragment.

Considering the excitation scheme suggested previously, the parent ion signal decays faster because perhaps of the evolution in the Rydberg manifold throughout different conical intersection with the $\pi\pi^*$ state. Here, we demonstrate also that this signal correlates with low kinetic energy electrons, suggesting that the excess energy to reach this cationic state is low (< 0.5 eV) or, in other words, that the probe state is as far as possible from the ionization potential. This is also confirmed by the IR scaling for the parent (see 5.5(ions)). At the same time, the yield of photoelectron for intermediate energy around 0.8 eV remains constant in the time range explored. In turn, this indicates that acetyl fragments correlate with higher energies than the parent, which means states which are closer to the ionization potential or,

alternatively higher cationic states. One additional information we can obtained from the covariance analysis is that all the oscillations are related to the acetyl fragment, since they mostly occur in energy region in between from 0.4 eV to 1.2 eV.

6

TIME-RESOLVED UV-INDUCED MOLECULAR DYNAMICS PROBED BY PHOTOELECTRON CIRCULAR DICHROISM

The experiment contained in this chapter aims at demonstrating the possibility of using broadband ultrafast UV pulses to control specific properties of a molecule on an ultrafast time scale. In the following, we exploit the large bandwidth of few-fs UV pulses to populate a coherent superposition of Rydberg states in methyl-lactate, a chiral molecule. The aim is to observe a modulation of the chiral response of the molecule. To address the chiral character of the evolution, circularly polarized pulses can be used to probe the dynamics with a technique which is called Photoelectron circular dichroism (PECD).

The experiment was conceived by Vincent Wanie from my group together with the Harmodyn group from the Centre Laser Intense and Applications (Bordeaux, France) led by Valerie Blanchet and Yann Mariesse. I participated to all three experimental campaigns starting in 2019 and help in the data analysis, as well as discussing possible interpretation.

6.1 INTRODUCTION AND PREVIOUS WORK

Towards the goal of controlling the reactivity of a molecule with very short laser pulses, one can think about many different modifications the target can undergo to favor one or another reaction. For instance, coherent control targets specific molecular states by shaping the pulse spectrum to favor geometrical changes or dissociation. There is also additional interaction in between molecules which one might want to control, one of which is a property called *chirality*.

Generally, an object is called chiral when its mirror images are not superimposable to each other. For instance, typical familiar chiral objects are our hands: the mirror image of one hand is not overlapping with itself. The word chiral comes from the Greek $\chi\epsilon\iota\rho$ (cheir) which means hand. In chemistry, a molecule is chiral if it cannot be superposed on its mirror image by any combination of rotations, translations, and conformational changes. Each chiral molecule exists in two stereoisomers which are mirror images of each other which are called enantiomers. They can be distinguished in between "left-handed" or (-) and "right handed" or (+), which is the reason why chirality is also referred as handedness.

Two enantiomers have precisely the same structural properties, but their chemical properties changes significantly when they interact

with other chiral compounds. In pharmacology the difference in chiral interaction can produce even dangerous outcome: while a specific enantiomer can be employed as a curing drug, the opposite is perceived as a toxin by our body biological chiral receptor. This is the case, for example, for L-Methamphetamine, which is contained in vapor inhalers and R-methamphetamine which is a psychotic drug. Chiral recognition plays therefore an important role in many biological processes and important precautions are required for the synthesis, separation and characterization of chiral compounds [111].

A typical object in physics which is chiral is circularly polarized light (CPL), in which the helicity of photons defines its handedness. Characterization of enantiomers can therefore be performed by studying their interaction with chiral light. Circular dichroism is a common technique where the absorption difference ($\Delta A = A_L - A_R$) in between Left-Handed (LHC) and Right-Handed (RHC) circularly polarized light is measured in a particular target. This method has a wide range of applications in many different fields. Most notably, in the ultraviolet is used to investigate the secondary structure of proteins[112], in particular because of the chiral response of the main amino acids.

In general, since a given enantiomers favor the interaction with CPL with the same handedness, two different samples constitute of pure enantiomers will show dichroism of the same amplitude but opposite in sign. Typical circular dichroism signal is however particularly low, on the order of $10^{-3} - 10^{-5}$ relative to the total absorption signal. The reason is that the circular dichroism signal originates from the product between electric and magnetic dipole interactions, for which the latter is particularly weak. To obtain reasonable signal, circular dichroism requires samples to be highly concentrated, a requirement which is not implementable in gas phase experiments when using ultrashort pulses.

A more suitable techniques to study chirality in the gas phase is Photoelectron circular dichroism (PECD), which was experimentally demonstrated for the first time by Böwering *et al.* in 2001 [113]. Since this phenomenon is purely driven by electric dipole interactions, its magnitude signal can reach higher level than normal circular dichroism.

PECD is based on the fact that electrons that are photoionized from chiral molecules by circularly polarized light are ejected in a preferential emission direction along the propagation axis. In particular, the emission direction depends both on the handedness of the enantiomer and on the helicity of the circularly polarized light. Fig 6.1 explains this behavior, where the direction of emission is reversed when changing the helicity of the ionizing light by keeping the same molecular enantiomer.

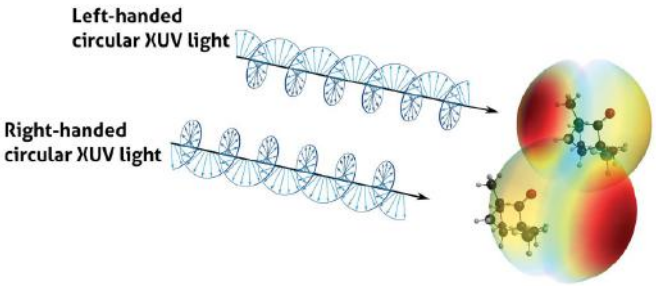

Figure 6.1: Principle of photoelectron angular dichroism. ionization of a chiral molecule by circularly polarized light results in an asymmetry in the forward/backward emission distribution along the propagation axis. Changing the light handedness reverts the distribution. Adapted from [114].

When it was first proposed [115], it was suggested the photoelectron emission from circularly polarized light from a random isotropic sample of chiral molecule would give a distribution which follows

$$I_p(\theta) = \frac{I_{tot}}{4\pi}\left(1 + b_1^p P_1(\cos\theta) + b_2^p P_2(\cos\theta)\right) \tag{6.1}$$

where $p = \pm 1$ indicates the different helicity of the incoming light and θ is the emission angle in respect the laser propagation direction. $P_i(\cos\theta)$ are Legendre polynomials, each one of them with a different coefficient b_i^p. In VMI spectroscopy, each angular distribution is usually decomposed with these functions, due to a symmetry axis which is typically the linear polarization direction which is parallel to the 2D detector. If we used linearly polarized light or an achiral sample, symmetry argument makes the coefficient $b_1^0 = 0$, retrieving the usual VMI case in which only even coefficient describes the angular distribution. However, if circularly polarized light interacts with a chiral target, the forward/backward asymmetry is expressed by a non-zero odd coefficient in Eq. 6.2. In particular, exchanging the enantiomer or the helicity will result in a sign change $b_1^{-1} = -b_1^1$, while preserving the even coefficient $b_2^{-1} = b_2^1$.

A quantitative characterization of the magnitude of the PECD symmetry can therefore be carried out by measuring the difference in intensity of the photoelectron angular distribution produced by LHC and RHC

$$\text{PECD} = \frac{I_{LHC}(\theta) - I_{RHC}(\theta)}{I_{tot}/2} = 2b_1^{+1} \tag{6.2}$$

where the forward/backward asymmetry is expressed as a percentage of the averaged total signal. It can be shown that this definition measures also the difference between the integrated electron counts in the forward and backward hemispheres.

When considering a N-th multiphoton ionization process, the resulting photoelectron angular distribution $D^p(E,\theta)$ is usually described in the three-dimensional space by a series of higher order Legendre polynomials $P_i(\cos\theta)$

$$D^p(E,\theta) = \sum_{i=0}^{2N} \beta_i^p(E)\ P_i(\cos\theta) \tag{6.3}$$

where E is the kinetic energy of the emitted electron, θ is the angle of emission in respect to the propagation direction and N is the number of photons involved in the ionization. β_i^p represents the amplitude of each polynomial, also known as beta-coefficient, and they are kinetic energy dependent.

Following (6.2) a similar definition as the single photon case, the photoelectron spectrum (PES) is defined as the average distribution

$$\mathrm{PES}(E,\theta) = \frac{D^{-1}(E,\theta) + D^1(E,\theta)}{2} \tag{6.4}$$

while the quantity characterizing the forward-backward asymmetry is

$$\mathrm{PECD}(E,\theta) = \frac{D^{-1}(E,\theta) - D^1(E,\theta)}{\mathrm{PES}} \tag{6.5}$$

In this way, it is possible to express the PECD for a multiphoton process

$$\mathrm{MP-PECD} = \frac{1}{b_0}\left(2b_1 - \frac{1}{2}b_3 + \frac{1}{5}b_5 + ...\right) \tag{6.6}$$

where b_0 corresponds to the zero-th order of (6.3) and therefore is the symmetrical part or the averaged yield of the distribution. This definition establishes a unique way of characterizing the asymmetry. [116].

Ever since the first experimental measurements, most of PECD experiments were performed at synchrotron facilities, because of the need for VUV/UV light source which allows single photon ionization and allows exploration in the technique capabilities [113]. For example, it was shown that PECD is sensitive to the ionized molecular orbital and at the same time to the final continuum state [117]. PECD has been used to efficiently identify chemical substitution [118] and molecular conformation [119, 120]. It is able also to distinguish isomers [121] and isomerism [122]. All the above mentioned examples indicate the potential of using PECD for tracking dynamical properties in molecules, but such studies require to use circularly polarized femtosecond pulses, to attain sufficient temporal resolution to follow an ultrafast molecular dynamics through pump-probe PECD measurements. The first

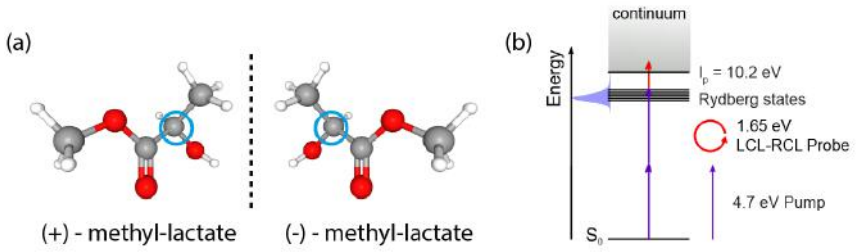

Figure 6.2: *(a)* The two enantiomers of methyl-lactate, in which oxygen atoms are shown in red, carbon atoms in grey and hydrogen in white. Blue circles indicate the chiral center of the molecule. *(b)* Experimental pump-probe scheme: methyl-lactate is excited from the ground state S_0 to a coherent superposition of Rydberg states through the absorption of two linearly polarized UV photon (purple arrows). The subsequent dynamics chiral response is then probe through ionization by circularly polarized NIR pulses (1.65 eV).

demonstration of time-resolved PECD was conducted by Comby *et al.* in fenchone [123]. In this work, an UV-pump (201 nm) initiates a relaxation dynamics which is tracked by the PECD signal, probing the system with a circularly polarized 403 nm pulses. A vibrational (400 fs) and slower electronic 3.28 ps relaxation could be observed. Attosecond resolved chirality has been also demonstrated by the same group, by exploiting self-referenced attosecond photoelectron interferometry in which they measured the difference in photoemission delay in between the forward and backward emission of the electrons [124]. PECD has also been applied successfully to core transition in Free-electron laser [125].

6.2 EXPERIMENT

The main objective was to study the chiral dynamics of methyl-lactate, which is a derivative of lactic acid, a fundamental compound for the metabolism of our muscles. In Fig. 6.2(a) we reported a ball and stick model of the two enantiomers of the molecule.

Fig. 6.2 (b) represents the experimental scheme we employed to investigate the dynamics: basically, few-femtosecond linearly polarized UV pulses are used to excite a coherent superposition of Rydberg states, right below the ionization energy. The PECD signal is then probe by photoionizing with circularly polarized light for the two helicities.

For this experiment, 3 fs UV pulses centered at 266 nm (4.7 eV) are used as a pump. Roughly 70 nJ energy per pulse is focused into the experimental region, to obtain and intensity of around $5 \times 10^{12}\,\mathrm{W\,cm^{-2}}$. The circularly polarized probe is obtained from the HHG arm (see Fig. 3.3) in which a broadband low-dispersion quarter-waveplate is installed after the toroidal mirror. A motorized mount allows the rotation of the waveplate around the propagation direction, and the waveplate angle has been characterized by measuring the ion yield in Krypton in order to obtain the maximum angles corresponding to the two circularly polarized states. A typical spectrum for the probe is reported in Fig. 3.2 and it is associated with 5 fs pulses. An intensity scaling has been performed which confirmed the photoionization scheme, following a similar approach as shown for acetone 5.4. The intensity was kept at $5 \times 10^{12}\,\mathrm{W\,cm^{-2}}$ for most of the acquisition.

Liquid methyl-lactate was heated and evaporated to reach the experimental chamber through a 500 µm needle in the molecular source. Both ions and electrons were recorded during the experiment, but in the following we will focus our discussion only on the electrons. Calibration of the VMI images have been performed by simulating the electrodes configuration with SIMION.

6.3 RESULTS

VMI images have been acquired over 100 000 shots per helicity at the temporal overlap for (+)-methyl-lactate. The other enantiomers have been measured with less statistics. Fig. 6.3 shows the PES and PECD, calculated from the raw VMI images following (6.4) and (6.5) respectively. Each polar plot represents a region of the VMI which goes from 20 meV to 700 meV and the angle θ represents the angle in between the emission and propagation direction. The PES (Fig. (a) and (c)) shows no clear structure and the signal decreases monotonically as a function of the kinetic energy (or momentum) for both enantiomers. This contribution represents the symmetric part of the distribution. When looking at the PECD signal instead, we observe a clear dependance from the emission angle θ. In particular, we observe a clear preference towards 180 deg, where the PECD is positive. When repeating the same measurement with the opposite enantiomer, the asymmetry is reversed - more electron emitted for $\theta = 0$ deg, which confirms that the observed PECD comes from the chiral response of the molecule. It was indeed observed that wrong spectrometer alignment with the respect to the laser focus can induce false asymmetries in the PECD signal: for instance, if the VMI electrodes are not perfectly aligned to the laser focus position, or the jet and the laser are not interacting in the exact center of the VMI. A careful alignment of the instrument with an achiral target (acetone) has been performed, in order to minimize any measured fake asymmetries. The difference in structure between

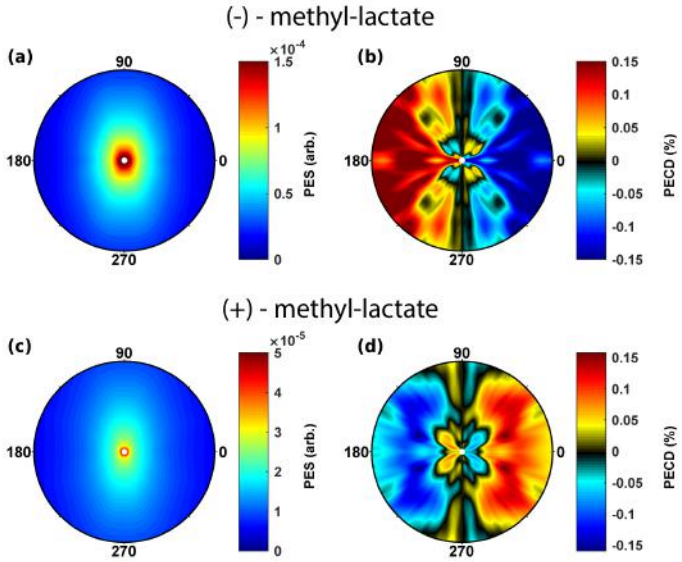

Figure 6.3: PES (a,c) and PECD (b,d) based on the raw VMI images for both the enantiomers (top and bottom). Angle is measured in respect the propagation direction. Radius represents the kinetic energy of the electrons, and the maximum radius shown corresponds to 700 meV. Although the photoelectron distribution is featureless when looking at the PES, the PECD shows a clear preferential direction of emission along the laser propagation. This behavior is reversed when measuring the other enantiomer.

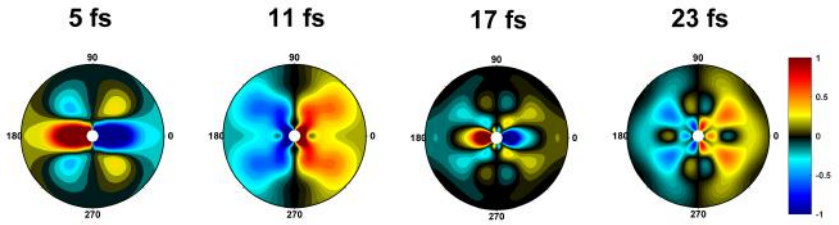

Figure 6.4: Abel inverted two-dimensional PECD images for different pump-probe delays obtained for (-) - methyl-lactate are shown in kinetic energy region from 0.02 eV to 0.3 eV. An ultrafast evolution of the PECD can be observed where the forward/backward emission reverses over around 10 fs.

the two enantiomers in Fig. 6.3 can be attributed to a residual fake asymmetries and different probe condition on different day.

In order to extract more information a p-basex analysis can be performed on the PECD images to extract the beta parameters of the distribution. In a normal VMI configuration, when the projected images on the 2D detector have a specific symmetry axis (i.e., the laser polarization direction), the measured 2D distribution can be decomposed as a sum of Legendre Polynomials through several methods, such as p-basex [56]. Because the even Legendre polynomials are symmetric along the optical axis, the angular distribution of the image is encoded only in the even coefficients of the decomposition. More precisely, for single photon ionization, the angular information is contained in the b_2, also known as anisotropy parameter in VMI spectroscopy, since the b_0 depends only on the radius, representing the integrated kinetic energy distribution. In this sense, the odd Legendre polynomials are related only to the antisymmetric part of the image along the optical propagation axis, which is non-zero only if a forward/backward asymmetry exists, for instance, with PECD. For this reason, even if the typical VMI symmetry argument is not valid, the same decomposition can still be performed when considering the differential image along the optical axis. By applying p-basex analysis on such image, it is still possible to obtain the odd coefficient of the Legendre polynomials, which encodes the asymmetry of the image. To extract the PECD, we need to normalize by the averaged coefficient. To this purpose, it is possible to extract the b_0 from the PES i.e., the symmetric part [123].

In Fig. 6.4 we report an example of applying the Abel inversion through p-basex method to the raw images, such as Fig. 6.3 as a function of the time delay. In the figure, only the energy region from 0.02 eV to 0.3 eV is shown. The figure at $t = 5$ fs, which represents the measurement very close to the time overlap, shows a pronounce asymmetry towards 180 deg, which is reversed in about 10 fs. For

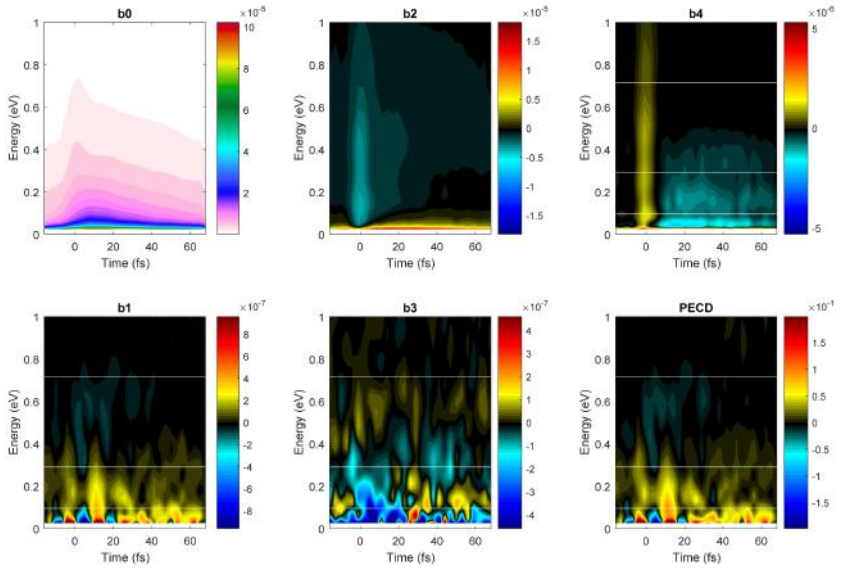

Figure 6.5: Beta coefficients obtained from a p-basex analysis of a series of PECD images for different time delays. The top row contains the symmetric coefficient, in particular b_0 which represents the photoelectron kinetic energy distribution. The bottom row includes the antisymmetric coefficient b_1 and b_3, which are combined to obtain the PECD using (6.6) up to the third order. White horizontal line divides the kinetic energy spectrum in three regions: between 25-100 meV, 100-300 meV and 300-720 meV.

further times, it oscillates with the same period. PECD inversion over such a short time scale has never been observed before.

To extrapolate more quantitative information, a series of PECD images have been recorded for different time delay with a step of 3 fs and p-basex method has been applied to each image. This process has been repeated 5 times over the full time range to acquire statistics. The beta coefficients as a function of the time delay and kinetic energy of the photoelectrons are displayed in Fig. 6.5. In particular, we can distinguish three main kinetic energy regions (separated by white horizontal lines): between (*i*) 25-100 meV, (*ii*) 100-300 meV and (*iii*) 300-720 meV. Higher orders were neglected because most of the dynamics seems to be already included in the first coefficients.

As discussed previously, the b_0 coefficient encodes information regarding the symmetric photoelectron energy distribution. From this perspective, the PES follows well the images shown 6.3 (a,c) as it is composed of a featureless decaying spectrum. It has a maximum at around 5 fs, after which it decays with a time constant of around 60 fs. The even coefficients represent the angular distribution in respect the top-bottom symmetry of the image, which includes a sharp feature around the time origin, which is negative for b_2 and positive for b_4.

The subsequent dynamics, in particular in the low kinetic energy region (*i*), reflects the decay of the PES.

Instead, the odd coefficients b_1 and b_3 represent the asymmetric distribution. They both show clear oscillations around the zero in the low-kinetic energy region, especially in the b_1 coefficient. In the energy region (*ii*) these oscillations are still observed but without sign inversion. They oscillate around a positive value. Both coefficients can be combined following Eq. (6.6) up to the third order to obtain a measure of the asymmetry expressed by

$$\mathrm{PECD}(E) = \frac{2b_1 - 0.5b_3}{b_0} \tag{6.7}$$

This quantity represents the main observable of our experiment, since it includes both the asymmetric components, and it is normalized by the total electron distribution. We observe that the PECD is mainly contained in the b_1 coefficient, since the two maps looks quite similar. This is expected, since the higher order in the decomposition account for the behavior far from the origin (higher kinetic energy), where the PES goes rapidly to zero.

The PECD signal is averaged in the three energy region defined in the previous 2D-maps, and the results are shown in Fig. 6.6 (three left panels). The low kinetic energy region shows very clearly that the PECD is reversed in about 10 fs with an amplitude on the order of 10 %. This signature vanishes at higher kinetic energies (central and bottom panel), but the oscillatory behavior is preserved, with an amplitude on the same order of magnitude. Fourier analysis for each kinetic energy region is also performed, as it is reported in the right panels of Fig. 6.6 for each energy region. Similar peaks centered at a frequency of around 330 meV is observed in all the signal. We note that these oscillations are not observed in the even coefficients (see Fig. 6.5. The reason is that these observables are based on the integrated photoelectron yield, which provide a limited signal to noise ratio.

It is well-known that PECD is sensitive to the electronic and nuclear degrees of freedom of the molecule [126]. In particular, in previous work different vibrational levels can show opposite asymmetries [127]. The oscillatory behavior might suggest that, upon broadband UV excitation, two different states with opposite chiral responses might be interfering, resulting in a modulation of the chiral response of the molecule. The fact that we observe such oscillations on a very short time scale, might indicate that the observed beating is produced by electronic states. For instance, due to the high density of states in the Rydberg manifold, the frequency of the oscillations might match the energy separation of some of these states.

To verify this hypothesis and identify the origin of this modulation we compared our results with advanced theoretical modeling as described in the following.

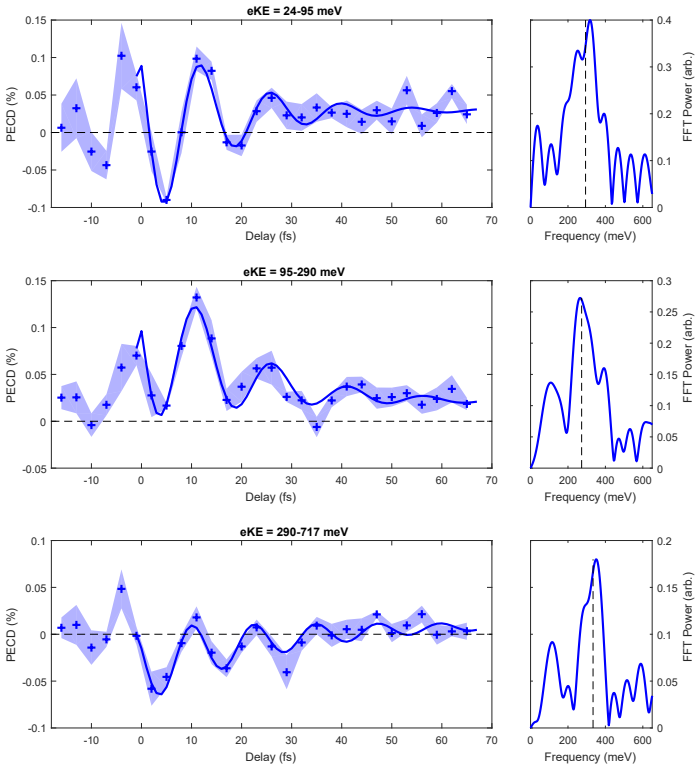

Figure 6.6: Energy resolved PECD. Blue cross markers show the experimental temporal evolution of the PECD signal for $(-)$ - methyl-lactate in the energy region 25-100 meV, 100-300 meV and 300-720 meV (top to bottom panel). Shaded areas show the standard deviation over 5 measurements per point. Blue solid line in each point is intended as guide to the eye. Right panels show the Fourier spectrum of the oscillatory part of each energy region. In all the regions a frequency of 330 meV is observed (dash line), which corresponds to 13 fs period.

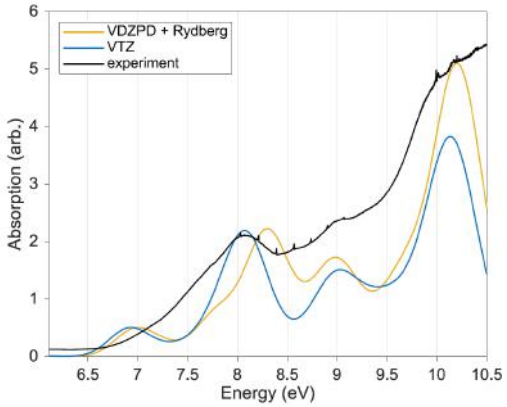

Figure 6.7: Single photon absorption spectrum of methyl-lactate in the energy region where we expect 2 UV excitation. Black curve indicates experimental spectra, measured at Synchrotron (SOLEIL), while blue and yellow light indicates the calculated DFT spectra.

6.4 THEORY AND INTERPRETATION

For the identification of the particular dynamics observed in the experiment, we modelled both the excitation step and the ionization probing.

6.4.1 *Excitation*

In order to calculate the two-photon excitation step, a detailed knowledge of the electronic states of methyl-lactate in the energy region of the UV pump, for which the effective photon energy is centered around 9.3 eV. Being very close to the ionization potential, this region contains several Rydberg states, and its calculation is not trivial.

In Fig. 6.7 the black curve represents the 1-photon absorption spectrum of methyl-lactate in between 6 eV to 10.3 eV, which was measured at the SOLEIL Synchrotron (DESIRS beamline). The curves show two clear peaks at 8.0 and 10.2 eV, with in between a less visible at 9.0 eV. This curve serves as a benchmark for the choice of the particular bases required to describe the target molecule. Considering the ionization potential of methyl-lactate of 10.5 eV, the region of interest around the 2UV pump carrier is supposed to have a high density of delocalized Rydberg states, which requires a properly choice of the basis sets in order to reproduce the experimental curve.

Our collaborators at LCPQ (Toulouse, France), M.C. Heitz and N. Ben Amor tested through Density Functional Theory many different basis sets: the best result was obtained with Valence Triple Zeta (VTZ) basis, which is displayed by the blue curve in Fig. 6.7. In this case, the oscillator strength of the states was shifted by 50 meV and convoluted with a Gaussian with $\sigma = 200$ meV.

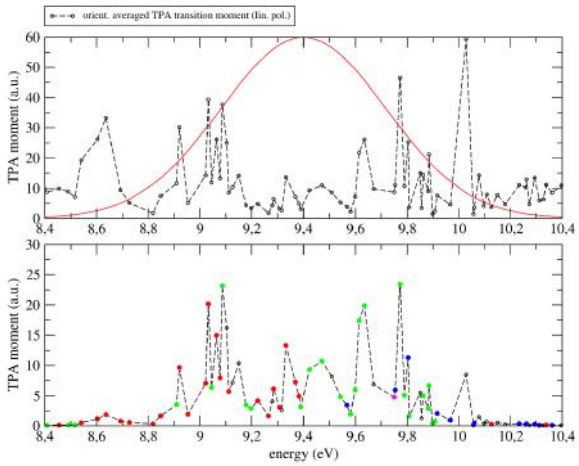

Figure 6.8: Top panel: Calculated two-photon transition moments amplitude in the energy region close the ionization potential. Bottom panel: weighted transition moment probability, considering the spectrum of 2 UV photons, laser polarization and randomly oriented molecules. The red dots indicate the Rydberg states which are originated from the (HOMO), while the green dots are the states coming from the (HOMO-1).

This particular choice of basis is able to match all main feature of the experimental absorption spectrum, but it has the disadvantage of a very high computational costs, which is too high when using the basis to calculate the transition moments. Therefore, we introduced a modified VDZ basis set, which is shown in yellow in the same figure. It corresponds to a VDZDP (valence double zeta + diffuse + polarization) basis combined with a double Rydberg $2s2p2d$ basis localized at the cation charge center. A f function with exponent 0.012 at the same charge center was included.

Time dependent density functional theory (TDDFT) is used to calculate the two-photon absorption transition moments of the specific states. Although the analysis is not complete and the number of Rydberg states needs to be refined, we can discuss preliminary results obtained only a subset of Rydberg states. In Fig. 6.8 top panel we have reported the calculated two-photon absorption transition moments of the considered electronic states, where the solid Gaussian line indicates the excitation coming from the pump. We can already observe that many states are present in this energy region, confirming that the measured chiral response is dependent on a superposition of different Rydberg states. The 2-UV photons spectrum is used to weight the different contribution, resulting in the updated transition moments spectrum reported in the bottom panel. In this figure, for instance, the dot color represents the origin of the specific states: red dots indicate that 8 Rydberg states come through excitation from the Highest Occupied Molecular Orbital (HOMO). I Instead, green dots indicate those

states which come from the (HOMO -1) state. The different character of the two set of Rydberg states indicate that the pump creates two distinct electronic wavepackets, which after ionization will lead to orthogonal continua and therefore cannot interfere.

When applying TDDFT to evaluate the subsequent evolution of each wavepackets, in the case of the states of (HOMO-1) character, we find that the molecular geometry associated with this state is far from the neutral. In other words, the potential energy surfaces of this channel involve strong gradients, which is usually associated with fast decoherence and therefore would not allow us to resolve oscillation in the experiment. With this argument, we focus our attention on the (HOMO) wavepacket only. Despite the fact that at least 8 states are excited by the UV pump, the experiment shows a clear well define oscillation frequency, which indicates that only a few states are responsible for the chiral response of the molecule.

6.4.2 *Classical trajectories simulations*

To narrow down even further the different states involved, classical trajectory simulations have been performed using the Newton-X package. This calculation can give an indication of the different nuclear dynamics induced by the UV, when evaluating the behavior of the molecule. These simulations include nuclear adiabatic evolution of the ground state of the cation, through the projection of the vibrational state of the neutral ground state (GS) on the cationic state and also classical propagation without surface hopping. The propensity rule $\delta\nu = 0$ indicates that this is a good estimation for the dynamics of the Rydberg states.

Fig. 6.9 shows the results of these calculations. In particular, the panel (a) shows the ground state geometry of the neutral, which we will use as a reference to discuss the following dynamics. There are two sets of the trajectories identified in the cation: 43 % reaches a configuration similar to the ground state geometry, while 49 % converge towards a dissociative channel. The two sets of trajectories are displayed in the left and right panels of Fig. 6.9, respectively (Fig. 6.9(b)). (c) panels instead show the evolution of the hole density on the molecule for both sets. In particular, the second set shows that the distance in between the two central carbon of the molecule (CC1 bond) increases significantly after 15 fs. At the same time, this is also reflected in the hole density, where it evolves in about the same time, indicating population transfer in between different orbitals. Change in electronic state populations and nuclear dissociation has already been shown to reduce the coherence in several studies in ionized molecules over only a few femtoseconds range [128] and cannot be explain the extremely long time for which the oscillations are observed experimentally. The other set of trajectories, instead, reaches a geometry

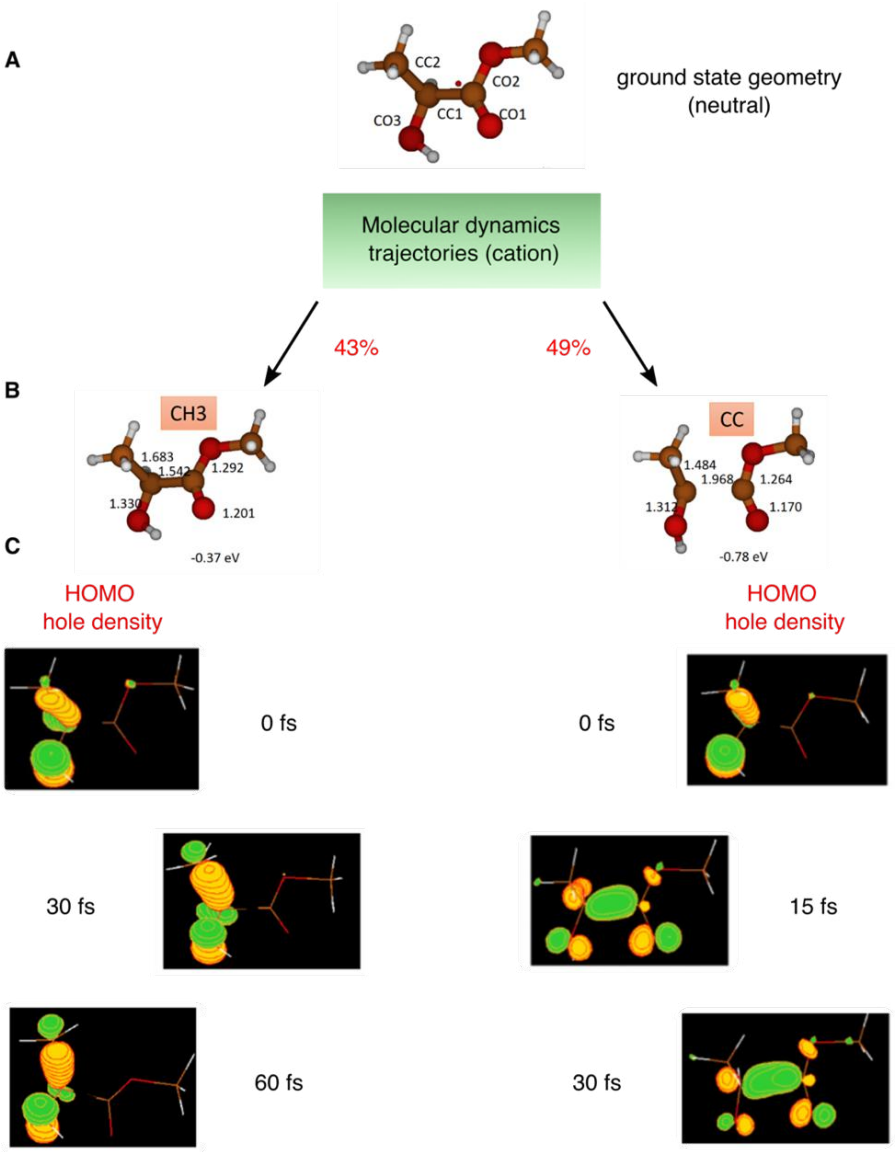

Figure 6.9: Classical trajectory simulations and hole density. (a) calculated ground state geometry of the neutral. (b) Calculated geometries of the two main groups of trajectories associated to the ground state of the cation. Rydberg dynamics should have similar behavior. Isomer 1 (left) preserves the geometry of the neutral ground state, while isomer 2 (right) is subject to strong nuclear distortion, leading to dissociation along the CC bond. The limited nuclear motion favors the preservation of the electronic oscillations, while the dissociation should induce fast decoherence. (c) Temporal evolution of the hole density associated to the HOMO orbital for each isomer: in the first case the density is quite stable over 60 fs, while it evolves very fast for isomer 2.

which is very similar to the ground state nuclear configuration. In this case, the limited motion of the nuclei gives a good contribution to the preservation of the electronic coherences. Additionally, the hole density dynamics shows that there is no substantial change over 60 fs which makes this set of states a good candidate to preserve the coherences.

6.4.3 *Ionization*

When choosing the initial excited wavepacket, it is possible to evaluate the beta coefficients observed experimentally by calculating the ionization differential cross-section for a circularly polarized pulse and estimate the amplitude coefficients of the spherical harmonics which describes the photoelectron angular distribution. For a more detailed description of the model employed, see [129, 130]. Briefly, we can calculate the dipolar ionization dipole moment using

$$d_{\vec{k}}^{(i,j)}(\vec{R}) = \left\langle \Psi_{\vec{k}}^{(j)}(\vec{R}) \; | \vec{e}_{\pm 1} \cdot \vec{r} \; | \; \varphi_i(\vec{R}) \right\rangle \tag{6.8}$$

where $\Psi_{\vec{k}}^{(j)}$ are molecular scattering states for the channel (**energy?**) j with momentum $\vec{k}$, while $\varphi_i(\vec{R})$ a specific time-independent excited Rydberg state, obtained in the previous step. In the previous Eq. $\vec{R}$ represents a molecular orientation and $\vec{e}_{\pm 1}$ indicates the polarization vector of the ionizing circularly polarized light.

The final dipole can be calculated starting from these dipolar matrix elements by including the two-photons transition moments $T_{xx}^{(i)}(\vec{R})$ (where $\vec{x}$ is the polarization axis of the linearly polarized pump) and the time evolution $e^{-iE_i\tau}$ following

$$d_{\vec{k}}^{(j)}\left(\vec{R},\tau\right) = \sum_i S(E_i) T_{xx}^{(i)}(\vec{R}) d_{\vec{k}}^{(i,j)}(\vec{R}) e^{-iE_i\tau} \tag{6.9}$$

where $S(E_i) = I_{pump}(E_i)\sqrt{I_{probe}(E_i)}$. This expression contains all the information regarding which states are excited (product of $I_{pump}T_{xx}^{(i)}$), the time evolution through the phase coefficient and the dipole transition matrix in between the continuum and the initial state. Therefore, one can calculate the ionization differential cross-section

$$\frac{\mathrm{d}\sigma^{(j)}}{\mathrm{d}\Omega_{\vec{k}}}(\tau) = \int \mathrm{d}\vec{R} \frac{\mathrm{d}\sigma^{(j)}\left(\vec{R},\tau\right)}{\mathrm{d}\Omega_{\vec{k}}} = \int \mathrm{d}\vec{R} \left| d_{\vec{k}}^{(j)}\left(\vec{R},\tau\right)\right|^2 \tag{6.10}$$

which can be expressed in terms of real spherical harmonics $Y_{l,i}^{(\cos,\sin)}$

$$\frac{\mathrm{d}\sigma^{(j)}}{\mathrm{d}\Omega_{\vec{k}}}(\tau) = \sum_{l=0}^{6}\sum_{i=0}^{2} b_{l,2i}^{(\cos,\sin)}(\tau) Y_{l,2i}^{(\cos,\sin)}\left(\Omega_{\vec{k}}\right) \tag{6.11}$$

from which obtained the real beta coefficients. Note that the enantio-sensitive coefficients are all the odd-parity coefficients: all the $b_{l,2i}^{(\cos)}$ with odd l and all the $b_{l,2i}^{(\sin)}$ with even l express the chiral response of the molecule. These coefficients can be used to calculate the MP-PECD to be compared directly with the experiment.

In Fig. 6.10 we have reported the calculated MP-PECD for the central energy of the interval define previously: 50, 200 and 500 meV (left panels). First of all, the theory is able to reproduce the oscillatory behavior for all energies, despite the large number (eight) Rydberg states involved in the calculations. Clearly, some of these states are dominating the dynamics and are quite visible in particular in the differential PECD measurement. By looking at the Fourier spectrum of each calculated line, we observe that the experimental frequency of 330 meV is well reproduced only for the high kinetic energy region, while we see the appearance of lower components as the photoelectron kinetic energy diminishes. This supports the more complex structure observed experimentally at the same energies (see Fig. 6.6) and it suggests that closer states interfere more with each other for lower energies. In particular, it could also explain why the overall amplitude of the PECD signal is not well reproduced, a factor of two higher for low kinetic energies. We note that this level of theory does not include any interaction with the nuclei and therefore it is expected to observe no decoherence for long time. Next step is to include more Rydberg states in a similar analysis to narrow down the specific states which are responsible for the beating. Due to the very small separations among these states the assignment of the specific electronic states is not trivial. Additional investigation is being pursued in order to include even more states, in particular Rydberg states which are closer to the ionization energy.

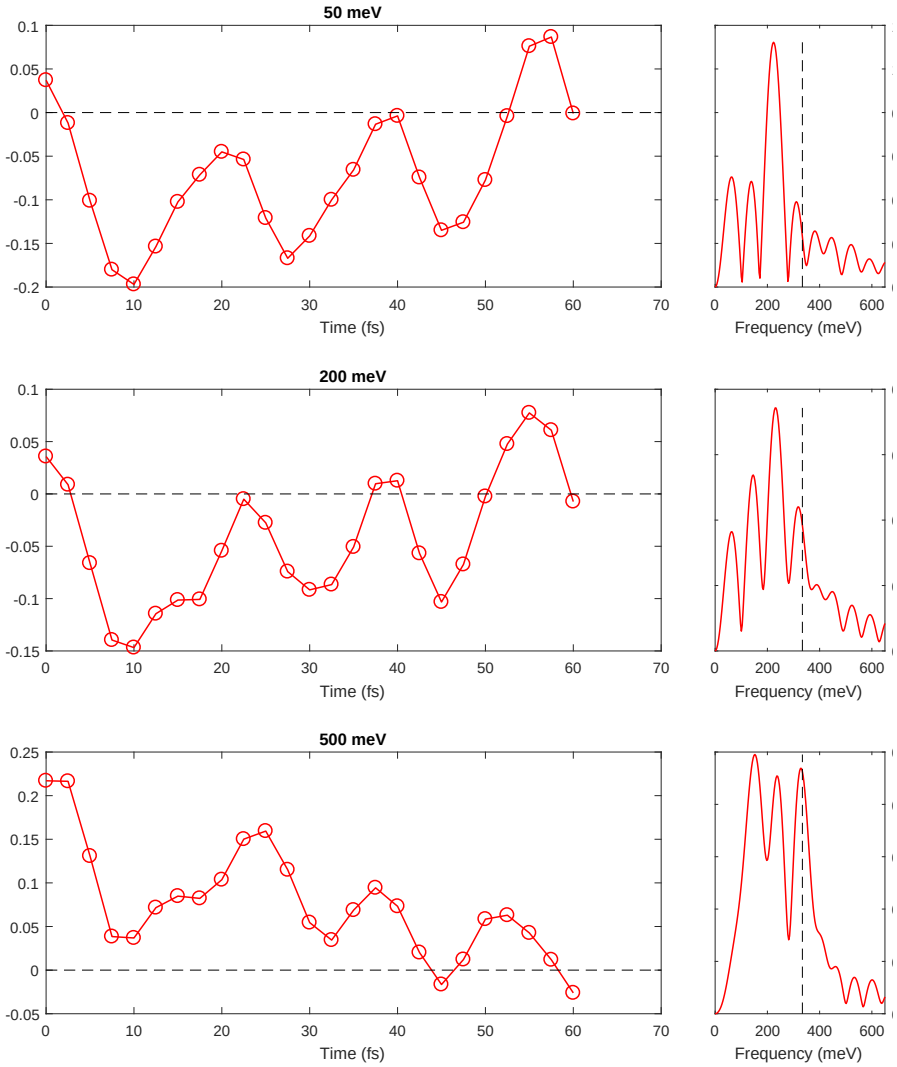

Figure 6.10: Simulated MP-PECD for methyl-lactate, obtained including the two-photon excitation and the ionization from circularly polarized probe for the central energy 50, 200 and 500 meV for every region defined in the experimental map 6.5. The simulations show clear beating in between different electronic states. Right panels show the corresponding Fourier transform. The experimental frequency of 330 meV is well reproduce for the high kinetic energy region, while slightly lower frequency is dominant for lower energies.

7

PHOTOELECTRON ENERGY DISTRIBUTION OF WATER CLUSTERS IONIZED BY AN XUV COMB

The following chapter is dedicated to an experiment performed in October 2019 in collaboration with the group of Ruth Signorell in ETH Zürich, the aim of which was the measurement of the scattering time of the photoelectron in water clusters after ionization in the 10 eV to 30 eV range. Although most of the work described in this thesis focused on UV induced dynamics, the capabilities of the beamline we developed extend also toward higher energy photons and it can be used to study the response of complex target to ionizing radiation. Water clusters represents an interesting starting point for the study of electron dynamics of biomolecules in aqueous solution and the understanding of the water environment alone motivates our investigation.

This chapter will describe the first attempt of such a measurement, focusing in particular on static measurements performed with an XUV comb. It stands as preliminary analysis for the time-resolved investigation of photoemission time delay.

7.1 INTRODUCTION AND PREVIOUS WORK

A deeper understanding of electron scattering in water represents a crucial point in modelling and controlling many processes which occur in different fields ranging from atmospheric chemistry to radiation biology [131, 132].

When a highly energetic charged particle interacts with living tissues or cells, about 80% of the absorbed energy ionizes the medium, whereas the remainder produces electronic and vibrational excitation. This leads to the formation of many intermediate species, such as fragmentation of water molecules and in particular the creation of free (or solvated) electrons with kinetic energies peaked at around 15 eV [133]. Since high energy photons (such as X or γ-rays) typically produce primary fast electrons by Compton scattering, one can say that also highly energetic radiation can indirectly produce secondary electrons with the same energy range around tens of eV. Low-kinetic energy electrons have been shown to play a crucial role in DNA damage since they can ionize further the tissues or interact with the DNA macromolecule resulting in strand-breakage [134, 135]. A scheme of this process is depicted in Fig. 7.1.

Through a bottom-up approach in the understanding of such complex systems, investigating electron scattering and transport properties

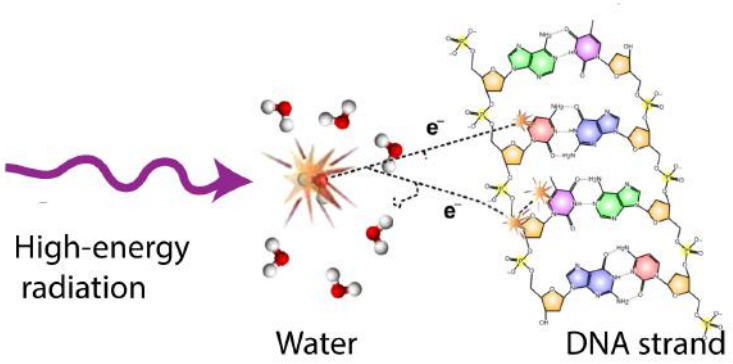

Figure 7.1: When highly energetic particles or photons interacts with water, electrons with energy in between 10 eV to 50 eV are produced. These electrons are known to be responsible for DNA damage.

in water remains fundamental. In synchrotron, attenuation length between 10 eV to 100 eV has been measured [136] and photoelectron angular distribution in liquid water [137] have been measured. In this context, scattering cross sections for liquid water has been retrieved in the sub excitation range [138–140]. For the energy range of low-kinetic energy electrons, amorphous ice was measured through electron scattering [141]. For liquid water, photoelectrons energy distribution has been recently measured by monochromatized high harmonic sources [142]. Instead, electron scattering in large water clusters has been studied as a function of cluster size in [143] and the transport properties have been compared with condensed phase data [144].

Although many of these studies shed light on low kinetic energy electrons scattering in water, mostly estimating scattering cross sections and channel-resolved energy losses, only a few times resolved studies of electrons scattering in water have been reported, in particular in water clusters. It is known that these low energies electrons, when they propagated through biological tissues, induce ultrafast non-thermal reactions, typically in the femtosecond time range. In the 2020, the measurement scattering time of the electron in water, which represents the initial step for this chain of processes, has been reported for the first time [145], pioneering the application of attosecond techniques to such class of targets.

Time-resolved spectroscopy with extremely high temporal resolution can shed new light into the ultrafast electron dynamics occurring in hydrated molecules. In this context, our group investigated already electron transport properties in large dielectric nanoparticles [146], in which an inelastic scattering time of around 400 as was measured for photoelectron energies between 20 eV to 30 eV. This result proved the capability of attosecond spectroscopy to be applied to large dielectric target such as water clusters.

Nevertheless, merging attosecond spectroscopy setups and liquid water samples is still technologically challenging. Attosecond XUV pulses need to propagate in high vacuum and low-dispersion environment, which makes the implementation of cuvettes for liquid target impossible. Liquid micro jet [147] has been extensively used in synchrotron sources, but it has only in the last few years implemented with tabletop sources [145, 148]. As a more manageable target, molecular sources producing water clusters in gas phase might partially simplified the technological limits for the realization of such experiments. At the same time, water clusters stand as an interesting prototype target on its own, with specific properties which put them in between the gas and liquid phase, which could simplify the interpretation of the experimental results and the application of theoretical models.

In this chapter, we report the measurements of photoelectron spectra in water clusters containing around 100 molecules ionized by an attosecond XUV comb in the energy region from 20 eV to 50 eV, based on a publication [149]. In particular, the aim is to extract photoelectron spectra from the water cluster signal from other species which are producing by the cluster source, specifically gas phase water and the carrier gas (helium). This analysis represents the first step for the interpretation of attosecond time-resolved photoelectron spectra, such as RABBITT [150].

7.2 EXPERIMENT

The experiment was performed using the beamline described in 3.1.2. In this case, it was seeded with long pulses, without injecting gas in the fiber and using the typical output of the Ti:sa laser. 2 mJ with a temporal width 20 fs, centered at a carrier wavelength of 780 nm were used to generate the XUV comb through High Harmonic generation (HHG) [151] in the first arm of the beamline. An example of the driving laser spectrum can be observed in grey in Fig. 3.2.

Fig. 7.2 represents a scheme of the first arm. The driving laser was focused in a pulsed gas jet injecting around 200 mbar of argon. The generated XUV beam and the driving field propagated collinearly through a thin Al foil of 100 µm thickness, which stopped the 780 nm. Afterwards, the HHG beam was focused onto the interaction region through a grazing-incidence gold-coated toroidal mirror, where it crossed with the molecular beam. Fig. 7.2 (b) shows the obtained XUV spectrum, measured downstream by the XUV spectrometer described in 3. It consists of a comb of odd harmonics of the fundamental frequency in an energy range between 20 eV to 50 eV, coming from the 13th up to 31st harmonics.

Water clusters were produced by expanding water vapor through a pulsed Even-Lavie (EL) valve [152] (Fig. 7.2(a). 12 bar of helium carrier

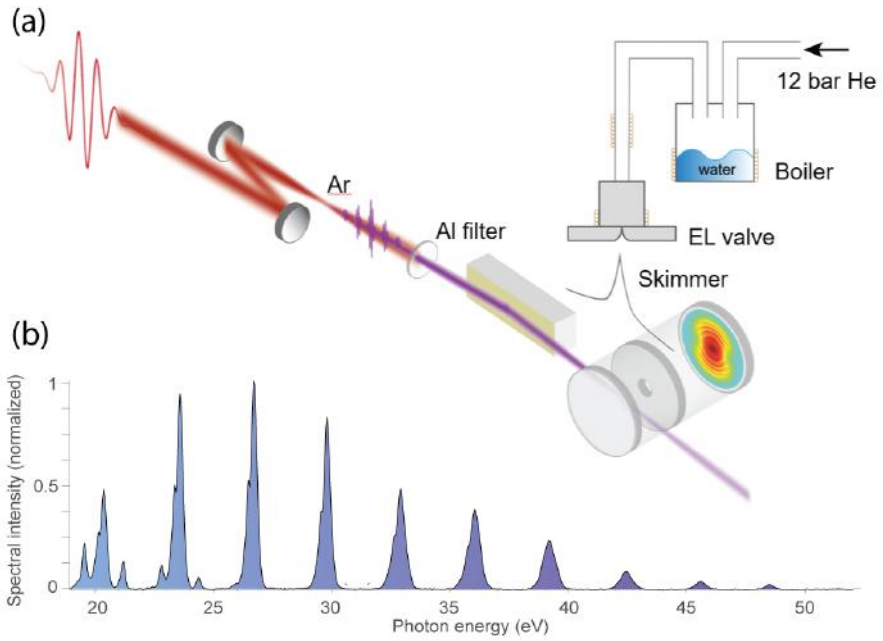

Figure 7.2: *(a)*: A 780 nm, 20 fs driving laser is used to generate an attosecond pulse train through HHG by focusing it on a pulsed jet filled with argon. The XUV pulses are focused into the interaction region by a gold-coated toroidal mirror at grazing incident. Water clusters are produced by expanding water vapor through an Even-Lavie valve into vacuum using helium as a carrier gas. *(b)*: High-harmonic spectrum generated in argon. Satellite peaks below 25 eV are originated from higher order diffraction introduced by the gratings.

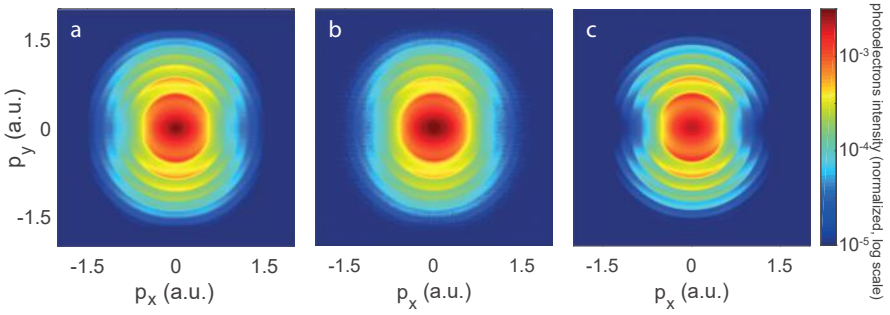

Figure 7.3: 2D projections of the angle-resolved photoelectron momentum distributions, reported in atomic units for clusters (a), He/water vapor mixture (c) pure helium. All the images have been fully symmetrized along both the x and y axes and normalized to the innermost ring and shown on logarithmic scale. The XUV beam is polarized along the y axis.

gas were injected in the sample reservoir filled with liquid water. Thermocouple resistors controlled the temperature of the sample reservoir, which in turns affect the different cluster size distribution. For this experiment, the temperature was set at 383 K. To avoid condensation in the nozzle, the EL valve and the transport tubing is kept heated at higher temperature at 388 K. The result is that a mixture of water vapor, clusters and helium was expanded in the experimental region through a skimmer. The condition described here resulted in a molecular beam with clusters containing about 100 molecules. This was estimated by previous measurements of cluster size distribution performed at ETH Zürich with the same source [153] using Na-doping measurements [154] and it will also be confirmed later in our analysis by a fit in the photoelectron spectrum.

Time of flight mass spectra and VMI images were recorded using the most common VMI design in a perpendicular extraction configuration [54, 155].

7.3 RESULTS AND DISCUSSION

VMI images are obtained for different target mixture and are reported in Fig. 7.3. Each image is acquired integrating 30 000 laser shots and are fully symmetrized along the x and y axes. In the figure, we normalized each image to the innermost ring to enhance their similarity.

Fig. 7.3 (a) represents the photoelectron momentum distribution (PAD) in atomic units obtained when clusters are efficiently produced. The energy distribution shows the typical equidistant rings structure reflecting by ionization by an HHG comb spectrum 7.2 (b). Due to the typical operation of the cluster source, water clusters are not the only species that are present in the experimental region, but also gas

phase water monomers and helium atoms are injected, which will contribute to the overall signal. Indeed, these additional species may represent the dominant contribution to the photoelectron spectrum, acting as a relatively large background in our experiment on water clusters. For this reason, we have developed a robust analysis that allows the removal of such a background and gives us access to the cluster contribution.

This process relies on evaluating the contribution to the PAD Fig. 7.3(a) of these species - helium and water monomers - in order to eliminate it and extract a pure signal assigned to the water clusters. For the evaluation step, we measured photoelectron momentum distributions relatively to the background species only, operating the cluster sources in two additional conditions. For the first, the laser pulse is synchronized to intercept the rising edge of the temporal profile of the cluster beam pulse, for which a lower-density mixture of helium and water monomers is obtained, which contained no clusters. Second, a measurement of pure helium can be performed by not heating the system, reducing the amount of water content to a negligible amount. These alternative conditions were verified by mass spectra measurements as shown in Fig. 7.4. The (a) panel, or the clusters condition, shows a series of equally distanced peaks which represents the different size of clusters detected.

The mass spectra were recorded with the maximum voltage available (4 kV), while in order to detect large clusters a much higher accelerating field needs to be provided, up to 20 kV. For this reason, the largest clusters we detect in this method is $n = 13$, despite the known operation of the source [153]. As it will also verified from the photoelectrons, this is due only to the lack of proper voltage supply and does not indicate the correct cluster distribution present in the molecular beam. For the two other conditions instead (b) and (c), no clusters are detected and therefore can be used to quantify the photoelectron spectra. We note that contaminants are detected in all the three cases as a constant background.

Fig 7.3 (b) and (c) shows the resulting photoelectron distributions for the two additional cases of He/water mixture and helium only, respectively. All the three VMI images in the figure have been normalized to the innermost ring in each image. Before normalization the ratio of signals for this specific ring in (a), (b), (c) respectively is $1 : 0.25 : 0.9$, as expected from the different source conditions. Beside the difference in signal levels, the photoelectron spectra, in particular clusters and water monomers does not show significant differences.

We want to stress that the spectra acquired with the two additional conditions cannot be directly used as background and subtracted from Fig. 7.3 (a). The reason is that the relative concentration of helium and water monomers is not constant for different temporal slices of the molecular beam. Therefore, the three distributions need to be

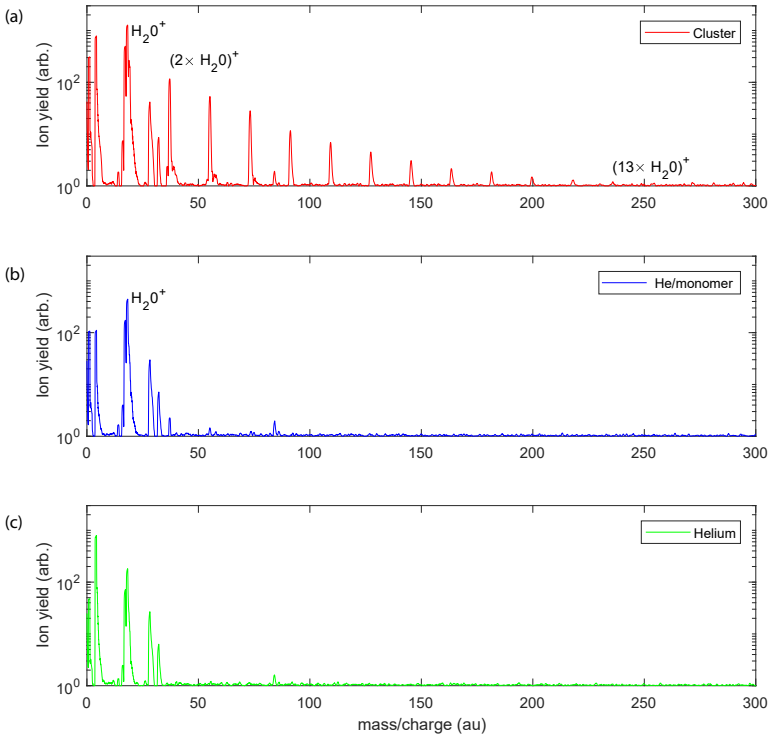

Figure 7.4: Mass spectra acquired for the three different operating conditions of the cluster sources (see text for details): clusters (a), He/water monomer (b) and helium (c). In order to observe large clusters, high voltages (up to 20 kV needs to be applied, while in our case we were limited by the voltage supplier to only 4 kV. For this reason, only clusters up to $n = 13$ are observed. The two other conditions show the absence of clusters.

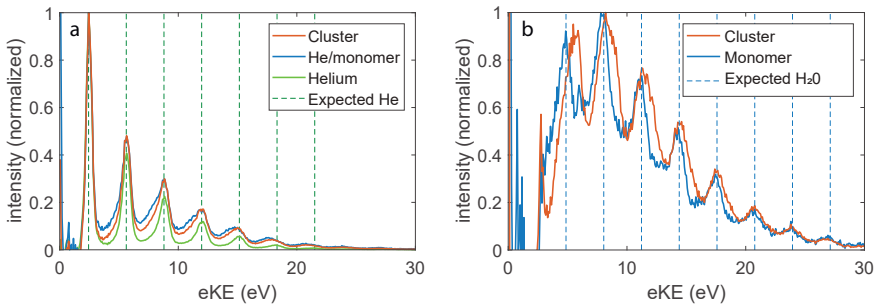

Figure 7.5: *(a)*: Angularly integrated inverted photoelectron spectra for the three conditions: red solid line indicates cluster, while He/-monomer and helium are represented by blue and green, respectively. Spectra are normalized to the lowest energy peak, a background has been removed. Green dashed lines show the energies expected for ionization of helium atoms ($I_P = 24.58\,\text{eV}$). *(b)*: Blue and red curves from (a) after the subtraction of the rescaled helium (green) spectrum; blue dashed lines indicate expected energies for ionization from the HOMO of water monomers ($I_P = 12.62\,\text{eV}$) by the XUV comb.

analyzed separately, with the goal of finding a rescaling factor which allows to make the subtraction. From this moment, we will refer with 'Cluster spectrum' to refer to the first target condition, or in other words the mixture of clusters, water monomer and helium. 'Monomer' will be used to indicate the second condition, as a mixture of helium and gas phase water molecule, while 'helium' will be used for pure helium spectrum.

As a first step, the full three dimensional momentum Newton spheres were retrieved by Abel inversion of the bi-dimensional projected data, shown in Fig. 7.3. The python implementation of a BASEX algorithm, included in the package PyAbel was used to the purpose [55]. Briefly, the 2D projection are decomposed as a sum of Legendre Polynomials to optimize the inversion. Then, the center slices of the reconstructed 3D photoelectron distribution were angularly integrated, resulting in the curves shown in 7.5 (a) as a function of the kinetic energy of the photoelectron (eKE). In the same figure, the photoelectron energies for ionization of helium atoms by the XUV comb ($eKE = h\nu - I_P$, with $I_P = 24.58\,\text{eV}$) are indicated by the green dashed lines.

In each of the three spectra, an exponentially decaying background was observed, which we attributed to scattered electrons generated in the long ionization volume due to the loosely focused XUV pulses. In the figure, this background has been already removed, through the fit with a combination of a Gaussian and an exponential function. The dominant contribution in the photoelectron spectra is attributed to helium, considering that all the spectra, regardless of the source condi-

tion, matches well the expected kinetic energies for helium ionization. This is also confirmed by looking at the mass spectrum, although it is not possible to use this relative abundance because of the difference in collection efficiency for the mass spectra and the electrons, i.e., we collect more electrons than ions.

Even without knowing the relative concentrations of helium in the water conditions, it is still possible to extract a specific ratio from the photoelectron spectra. We can identify a specific peak in the image, which includes almost entirely photoelectrons coming from helium. For the water targets (clusters and monomers) only the higher-binding-energy bands of water contribute to the spectrum for kinetic energies lower than 5 eV, because clusters and monomers have an ionization potential much lower than helium and therefore will show a contribution mostly at higher energies. Therefore, we can assume than that the first peak at 2.5 eV is dominated by photoelectrons coming from helium. Therefore, the ratio between the intensity of this peak in the different spectra represent a measure of the relative abundance of ionized helium in the clusters and He/monomer spectra. It can be then used to rescale the pure helium spectrum and remove it from the clusters and monomer signal. The result of the subtraction is shown in Fig. 7.5 (b).

The dashed blue lines indicate the expected photoelectron energies corresponding to ionization from the highest-occupied molecular orbital (HOMO) of gas phase water ($I_P = 12.62$ eV) by the XUV comb. In this case, the two spectra (solid line) are normalized to the maximum peak. For the spectrum corresponding to He/monomer mixture, the subtraction of the helium is expected to show a clear signature of ionization from gas phase water. In fact, the peaks of the blue curves match well the blue dashed lines. For the clusters spectrum, instead, the newly subtracted signal consists now of the photoelectrons produced by a mixture of clusters and water monomers. This is evident by the fact that they also match very closely the energies expected for water, but they also show an evident shoulder shifted towards higher kinetic energies. This is readily explained by the fact that the ionization potential of the clusters is expected to be 0.8 eV lower than the water monomers [153, 156]. For low kinetic energies (< 5 eV) the subtracted spectra show background subtraction artefacts, which might originate from a combination of imperfect subtraction of the diffuse low-energy features and imperfect rescaling based on the first peak. Nevertheless, for higher energies the difference in the two subtracted spectra demonstrates that a significant quantity of photoelectrons is produced by the water clusters and we are able to resolve it.

7.4 SIMULATIONS

To validate our interpretation, it is possible to compare the experimental results with simulated photoelectron spectra, including the spectrum of the XUV comb. We developed a method in which we compute the photoionization spectrum of helium, water monomers and clusters by each harmonic present in the comb and combine this with known information relative to cross-sections of gas phase water monomers and clusters.

Basically, we can describe the photoelectron distribution in terms of separated spectral components corresponding to each species present in the interaction region and ionized by each harmonic

$$\mathrm{PES}(eKE) = \sum_k I_k \sum_i A_i \sigma_i(k \cdot h\nu) \mathrm{PES}_i^k(k \cdot h\nu - eBE), \tag{7.1}$$

where $h\nu$ is the fundamental photon energy of the driving field and I_k represents the relative intensity of harmonic of order k. The index i indicates the species: helium, water monomers and clusters, and their relative abundance is indicated by the factor A_i. The parameters σ_i represents the energy dependent cross sections of each species, for which we used experimentally measured values found in literature [157, 158]. The corresponding photoelectrons spectra PES_i^k are calculated from the photon energy and the binding energies of the different species.

First of all, we simulated the pure helium photoelectron spectra, by fitting the green solid line in Fig. 7.5(a) in order to extract experimental parameters such as the relative XUV spectral intensities and the intrinsic resolution of the spectrometer. The result can be seen in Fig. 7.6(a). Due to the large ionization volume (Rayleigh length) defined by the loosely focus XUV beam, the trajectories inside the VMI of the electrons produced very far off-center will experience stronger VMI-lensing. This results in a clear asymmetric shape for the helium peaks, with a tail extending toward lower electron kinetic energies.

For this reason, each PES of helium is represented here by an exponentially modified Gaussian function [159] following

$$\begin{aligned}\mathrm{PES}_{He}^k(eKE) = &\frac{w}{\alpha}\sqrt{\frac{\pi}{2}} \exp\left[\frac{1}{2}\left(\frac{w}{\alpha}\right)^2 - \frac{eKE - eKE_0}{\alpha}\right] \times \\ &\left\{1 - \mathrm{erf}\left[\frac{1}{\sqrt{2}}\left(\frac{w}{\alpha} - \frac{eKE - eKE_0}{w}\right)\right]\right\}\end{aligned} \tag{7.2}$$

where w is the peak width and α indicates an asymmetry parameter, which they were both assumed to vary linearly on the kinetic energy. Additionally, eKE_0 represents the center of each distribution and is determined from the photon energy of the $k-$th harmonic and the ionization potential of helium, in order that the center of the peak

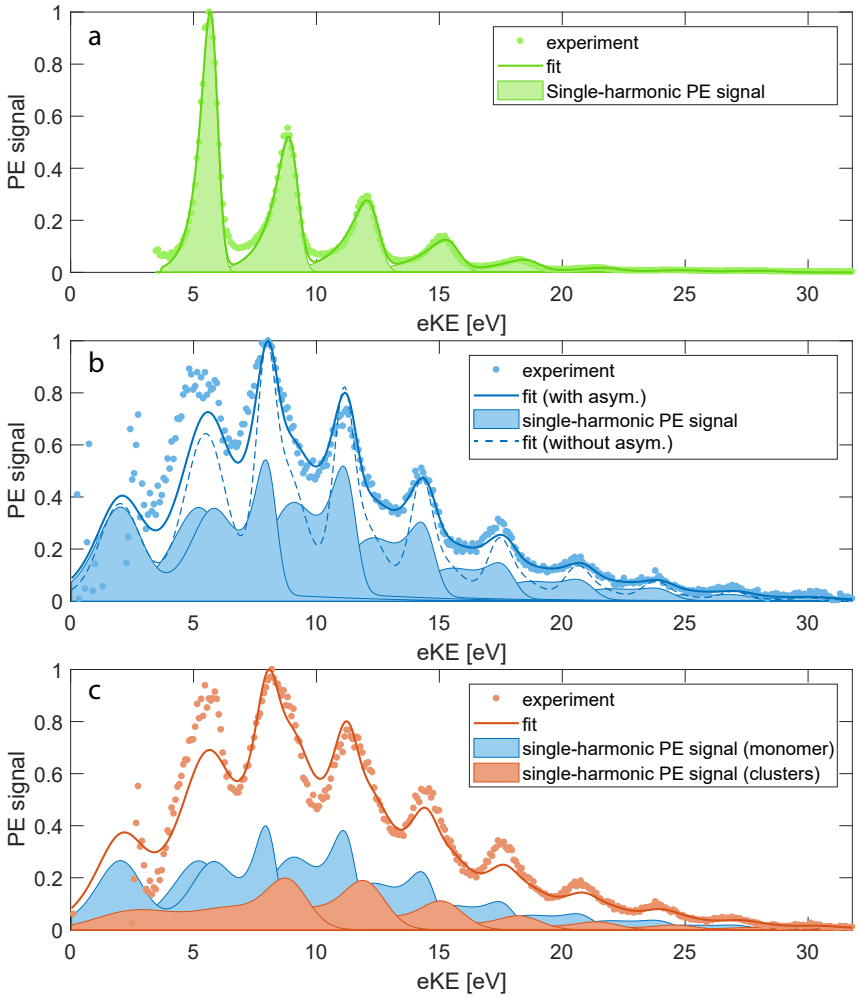

Figure 7.6: Comparison in between experimental spectra and simulations: *(a)* helium spectrum (without baseline) in dots, while solid line indicates the fit of the overall spectrum, assuming a combination of individual ionization spectrum for each harmonic, including harmonic width, amplitude and asymmetric parameters. *(b)* comparison for extracted water monomer only spectrum, solid line fit indicates the final fit, while dashed line shows the result of the fitting procedure without including the asymmetry peak corrections. *(c)* Fitting for clusters/water mixture.

lies at $eKE_0 = k \cdot h\nu - I_P$. In Fig. 7.6(a), each individual components expressed by Eq. (7.2) is shown as shaded area, while the total photoelectron spectrum is represented by a solid line. From this fit, the relative spectral intensity for the XUV peaks agrees with the optical spectrum (Fig. 7.2 (b)). The linewidths range from 0.2 eV to 0.5 eV, full width at half maximum, from 2.5 eV to 20 eV kinetic energy.

In a second step, the isolated water monomer spectrum (blue curve, Fig. 7.5(b)) is fitted, by keeping the retrieved XUV parameters (line widths and asymmetry) constants. The monomer spectrum is described by a sum of 4 Gaussian functions representing photoionization from the $1b_1$, $3a_1$ and $1b_2$ orbitals as found in literature [160]. In our case we replace the Gaussian functions with the exponentially modified Gaussian from (7.2) to take into account the asymmetry observed and the spectrometer linewidth. The solid line of Fig. 7.6(b) shows the spectrum obtained by the sum of each individual harmonic components (shaded areas). For clarity, we also included two different fits, by including or not the asymmetry term. The agreement with the experimental observed water spectrum comes only when the asymmetries are considered, showing that the determination of the experimental condition from the helium spectrum are crucial to the understanding of the more complex targets. This step shows that our model can replicate also the spectrum for water.

Finally, we focused on the clusters spectrum reported in Fig. 7.6(c). The monomer contributions are included in the same way as the previous step, still keeping the line shape parameters constant. Condensation effects are accounted on the cluster photoionization cross section, calculated by linearly scale the monomer cross section with $\sigma_{cl} = n\sigma_{mon}$, with n indicating the cluster size. The photoelectron spectrum for the clusters is represented by a literature spectrum obtained for a cluster of 20 molecules ionized with 22 eV light [160]. The relative band intensities in this spectrum should represents very closely the cluster regime we have investigated. For the clusters, no asymmetry is included due to the broad nature of the photoelectron bands. Additionally, condensation effects are also included as a size-dependent energy shift ΔeBE [153, 156] to have

$$\mathrm{PES}^k_{cl}\left(eKE\right) = \mathrm{PES}^k_{cl}\left(k \cdot h\nu - eBE + \Delta eBE\right) \tag{7.3}$$

This band shift can run in between 0.8 eV to 1.2 eV with respect to the monomer binding energies.

We performed a two parameters fit to the experimental spectrum shown as orange dots in Fig. 7.6(c). The first parameter represents the aforementioned energy shift for the ionization potential, resulting in a retrieved value of 0.8 eV which is consistent with clusters value of 100 water molecules [153]. The second parameter is the relative concentration A_{cl} in Eq. (7.1).The retrieved value for this is expressed as a ratio of photoelectrons originating from monomers to clusters,

which stands as 2:1. These two fit parameters presented are the main outcome of our analysis and demonstrate that a clear signature of water clusters can be extracted from the experimental spectra.

8

CONCLUSIONS

The work described in this thesis aims at exploring ultrafast dynamics on a few-fs time scale in gas-phase molecules initiated by ultrashort ultraviolet pulses. In particular, the use of novel few-fs ultraviolet pulses provide the optimal pump pulse to study photo-induced processes of interest in photo-chemistry on a time scale not explored so far. At the same time, the broad bandwidth of such pulses gives the possibility of triggering a coherent superposition of neutral electronic states, which results in an ultrafast dynamics which is potentially independent of the nuclear degrees of freedom. We will briefly mention here the different outcome of the investigation presented.

To this purpose, 4 fs ultraviolet pulses have been combined with NIR few-cycle 5 fs pulses, which acts as a probe, resulting in a time resolution of only a few femtoseconds. The two pulses have been combined in a double sided spectrometer, which detected simultaneously, and single shot electrons and ions produced by ionizing gas phase molecules. The electrons were measured through a VMI spectrometer, recording the kinetic energy and the angular distribution. The ions were acquired through a high-resolution mass spectrometer. Additionally, an attosecond pulse train or isolated pulse in the XUV can be generated through HHG generation for photoionization study at higher photon energies. These pulses will be combined with the ultrashort UV pulses to attain the best time resolution available.

Different experimental schemes have been described: linear pump and linear probe have been used to investigate the ultrafast photodissociation of methyl-iodide and the Rydberg states dynamics triggered in Acetone. Instead, the combination of linear UV and circular probe have been used to perform photoelectron circular dichroism, a powerful method to investigate the chiral response of methyl-lactate on a very short time scale.

Tracking the dissociation methyl-iodide in the A-band with few-fs pulses

Firstly, the photo-induced cleavage of the C–I bond of methyl-iodide has been investigated upon excitation of 1 UV photon and probe by multiple NIR photons. The ion yield of the three ions (parent, iodine and methyl) has been tracked as a function of the pump-probe delay. The parent ion signal shows the fastest decay of 5.5 fs, while methyl and iodine possess similar decay time around 20 fs. Surprisingly, the iodine signal is observed to increase again after around 30 fs. Due the nature of the multiphoton probing, several ionization channels needed

to be considered for the interpretation of this results. The neutral evolution has been simulated by semi-classical calculations, showing that the revival of the iodine signal can occur only after the conical intersection has been reached, after which part of the population can be accessed more easily through the NIR probe. The extremely high time resolution achieved by the combination of the few-fs pump and probe allows to study this dynamics for the first time in this time range, unveiling a novel behavior in particular in the time range right after the CI, which was previously estimated close to at 14 fs from the FC, but with a pump pulse of 24 fs [79]. The extremely short ionization window for the parent can be accessed only using few-fs UV pulses in combination with very short ionizing probe.

In the future, these measurements could be performed with the additional measurement of the ions kinetic energies to be able to distinguish iodine ions coming from the two main PES curve of methyl-iodide.

Triggering ultrafast Rydberg states dynamics in acetone

The Rydberg state dynamics in Acetone has been studied by exciting a coherent superposition of Rydberg states using 2 UV photons and probing with a single NIR photon. By looking at the mass spectra, the parent ion gives a very fast decay ($\sim$ 50 fs), while the acetyl fragment reaches a constant value as soon as the two pulses overlap. The parent signal can be interpreted by the presence of many crossing in between the Rydberg states and relatively repulsive valence state 4^1A_1 ($\pi\pi^*$) along the C–O length coordinate. This configuration results in a very narrow time window which gives the intact parent after ionization, based on previously published work [107] coupled with the ground state of the cation [105], while an almost constant yield for the acetyl, due the highly dissociative cationic curves. The photoelectrons kinetic energies show very rich features: three energy regions can be distinguished with very different time decays. Among these, the intermediate region (at 0.8 eV) yield is modulated by two main frequencies corresponding to 24 fs and 3.2 fs. The first one matches the characteristic umbrella mode of methyl, while the second is too fast to be assigned to any vibrational dynamics. Although theoretical support is in development, one can speculate that this fast modulation can be assigned to coherences induced by the UV pump, favored by the high density of states in the Rydberg. Alternatively, it could be assigned also to the wavepacket travelling in between the different curves which allows for several crossings. Theory is anyway needed to address this topic. Experimentally, we showed also that combining the mass spectra and kinetic energies map in the covariance mapping provides many more information: in particular, we demonstrated the intermediate

kinetic energy region correlates mostly with the acetyl fragment, while the parent is limited to the low kinetic energy electrons.

Ultrafast chiral response in the Rydberg

Electronic coherences have been studied in detail through the chiral response of methyl-lactate, after excitation in the Rydberg states of a chiral molecule, methyl-lactate. In this experiment, 2 UV photons creates the coherent wavepacket, whose chirality is probed through ionization by a circularly polarized NIR photon, measuring the backward/forward asymmetry in the electron emission (PECD). PECD stands as high-sensitivity alternative due to the differential measurements of photoelectron angular distribution. In fact, the observed PECD signal appears oscillating with a period of 13 fs and lasting for around $\sim$ 60 fs. Modulation of the chiral response on such a short time scale has never been observed before. The use of advanced theoretical model, which simulated the full experiment, allows to assign the oscillation to the beating of electronic Rydberg states, and the effect of decoherences on the modulation. This experiment represents the first example of chemical control with few-fs UV pulses, intended as modulation of the chiral response of the molecule.

Photoionization of large water clusters by an XUV comb

On a different experiment, a XUV comb generated through HHG has been used to study water clusters, as a preliminary step to measure the photoionization time delay in such targets. Due to the operation of the cluster source, in the experimental chamber there is an unknown mixture of water clusters, water monomers and buffer gas (helium), with a prevalence of the latter. By operating the source in different condition, a fully experimental protocol has been developed to remove and isolate the different contribution. The procedure relies on the ionization potential required by each target, which allows to retrieve concentration ratios which can be used to rescale and remove independent measurements of the contribution for the buffer gas and water monomers. We validate our method by simulating the experimental spectra and independently characterized the cluster source. This method stands as preliminary step towards attosecond measurement of time delay of photoemission in large clusters, with long term goal of embedding molecule in the clusters to simulated aqueous environment.

In conclusions, the work described here represents the first experiments in which a few-fs ultraviolet pulses have been used to trigger different photo-induced processes in neutral molecules and shows their value in extending attosecond technology towards neutral

molecules. The experiment in Methyl-iodide have shown their applicability towards well-investigated target with increased time resolution, in particular showing pump-free dynamics in the very first 40 fs. In Acetone, we showed that the excitation of a Rydberg wavepacket is connected to a very fast dynamics (around 30 fs) in the Rydberg manifold and is able to trigger at the same time vibrational and perhaps electronic beatings. However, to have a clearer indication of such wavepacket evolution, differential measurements need to be used: exploiting the high sensitivity of PECD is crucial for the observation of purely electronic beatings in the Rydberg, which have the surprising effect of modulating the chiral response of Methyl-lactate. The extremely short duration of the excitation pulses is crucial to avoid decoherence induced by the nuclear degrees of freedom.

From this perspective, these results encourage the use of short ultraviolet pulses for the investigation of such dynamics, which, paired with refined techniques such as PECD or covariance mapping aid at the understanding of such complex dynamics in the neutral, but above all stands as an effective tool to control them.

BIBLIOGRAPHY

[1] Arnaldo Donoso and Craig C. Martens. „Simulation of Coherent Nonadiabatic Dynamics Using Classical Trajectories.“ In: *The Journal of Physical Chemistry A* 102.23 (June 1998), pp. 4291–4300. ISSN: 1089-5639, 1520-5215. DOI: 10.1021/jp980219o.

[2] Theodore H. Maiman. „Stimulated Optical Radiation in Ruby.“ In: (1960).

[3] Ahmed H. Zewail. „Femtochemistry: Atomic-Scale Dynamics of the Chemical Bond.“ In: *The Journal of Physical Chemistry A* 104.24 (June 2000), pp. 5660–5694. ISSN: 1089-5639, 1520-5215. DOI: 10.1021/jp001460h.

[4] N. F. Scherer, J. L. Knee, D. D. Smith, and A. H. Zewail. „Femtosecond Photofragment Spectroscopy: The Reaction ICN → CN + I.“ In: *The Journal of Physical Chemistry* 89.24 (Nov. 1985), pp. 5141–5143. ISSN: 0022-3654. DOI: 10.1021/j100270a001.

[5] Ahmed H. Zewail. „Femtochemistry. Past, Present, and Future.“ In: *Pure and Applied Chemistry* 72.12 (Jan. 2000), pp. 2219–2231. ISSN: 1365-3075, 0033-4545. DOI: 10.1351/pac200072122219.

[6] Moshe Shapiro and Paul Brumer. „Coherent Control of Molecular Dynamics.“ In: *Reports on Progress in Physics* 66.6 (May 2003), pp. 859–942. ISSN: 0034-4885. DOI: 10.1088/0034-4885/66/6/201.

[7] David J. Tannor and Stuart A. Rice. „Control of Selectivity of Chemical Reaction via Control of Wave Packet Evolution.“ In: *The Journal of Chemical Physics* 83.10 (Nov. 1985), pp. 5013–5018. ISSN: 0021-9606. DOI: 10.1063/1.449767.

[8] P. M. Paul, E. S. Toma, P. Breger, G. Mullot, F. Augé, Ph. Balcou, H. G. Muller, and P. Agostini. „Observation of a Train of Attosecond Pulses from High Harmonic Generation.“ In: *Science* 292.5522 (June 2001), pp. 1689–1692. DOI: 10.1126/science.1059413.

[9] M. Hentschel, R. Kienberger, Ch Spielmann, G. A. Reider, N. Milosevic, T. Brabec, P. Corkum, U. Heinzmann, M. Drescher, and F. Krausz. „Attosecond Metrology.“ In: *Nature* 414.6863 (Nov. 2001), pp. 509–513. ISSN: 1476-4687. DOI: 10.1038/35107000.

[10] M. Drescher, M. Hentschel, R. Kienberger, M. Uiberacker, V. Yakovlev, A. Scrinzi, Th Westerwalbesloh, U. Kleineberg, U. Heinzmann, and F. Krausz. „Time-Resolved Atomic Inner-Shell Spectroscopy.“ In: *Nature* 419.6909 (Oct. 2002), pp. 803–807. ISSN: 1476-4687. DOI: 10.1038/nature01143.

[11] Eleftherios Goulielmakis et al. „Real-Time Observation of Valence Electron Motion." In: *Nature* 466.7307 (Aug. 2010), pp. 739–743. ISSN: 1476-4687. DOI: 10.1038/nature09212.

[12] J. Mauritsson et al. „Attosecond Electron Spectroscopy Using a Novel Interferometric Pump-Probe Technique." In: *Physical Review Letters* 105.5 (July 2010), p. 053001. DOI: 10.1103/PhysRevLett.105.053001.

[13] M. Schultze et al. „Delay in Photoemission." In: *Science* 328.5986 (June 2010), pp. 1658–1662. DOI: 10.1126/science.1189401.

[14] K. Klünder et al. „Probing Single-Photon Ionization on the Attosecond Time Scale." In: *Physical Review Letters* 106.14 (Apr. 2011), p. 143002. DOI: 10.1103/PhysRevLett.106.143002.

[15] G. Sansone et al. „Electron Localization Following Attosecond Molecular Photoionization." In: *Nature* 465.7299 (June 2010), pp. 763–766. ISSN: 1476-4687. DOI: 10.1038/nature09084.

[16] F. Kelkensberg et al. „Attosecond Control in Photoionization of Hydrogen Molecules." In: *Physical Review Letters* 107.4 (July 2011), p. 043002. DOI: 10.1103/PhysRevLett.107.043002.

[17] J. Breidbach and L. S. Cederbaum. „Migration of Holes: Formalism, Mechanisms, and Illustrative Applications." In: *The Journal of Chemical Physics* 118.9 (Mar. 2003), pp. 3983–3996. ISSN: 0021-9606. DOI: 10.1063/1.1540618.

[18] F. Remacle and R. D. Levine. „An Electronic Time Scale in Chemistry." In: *Proceedings of the National Academy of Sciences* 103.18 (May 2006), pp. 6793–6798. ISSN: 0027-8424, 1091-6490. DOI: 10.1073/pnas.0601855103.

[19] F. Remacle, R. D. Levine, E. W. Schlag, and R. Weinkauf. „Electronic Control of Site Selective Reactivity: A Model Combining Charge Migration and Dissociation." In: *The Journal of Physical Chemistry A* 103.49 (Dec. 1999), pp. 10149–10158. ISSN: 1089-5639. DOI: 10.1021/jp991853k.

[20] R. Weinkauf, P. Schanen, D. Yang, S. Soukara, and E. W. Schlag. „Elementary Processes in Peptides: Electron Mobility and Dissociation in Peptide Cations in the Gas Phase." In: *The Journal of Physical Chemistry* 99.28 (July 1995), pp. 11255–11265. ISSN: 0022-3654, 1541-5740. DOI: 10.1021/j100028a029.

[21] L. S. Cederbaum and J. Zobeley. „Ultrafast Charge Migration by Electron Correlation." In: *Chemical Physics Letters* 307.3 (July 1999), pp. 205–210. ISSN: 0009-2614. DOI: 10.1016/S0009-2614(99)00508-4.

[22] F. Calegari et al. „Ultrafast Electron Dynamics in Phenylalanine Initiated by Attosecond Pulses." In: *Science* 346.6207 (Oct. 2014), pp. 336–339. DOI: 10.1126/science.1254061.

[23] M. Born and R. Oppenheimer. „Zur Quantentheorie Der Molekeln.“ In: *Annalen der Physik* 389.20 (1927), pp. 457–484. ISSN: 1521-3889. DOI: 10.1002/andp.19273892002.

[24] B. H. Muskatel, F. Remacle, and R. D. Levine. „The Post-Born–Oppenheimer Regime: Dynamics of Electronic Motion in Molecules by Attosecond Few-Cycle Spectroscopy.“ In: *Physica Scripta* 80.4 (Oct. 2009), p. 048101. ISSN: 1402-4896. DOI: 10.1088/0031-8949/80/04/048101.

[25] Wolfgang Domcke and David R. Yarkony. „Role of Conical Intersections in Molecular Spectroscopy and Photoinduced Chemical Dynamics.“ In: *Annual Review of Physical Chemistry* 63.1 (2012), pp. 325–352. DOI: 10.1146/annurev-physchem-032210-103522.

[26] Chris T. Middleton, Kimberly de La Harpe, Charlene Su, Yu Kay Law, Carlos E. Crespo-Hernández, and Bern Kohler. „DNA Excited-State Dynamics: From Single Bases to the Double Helix.“ In: *Annual Review of Physical Chemistry* 60.1 (May 2009), pp. 217–239. ISSN: 0066-426X, 1545-1593. DOI: 10.1146/annurev.physchem.59.032607.093719.

[27] Rajeshwar P. Sinha and Donat-P. Häder. „UV-induced DNA Damage and Repair: A Review.“ In: *Photochemical & Photobiological Sciences* 1.4 (Apr. 2002), pp. 225–236. ISSN: 1474-9092. DOI: 10.1039/B201230H.

[28] Carlos E. Crespo-Hernández, Boiko Cohen, Patrick M. Hare, and Bern Kohler. „Ultrafast Excited-State Dynamics in Nucleic Acids.“ In: *Chemical Reviews* 104.4 (Apr. 2004), pp. 1977–2020. ISSN: 0009-2665, 1520-6890. DOI: 10.1021/cr0206770.

[29] M. N. R. Ashfold, B. Cronin, A. L. Devine, R. N. Dixon, and M. G. D. Nix. „The Role of $\Pi\sigma^*$ Excited States in the Photodissociation of Heteroaromatic Molecules.“ In: *Science* 312.5780 (June 2006), pp. 1637–1640. DOI: 10.1126/science.1125436.

[30] Vincent Wanie, Lorenzo Colaizzi, Andrea Cartella, Andrea Trabattoni, and Francesca Calegari. „Advances of Ultraviolet Light Sources: Towards Femtosecond Pulses in the Few-Cycle Regime.“ In: *Emerging Laser Technologies for High-Power and Ultrafast Science*. 2053-2563. IOP Publishing, 2021, 5–1 to 5–26. ISBN: 978-0-7503-2536-3. DOI: 10.1088/978-0-7503-2536-3ch5.

[31] Mara Galli et al. „Generation of Deep Ultraviolet Sub-2-Fs Pulses.“ In: *Optics Letters* 44.6 (Mar. 2019), p. 1308. ISSN: 0146-9592, 1539-4794. DOI: 10.1364/OL.44.001308.

[32] Alessio Valentini. „Selective Bond Formation Triggered by Short Optical Pulses: Quantum Dynamics of a Four-Center Ring Closure.“ In: (2020), p. 12.

[33] V. Engel, V. Staemmler, R. L. Vander Wal, F. F. Crim, R. J. Sension, B. Hudson, P. Andresen, S. Hennig, K. Weide, and R. Schinke. „Photodissociation of Water in the First Absorption Band: A Prototype for Dissociation on a Repulsive Potential Energy Surface." In: *The Journal of Physical Chemistry* 96.8 (Apr. 1992), pp. 3201–3213. ISSN: 0022-3654, 1541-5740. DOI: 10.1021/j100187a007.

[34] T Koopmans. „Über die Zuordnung von Wellenfunktionen und Eigenwerten zu den Einzelnen Elektronen Eines Atoms." In: *Physica* 1.1 (Jan. 1934), pp. 104–113. ISSN: 0031-8914. DOI: 10.1016/S0031-8914(34)90011-2.

[35] Albert Stolow, Arthur E. Bragg, and Daniel M. Neumark. „Femtosecond Time-Resolved Photoelectron Spectroscopy." In: *Chemical Reviews* 104.4 (Apr. 2004), pp. 1719–1758. ISSN: 0009-2665, 1520-6890. DOI: 10.1021/cr020683w.

[36] L. Xu, Ch Spielmann, A. Poppe, T. Brabec, F. Krausz, and T. W. Hänsch. „Route to Phase Control of Ultrashort Light Pulses." In: *Optics Letters* 21.24 (Dec. 1996), pp. 2008–2010. ISSN: 1539-4794. DOI: 10.1364/OL.21.002008.

[37] M. Nisoli, G. Sansone, S. Stagira, S. De Silvestri, C. Vozzi, M. Pascolini, L. Poletto, P. Villoresi, and G. Tondello. „Effects of Carrier-Envelope Phase Differences of Few-Optical-Cycle Light Pulses in Single-Shot High-Order-Harmonic Spectra." In: *Physical Review Letters* 91.21 (Nov. 2003), p. 213905. DOI: 10.1103/PhysRevLett.91.213905.

[38] H.R. Telle, G. Steinmeyer, A.E. Dunlop, J. Stenger, D.H. Sutter, and U. Keller. „Carrier-Envelope Offset Phase Control: A Novel Concept for Absolute Optical Frequency Measurement and Ultrashort Pulse Generation." In: *Applied Physics B* 69.4 (Oct. 1999), pp. 327–332. ISSN: 1432-0649. DOI: 10.1007/s003400050813.

[39] Donna Strickland and Gerard Mourou. „Compression of Amplified Chirped Optical Pulses." In: *Optics Communications* 56.3 (Dec. 1985), pp. 219–221. ISSN: 0030-4018. DOI: 10.1016/0030-4018(85)90120-8.

[40] M. Nisoli, S. De Silvestri, O. Svelto, R. Szipöcs, K. Ferencz, Ch. Spielmann, S. Sartania, and F. Krausz. „Compression of High-Energy Laser Pulses below 5 Fs." In: *Optics Letters* 22.8 (Apr. 1997), p. 522. ISSN: 0146-9592, 1539-4794. DOI: 10.1364/OL.22.000522.

[41] Robert Szipöcs, Kárpát Ferencz, Christian Spielmann, and Ferenc Krausz. „Chirped Multilayer Coatings for Broadband Dispersion Control in Femtosecond Lasers." In: *Optics Letters* 19.3 (Feb. 1994), pp. 201–203. ISSN: 1539-4794. DOI: 10.1364/OL.19.000201.

[42] E. A. J. Marcatili and R. A. Schmeltzer. „Hollow Metallic and Dielectric Waveguides for Long Distance Optical Transmission and Lasers.“ In: *Bell System Technical Journal* 43.4 (July 1964), pp. 1783–1809. ISSN: 00058580. DOI: 10.1002/j.1538-7305.1964.tb04108.x.

[43] Tamas Nagy, Michael Forster, and Peter Simon. „Flexible Hollow Fiber for Pulse Compressors.“ In: *Applied Optics* 47.18 (June 2008), p. 3264. ISSN: 0003-6935, 1539-4522. DOI: 10.1364/AO.47.003264.

[44] D.J. Kane and R. Trebino. „Characterization of Arbitrary Femtosecond Pulses Using Frequency-Resolved Optical Gating.“ In: *IEEE Journal of Quantum Electronics* 29.2 (Feb. 1993), pp. 571–579. ISSN: 1558-1713. DOI: 10.1109/3.199311.

[45] W. Seka, S.D. Jacobs, J.E. Rizzo, R. Boni, and R.S. Craxton. „Demonstration of High Efficiency Third Harmonic Conversion of High Power Nd-glass Laser Radiation.“ In: *Optics Communications* 34.3 (Sept. 1980), pp. 469–473. ISSN: 00304018. DOI: 10.1016/0030-4018(80)90419-8.

[46] J. Ringling, G. Korn, J. Squier, O. Kittelmann, and F. Noack. „Tunable Femtosecond Pulses in the near Vacuum Ultraviolet Generated by Frequency Conversion of Amplified Ti:Sapphire Laser Pulses.“ In: *Optics Letters* 18.23 (Dec. 1993), p. 2035. ISSN: 0146-9592, 1539-4794. DOI: 10.1364/OL.18.002035.

[47] P. Baum, S. Lochbrunner, and E. Riedle. „Generation of Tunable 7-Fs Ultraviolet Pulses: Achromatic Phase Matching and Chirp Management.“ In: *Applied Physics B* 79.8 (Dec. 2004), pp. 1027–1032. ISSN: 0946-2171, 1432-0649. DOI: 10.1007/s00340-004-1668-2.

[48] Rocio Borrego Varillas, Alessia Candeo, Daniele Viola, Marco Garavelli, Sandro De Silvestri, Giulio Cerullo, and Cristian Manzoni. „Microjoule-Level, Tunable Sub-10 Fs UV Pulses by Broadband Sum-Frequency Generation.“ In: *Optics Letters* 39.13 (July 2014), p. 3849. ISSN: 0146-9592, 1539-4794. DOI: 10.1364/OL.39.003849.

[49] Takao Fuji, Takuya Horio, and Toshinori Suzuki. „Generation of 12 Fs Deep-Ultraviolet Pulses by Four-Wave Mixing through Filamentation in Neon Gas.“ In: *Optics Letters* 32.17 (Sept. 2007), p. 2481. ISSN: 0146-9592, 1539-4794. DOI: 10.1364/OL.32.002481.

[50] Charles G. Durfee, Sterling Backus, Henry C. Kapteyn, and Margaret M. Murnane. „Intense 8-Fs Pulse Generation in the Deep Ultraviolet.“ In: *Optics Letters* 24.10 (May 1999), p. 697. ISSN: 0146-9592, 1539-4794. DOI: 10.1364/OL.24.000697.

[51] John C. Travers, Teodora F. Grigorova, Christian Brahms, and Federico Belli. „High-Energy Pulse Self-Compression and Ultraviolet Generation through Soliton Dynamics in Hollow Capillary Fibres." In: *Nature Photonics* 13.8 (Aug. 2019), pp. 547–554. ISSN: 1749-4885, 1749-4893. DOI: 10.1038/s41566-019-0416-4.

[52] Tatsuo Harada, Kaoru Takahashi, Hideo Sakuma, and Andrzej Osyczka. „Optimum Design of a Grazing-Incidence Flat-Field Spectrograph with a Spherical Varied-Line-Space Grating." In: *Applied Optics* 38.13 (May 1999), p. 2743. ISSN: 0003-6935, 1539-4522. DOI: 10.1364/AO.38.002743.

[53] Luca Poletto. „Grazing-Incidence Flat-Field Spectrometer for High-Order Harmonic Diagnostics." In: *Optical Engineering* 40.2 (Feb. 2001), p. 178. ISSN: 0091-3286. DOI: 10.1117/1.1339204.

[54] André T. J. B. Eppink and David H. Parker. „Velocity Map Imaging of Ions and Electrons Using Electrostatic Lenses: Application in Photoelectron and Photofragment Ion Imaging of Molecular Oxygen." In: *Review of Scientific Instruments* 68.9 (Sept. 1997), pp. 3477–3484. ISSN: 0034-6748, 1089-7623. DOI: 10.1063/1.1148310.

[55] Vladimir Dribinski, Alexei Ossadtchi, Vladimir A. Mandelshtam, and Hanna Reisler. „Reconstruction of Abel-transformable Images: The Gaussian Basis-Set Expansion Abel Transform Method." In: *Review of Scientific Instruments* 73.7 (July 2002), pp. 2634–2642. ISSN: 0034-6748. DOI: 10.1063/1.1482156.

[56] Gustavo A. Garcia, Laurent Nahon, and Ivan Powis. „Two-Dimensional Charged Particle Image Inversion Using a Polar Basis Function Expansion." In: *Review of Scientific Instruments* 75.11 (Nov. 2004), pp. 4989–4996. ISSN: 0034-6748. DOI: 10.1063/1.1807578.

[57] Stephen Gibson, Daniel D. Hickstein, Roman Yurchak, Mikhail Ryazanov, Dhrubajyoti Das, and Gilbert Shih. *PyAbel/PyAbel: Vo.8.4*. Zenodo. Apr. 2021. DOI: 10.5281/zenodo.4690660.

[58] Erik P. Månsson, Stacey L. Sorensen, Cord L. Arnold, David Kroon, Diego Guénot, Thomas Fordell, Franck Lépine, Per Johnsson, Anne L'Huillier, and Mathieu Gisselbrecht. „Multi-Purpose Two- and Three-Dimensional Momentum Imaging of Charged Particles for Attosecond Experiments at 1 kHz Repetition Rate." In: *Review of Scientific Instruments* 85.12 (Dec. 2014), p. 123304. ISSN: 0034-6748. DOI: 10.1063/1.4904372.

[59] F. Chandezon, B. Huber, and C. Ristori. „A New-regime Wiley–McLaren Time-of-flight Mass Spectrometer." In: *Review of Scientific Instruments* 65.11 (Nov. 1994), pp. 3344–3353. ISSN: 0034-6748. DOI: 10.1063/1.1144571.

[60] S. Scherer, K. Altwegg, H. Balsiger, J. Fischer, A. Jäckel, A. Korth, M. Mildner, D. Piazza, H. Reme, and P. Wurz. „A Novel Principle for an Ion Mirror Design in Time-of-Flight Mass Spectrometry." In: *International Journal of Mass Spectrometry* 251.1 (Mar. 2006), pp. 73–81. ISSN: 13873806. DOI: 10.1016/j.ijms.2006.01.025.

[61] Leszek J Frasinski. „Covariance Mapping Techniques." In: *Journal of Physics B: Atomic, Molecular and Optical Physics* 49.15 (Aug. 2016), p. 152004. ISSN: 0953-4075, 1361-6455. DOI: 10.1088/0953-4075/49/15/152004.

[62] O. Kornilov et al. „Coulomb Explosion of Diatomic Molecules in Intense XUV Fields Mapped by Partial Covariance." In: *Journal of Physics B: Atomic, Molecular and Optical Physics* 46.16 (Aug. 2013), p. 164028. ISSN: 0953-4075. DOI: 10.1088/0953-4075/46/16/164028.

[63] U. Graf, M. Fieß, M. Schultze, R. Kienberger, F. Krausz, and E. Goulielmakis. „Intense Few-Cycle Light Pulses in the Deep Ultraviolet." In: *Optics Express* 16.23 (Nov. 2008), p. 18956. ISSN: 1094-4087. DOI: 10.1364/OE.16.018956.

[64] Florentin Reiter, Ulrich Graf, Martin Schultze, Wolfgang Schweinberger, Hartmut Schröder, Nicholas Karpowicz, Abdallah Mohammed Azzeer, Reinhard Kienberger, Ferenc Krausz, and Eleftherios Goulielmakis. „Generation of Sub-3 Fs Pulses in the Deep Ultraviolet." In: *Optics Letters* 35.13 (July 2010), p. 2248. ISSN: 0146-9592, 1539-4794. DOI: 10.1364/OL.35.002248.

[65] Eiji J. Takahashi, Hirokazu Hasegawa, Yasuo Nabekawa, and Katsumi Midorikawa. „High-Throughput, High-Damage-Threshold Broadband Beam Splitter for High-Order Harmonics in the Extreme-Ultraviolet Region." In: *Optics Letters* 29.5 (Mar. 2004), p. 507. ISSN: 0146-9592, 1539-4794. DOI: 10.1364/OL.29.000507.

[66] Mikhail N. Polyanskiy. *Refractive Index Database*. https://refractiveindex.info.

[67] H. J. Lehmeier, W. Leupacher, and A. Penzkofer. „Nonresonant Third Order Hyperpolarizability of Rare Gases and N2 Determined by Third Harmonic Generation." In: *Optics Communications* 56.1 (Nov. 1985), pp. 67–72. ISSN: 0030-4018. DOI: 10.1016/0030-4018(85)90069-0.

[68] P. S. Banks, M. D. Feit, and M. D. Perry. „High-Intensity Third-Harmonic Generation in Beta Barium Borate through Second-Order and Third-Order Susceptibilities." In: *Optics Letters* 24.1 (Jan. 1999), pp. 4–6. ISSN: 1539-4794. DOI: 10.1364/OL.24.000004.

[69] Ulrich Gubler and Christian Bosshard. „Optical Third-Harmonic Generation of Fused Silica in Gas Atmosphere: Absolute Value of the Third-Order Nonlinear Optical Susceptibility ${\ensuremath{\chi}}^{(3)}$.“ In: *Physical Review B* 61.16 (Apr. 2000), pp. 10702–10710. DOI: 10.1103/PhysRevB.61.10702.

[70] François Légaré, ed. *Emerging Laser Technologies for High-Power and Ultrafast Science*. IOP Publishing, July 2021. ISBN: 978-0-7503-2536-3. DOI: 10.1088/978-0-7503-2536-3.

[71] Rick Trebino. *Frequency-Resolved Optical Gating: The Measurement of Ultrashort Laser Pulses*. Springer US, 2000. ISBN: 978-1-4020-7066-2. DOI: 10.1007/978-1-4615-1181-6.

[72] C. Iaconis and I. A. Walmsley. „Spectral Phase Interferometry for Direct Electric-Field Reconstruction of Ultrashort Optical Pulses.“ In: *Optics Letters* 23.10 (May 1998), pp. 792–794. ISSN: 1539-4794. DOI: 10.1364/OL.23.000792.

[73] Jonathan R. Birge, Richard Ell, Richard Ell, and Franz X. Kärtner. „Two-Dimensional Spectral Shearing Interferometry (2DSI) for Ultrashort Pulse Characterization.“ In: *Conference on Lasers and Electro-Optics/Quantum Electronics and Laser Science Conference and Photonic Applications Systems Technologies (2006), Paper CWJ6*. Optical Society of America, May 2006, CWJ6.

[74] Christian Brahms, Dane R. Austin, Francesco Tani, Allan S. Johnson, Douglas Garratt, John C. Travers, John W. G. Tisch, Philip St J. Russell, and Jon P. Marangos. „Direct Characterization of Tuneable Few-Femtosecond Dispersive-Wave Pulses in the Deep UV.“ In: *Optics Letters* 44.4 (Feb. 2019), pp. 731–734. ISSN: 1539-4794. DOI: 10.1364/OL.44.000731.

[75] T. Witting, D. Greening, D. Walke, P. Matia-Hernando, T. Barillot, J. P. Marangos, and J. W. G. Tisch. „Time-Domain Ptychography of over-Octave-Spanning Laser Pulses in the Single-Cycle Regime.“ In: *Optics Letters* 41.18 (Sept. 2016), pp. 4218–4221. ISSN: 1539-4794. DOI: 10.1364/OL.41.004218.

[76] L. Allen, D. G. C. Jones, and D. G. Schofield. „Radiative Lifetimes and Collisional Cross Sections for Xe i and Ii.“ In: *JOSA* 59.7 (July 1969), pp. 842–847. DOI: 10.1364/JOSA.59.000842.

[77] Stefan Kröll and William K. Bischel. „Two-Photon Absorption and Photoionization Cross-Section Measurements in the 5${p}^{5}$6p Configuration of Xenon.“ In: *Physical Review A* 41.3 (Feb. 1990), pp. 1340–1349. DOI: 10.1103/PhysRevA.41.1340.

[78] Alexander Kramida and Yuri Ralchenko. *NIST Atomic Spectra Database, NIST Standard Reference Database 78*. 1999. DOI: 10.18434/T4W30F.

[79] Kristina F. Chang, Han Wang, Sonia M. Poullain, David Prendergast, Daniel M. Neumark, and Stephen R. Leone. „Mapping Wave Packet Bifurcation at a Conical Intersection in CH3I by Attosecond XUV Transient Absorption Spectroscopy.“ In: *The Journal of Chemical Physics* 154.23 (June 2021), p. 234301. ISSN: 0021-9606. DOI: 10.1063/5.0056299.

[80] Coleen M. Roehl, James B. Burkholder, Geert K. Moortgat, A. R. Ravishankara, and Paul J. Crutzen. „Temperature Dependence of UV Absorption Cross Sections and Atmospheric Implications of Several Alkyl Iodides.“ In: *Journal of Geophysical Research: Atmospheres* 102.D11 (June 1997), pp. 12819–12829. ISSN: 01480227. DOI: 10.1029/97JD00530.

[81] Aharon Gedanken and Michael D. Rowe. „Magnetic Circular Dichroism of Iodoform and Methylene Iodide.“ In: *Chemical Physics* 36.2 (Jan. 1979), pp. 181–186. ISSN: 0301-0104. DOI: 10.1016/0301-0104(79)85004-1.

[82] Robert S. Mulliken. „Intensities in Molecular Electronic Spectra X. Calculations on Mixed-Halogen, Hydrogen Halide, Alkyl Halide, and Hydroxyl Spectra.“ In: *The Journal of Chemical Physics* 8.5 (May 1940), pp. 382–395. ISSN: 0021-9606. DOI: 10.1063/1.1750671.

[83] María E. Corrales, Rebeca de Nalda, and Luis Bañares. „Strong Laser Field Control of Fragment Spatial Distributions from a Photodissociation Reaction.“ In: *Nature Communications* 8.1 (Nov. 2017), p. 1345. ISSN: 2041-1723. DOI: 10.1038/s41467-017-01139-6.

[84] André T. J. B. Eppink and David H. Parker. „Methyl Iodide A-band Decomposition Study by Photofragment Velocity Imaging.“ In: *The Journal of Chemical Physics* 109.12 (Sept. 1998), pp. 4758–4767. ISSN: 0021-9606. DOI: 10.1063/1.477087.

[85] Rebeca de Nalda, Judith Durá, Alberto García-Vela, Jesús G. Izquierdo, Jesús González-Vázquez, and Luis Bañares. „A Detailed Experimental and Theoretical Study of the Femtosecond A-band Photodissociation of CH3I.“ In: *The Journal of Chemical Physics* 128.24 (June 2008), p. 244309. ISSN: 0021-9606. DOI: 10.1063/1.2943198.

[86] J. Durá, R. de Nalda, G. A. Amaral, and L. Bañares. „Imaging Transient Species in the Femtosecond A-band Photodissociation of CH3I.“ In: *The Journal of Chemical Physics* 131.13 (Oct. 2009), p. 134311. ISSN: 0021-9606. DOI: 10.1063/1.3236808.

[87] Marta L. Murillo-Sánchez, Jesús González-Vázquez, María E. Corrales, Rebeca de Nalda, Emilio Martínez-Núñez, Alberto García-Vela, and Luis Bañares. „Femtochemistry under Scrutiny: Clocking State-Resolved Channels in the Photodis-

sociation of CH3I in the A-band." In: *The Journal of Chemical Physics* 152.1 (Jan. 2020), p. 014304. ISSN: 0021-9606. DOI: 10.1063/1.5134473.

[88] Andrew R. Attar, Aditi Bhattacherjee, and Stephen R. Leone. „Direct Observation of the Transition-State Region in the Photodissociation of CH3I by Femtosecond Extreme Ultraviolet Transient Absorption Spectroscopy." In: *The Journal of Physical Chemistry Letters* 6.24 (Dec. 2015), pp. 5072–5077. DOI: 10.1021/acs.jpclett.5b02489.

[89] Emily M. Warne et al. „Photodissociation Dynamics of Methyl Iodide Probed Using Femtosecond Extreme Ultraviolet Photoelectron Spectroscopy." In: *Physical Chemistry Chemical Physics* 22.44 (2020), pp. 25695–25703. DOI: 10.1039/D0CP03478A.

[90] Emily M. Warne et al. „Photodissociation Dynamics of CH3I Probed via Multiphoton Ionisation Photoelectron Spectroscopy." In: *Physical Chemistry Chemical Physics* 21.21 (May 2019), pp. 11142–11149. ISSN: 1463-9084. DOI: 10.1039/C9CP01477B.

[91] Arne Baumann, Dimitrios Rompotis, Oliver Schepp, Marek Wieland, and Markus Drescher. „Time-Resolved Dissociation Dynamics of Iodomethane Resulting from Rydberg and Valence Excitation." In: *The Journal of Physical Chemistry A* 122.21 (May 2018), pp. 4779–4784. ISSN: 1089-5639. DOI: 10.1021/acs.jpca.8b01248.

[92] Jean Lacoursière, Michael Meyer, Laurent Nahon, Paul Morin, and Michel Larzillière. „Time-Resolved Pump-Probe Photoelectron Spectroscopy of Helium Using a Mode-Locked Laser Synchronized with Synchrotron Radiation Pulses." In: *Nuclear Instruments and Methods in Physics Research Section A: Accelerators, Spectrometers, Detectors and Associated Equipment* 351.2 (Dec. 1994), pp. 545–553. ISSN: 0168-9002. DOI: 10.1016/0168-9002(94)91384-6.

[93] Aleksey B. Alekseyev, Heinz-Peter Liebermann, and Robert J. Buenker. „Ab Initio Configuration Interaction Study of the B- and C-band Photodissociation of Methyl Iodide." In: *The Journal of Chemical Physics* 134.4 (Jan. 2011), p. 044303. ISSN: 0021-9606. DOI: 10.1063/1.3532926.

[94] Gunnar Karlström et al. „MOLCAS: A Program Package for Computational Chemistry." In: *Computational Materials Science*. Proceedings of the Symposium on Software Development for Process and Materials Design 28.2 (Oct. 2003), pp. 222–239. ISSN: 0927-0256. DOI: 10.1016/S0927-0256(03)00109-5.

[95] Francesco Aquilante et al. „Molcas 8: New Capabilities for Multiconfigurational Quantum Chemical Calculations across the Periodic Table.“ In: *Journal of Computational Chemistry* 37.5 (2016), pp. 506–541. ISSN: 1096-987X. DOI: 10.1002/jcc.24221.

[96] Markus Reiher and Alexander Wolf. „Exact Decoupling of the Dirac Hamiltonian. I. General Theory.“ In: *The Journal of Chemical Physics* 121.5 (Aug. 2004), pp. 2037–2047. ISSN: 0021-9606. DOI: 10.1063/1.1768160.

[97] Per-Olof Widmark, Per-Åke Malmqvist, and Björn O. Roos. „Density Matrix Averaged Atomic Natural Orbital (ANO) Basis Sets for Correlated Molecular Wave Functions.“ In: *Theoretica chimica acta* 77.5 (Sept. 1990), pp. 291–306. ISSN: 1432-2234. DOI: 10.1007/BF01120130.

[98] Toru Shiozaki, Werner Győrffy, Paolo Celani, and Hans-Joachim Werner. „Communication: Extended Multi-State Complete Active Space Second-Order Perturbation Theory: Energy and Nuclear Gradients.“ In: *The Journal of Chemical Physics* 135.8 (Aug. 2011), p. 081106. ISSN: 0021-9606. DOI: 10.1063/1.3633329.

[99] J. H. D. Eland, R. Frey, A. Kuestler, H. Schulte, and B. Brehm. „Unimolecular Dissociations and Internal Conversions of Methyl Halide Ions.“ In: *International Journal of Mass Spectrometry and Ion Physics* 22.1 (Nov. 1976), pp. 155–170. ISSN: 0020-7381. DOI: 10.1016/0020-7381(76)80116-7.

[100] Martin Richter, Philipp Marquetand, Jesús González-Vázquez, Ignacio Sola, and Leticia González. „SHARC: *Ab Initio* Molecular Dynamics with Surface Hopping in the Adiabatic Representation Including Arbitrary Couplings.“ In: *Journal of Chemical Theory and Computation* 7.5 (May 2011), pp. 1253–1258. ISSN: 1549-9618, 1549-9626. DOI: 10.1021/ct1007394.

[101] Aleksey B. Alekseyev, Heinz-Peter Liebermann, and Robert J. Buenker. „An Ab Initio Study of the CH3I Photodissociation. II. Transition Moments and Vibrational State Control of the I* Quantum Yields.“ In: *The Journal of Chemical Physics* 126.23 (June 2007), p. 234103. ISSN: 0021-9606. DOI: 10.1063/1.2736696.

[102] Eric W.-G. Diau, Carsten Kötting, and Ahmed H. Zewail. „Femtochemistry of Norrish Type-I Reactions: I. Experimental and Theoretical Studies of Acetone and Related Ketones on the S1 Surface.“ In: *ChemPhysChem* 2.5 (2001), pp. 273–293. ISSN: 1439-7641. DOI: 10.1002/1439-7641(20010518)2:5<273::AID-CPHC273>3.0.CO;2-H.

[103] Eric W.-G. Diau, Carsten Kötting, Theis I. Sølling, and Ahmed H. Zewail. „Femtochemistry of Norrish Type-I Reactions: III. Highly Excited Ketones—Theoretical.“ In: *ChemPhysChem* 3.1

(2002), pp. 57–78. ISSN: 1439-7641. DOI: 10.1002/1439-7641(20020118)3:1<57::AID-CPHC57>3.0.CO;2-F.

[104] Theis I. Sølling, Eric W.-G. Diau, Carsten Kötting, Steven De Feyter, and Ahmed H. Zewail. „Femtochemistry of Norrish Type-I Reactions: IV. Highly Excited Ketones—Experimental." In: *ChemPhysChem* 3.1 (2002), pp. 79–97. ISSN: 1439-7641. DOI: 10.1002/1439-7641(20020118)3:1<79::AID-CPHC79>3.0.CO;2-#.

[105] O. Hüter and F. Temps. „Ultrafast α –CC Bond Cleavage of Acetone upon Excitation to 3p and 3d Rydberg States by Femtosecond Time-Resolved Photoelectron Imaging." In: *The Journal of Chemical Physics* 145.21 (Dec. 2016), p. 214312. ISSN: 0021-9606. DOI: 10.1063/1.4971243.

[106] Mark A. Blitz, Dwayne E. Heard, and Michael J. Pilling. „Study of Acetone Photodissociation over the Wavelength Range 248-330 Nm: Evidence of a Mechanism Involving Both the Singlet and Triplet Excited States." In: *The Journal of Physical Chemistry A* 110.21 (June 2006), pp. 6742–6756. ISSN: 1089-5639. DOI: 10.1021/jp056276g.

[107] Manuela Merchán, Björn O. Roos, Ruth McDiarmid, and Xing Xing. „A Combined Theoretical and Experimental Determination of the Electronic Spectrum of Acetone." In: *The Journal of Chemical Physics* 104.5 (Feb. 1996), pp. 1791–1804. ISSN: 0021-9606. DOI: 10.1063/1.470976.

[108] David E. Couch, Henry C. Kapteyn, Margaret M. Murnane, and William K. Peters. „Uncovering Highly-Excited State Mixing in Acetone Using Ultrafast VUV Pulses and Coincidence Imaging Techniques." In: *The Journal of Physical Chemistry A* 121.12 (Mar. 2017), pp. 2361–2366. ISSN: 1089-5639, 1520-5215. DOI: 10.1021/acs.jpca.7b01112.

[109] Ryuta Uenishi, Takuya Horio, and Toshinori Suzuki. „Time-Resolved Photoelectron Imaging of Acetone with 9.3 eV Photoexcitation." In: *The Journal of Physical Chemistry A* 123.32 (Aug. 2019), pp. 6848–6853. ISSN: 1089-5639. DOI: 10.1021/acs.jpca.9b05179.

[110] M. Nobre, A. Fernandes, F. Ferreira da Silva, R. Antunes, D. Almeida, V. Kokhan, S. V. Hoffmann, N. J. Mason, S. Eden, and P. Limão-Vieira. „The VUV Electronic Spectroscopy of Acetone Studied by Synchrotron Radiation." In: *Physical Chemistry Chemical Physics* 10.4 (Jan. 2008), pp. 550–560. ISSN: 1463-9084. DOI: 10.1039/B708580J.

[111] Anne Zehnacker and Martin A. Suhm. „Chirality Recognition between Neutral Molecules in the Gas Phase." In: *Angewandte Chemie International Edition* 47.37 (2008), pp. 6970–6992. ISSN: 1521-3773. DOI: 10.1002/anie.200800957.

[112] Norma J. Greenfield. „Using Circular Dichroism Spectra to Estimate Protein Secondary Structure." In: *Nature protocols* 1.6 (2006), pp. 2876–2890. ISSN: 1754-2189. DOI: 10.1038/nprot.2006.202.

[113] N. Böwering, T. Lischke, B. Schmidtke, N. Müller, T. Khalil, and U. Heinzmann. „Asymmetry in Photoelectron Emission from Chiral Molecules Induced by Circularly Polarized Light." In: *Physical Review Letters* 86.7 (Feb. 2001), pp. 1187–1190. DOI: 10.1103/PhysRevLett.86.1187.

[114] Samuel Beaulieu et al. „Probing Ultrafast Dynamics of Chiral Molecules Using Time-Resolved Photoelectron Circular Dichroism." In: *Faraday Discussions* 194.0 (Dec. 2016), pp. 325–348. ISSN: 1364-5498. DOI: 10.1039/C6FD00113K.

[115] Burke Ritchie. „Theory of the Angular Distribution of Photoelectrons Ejected from Optically Active Molecules and Molecular Negative Ions." In: *Physical Review A* 13.4 (Apr. 1976), pp. 1411–1415. DOI: 10.1103/PhysRevA.13.1411.

[116] C. Stefan Lehmann, N. Bhargava Ram, Ivan Powis, and Maurice H. M. Janssen. „Imaging Photoelectron Circular Dichroism of Chiral Molecules by Femtosecond Multiphoton Coincidence Detection." In: *The Journal of Chemical Physics* 139.23 (Dec. 2013), p. 234307. ISSN: 0021-9606. DOI: 10.1063/1.4844295.

[117] Laurent Nahon, Gustavo A. Garcia, Chris J. Harding, Elisabeth Mikajlo, and Ivan Powis. „Determination of Chiral Asymmetries in the Valence Photoionization of Camphor Enantiomers by Photoelectron Imaging Using Tunable Circularly Polarized Light." In: *The Journal of Chemical Physics* 125.11 (Sept. 2006), p. 114309. ISSN: 0021-9606. DOI: 10.1063/1.2336432.

[118] Gustavo A. Garcia, Héloïse Dossmann, Laurent Nahon, Steven Daly, and Ivan Powis. „Photoelectron Circular Dichroism and Spectroscopy of Trifluoromethyl- and Methyl-Oxirane: A Comparative Study." In: *Physical Chemistry Chemical Physics* 16.30 (July 2014), pp. 16214–16224. ISSN: 1463-9084. DOI: 10.1039/C4CP01941E.

[119] Gustavo A. Garcia, Laurent Nahon, Chris J. Harding, and Ivan Powis. „Chiral Signatures in Angle-Resolved Valence Photoelectron Spectroscopy of Pure Glycidol Enantiomers." In: *Physical Chemistry Chemical Physics* 10.12 (Mar. 2008), pp. 1628–1639. ISSN: 1463-9084. DOI: 10.1039/B714095A.

[120] Stefano Turchini, Daniele Catone, Giorgio Contini, Nicola Zema, Simona Irrera, Mauro Stener, Devis Di Tommaso, Piero Decleva, and Tommaso Prosperi. „Conformational Effects in Photoelectron Circular Dichroism of Alaninol.“ In: *ChemPhysChem* 10.11 (2009), pp. 1839–1846. ISSN: 1439-7641. DOI: 10.1002/cphc.200800862.

[121] Ivan Powis, Chris J. Harding, Gustavo A. Garcia, and Laurent Nahon. „A Valence Photoelectron Imaging Investigation of Chiral Asymmetry in the Photoionization of Fenchone and Camphor.“ In: *ChemPhysChem* 9.3 (2008), pp. 475–483. ISSN: 1439-7641. DOI: 10.1002/cphc.200700748.

[122] Laurent Nahon, Lipsa Nag, Gustavo A. Garcia, Iuliia Myrgorodska, Uwe Meierhenrich, Samuel Beaulieu, Vincent Wanie, Valérie Blanchet, Romain Géneaux, and Ivan Powis. „Determination of Accurate Electron Chiral Asymmetries in Fenchone and Camphor in the VUV Range: Sensitivity to Isomerism and Enantiomeric Purity.“ In: *Physical Chemistry Chemical Physics* 18.18 (May 2016), pp. 12696–12706. ISSN: 1463-9084. DOI: 10.1039/C6CP01293K.

[123] Antoine Comby et al. „Relaxation Dynamics in Photoexcited Chiral Molecules Studied by Time-Resolved Photoelectron Circular Dichroism: Toward Chiral Femtochemistry.“ In: *The Journal of Physical Chemistry Letters* 7.22 (Nov. 2016), pp. 4514–4519. DOI: 10.1021/acs.jpclett.6b02065.

[124] S. Beaulieu et al. „Attosecond-Resolved Photoionization of Chiral Molecules.“ In: *Science* 358.6368 (Dec. 2017), pp. 1288–1294. DOI: 10.1126/science.aao5624.

[125] D. Faccialà et al. „Time-Resolved Chiral X-Ray Photoelectron Spectroscopy with Transiently Enhanced Atomic Site-Selectivity: A Free Electron Laser Investigation of Electronically Excited Fenchone Enantiomers.“ In: *arXiv:2202.13704 [physics]* (Feb. 2022). arXiv: 2202.13704 [physics].

[126] Laurent Nahon, Gustavo A. Garcia, and Ivan Powis. „Valence Shell One-Photon Photoelectron Circular Dichroism in Chiral Systems.“ In: *Journal of Electron Spectroscopy and Related Phenomena*. Gas Phase Spectroscopic and Dynamical Studies at Free-Electron Lasers and Other Short Wavelength Sources 204 (Oct. 2015), pp. 322–334. ISSN: 0368-2048. DOI: 10.1016/j.elspec.2015.04.008.

[127] Gustavo A. Garcia, Laurent Nahon, Steven Daly, and Ivan Powis. „Vibrationally Induced Inversion of Photoelectron Forward-Backward Asymmetry in Chiral Molecule Photoionization by Circularly Polarized Light.“ In: *Nature Communications* 4.1 (July 2013), p. 2132. ISSN: 2041-1723. DOI: 10.1038/ncomms3132.

[128] Morgane Vacher, Michael J. Bearpark, Michael A. Robb, and João Pedro Malhado. „Electron Dynamics upon Ionization of Polyatomic Molecules: Coupling to Quantum Nuclear Motion and Decoherence." In: *Physical Review Letters* 118.8 (Feb. 2017), p. 083001. DOI: 10.1103/PhysRevLett.118.083001.

[129] S. Beaulieu et al. „Photoexcitation Circular Dichroism in Chiral Molecules." In: *Nature Physics* 14.5 (May 2018), pp. 484–489. ISSN: 1745-2481. DOI: 10.1038/s41567-017-0038-z.

[130] R. E. Goetz, T. A. Isaev, B. Nikoobakht, R. Berger, and C. P. Koch. „Theoretical Description of Circular Dichroism in Photoelectron Angular Distributions of Randomly Oriented Chiral Molecules after Multi-Photon Photoionization." In: *The Journal of Chemical Physics* 146.2 (Jan. 2017), p. 024306. ISSN: 0021-9606. DOI: 10.1063/1.4973456.

[131] Léon Sanche. „Beyond Radical Thinking." In: *Nature* 461.7262 (Sept. 2009), pp. 358–359. ISSN: 1476-4687. DOI: 10.1038/461358a.

[132] Q.-B. Lu and L. Sanche. „Effects of Cosmic Rays on Atmospheric Chlorofluorocarbon Dissociation and Ozone Depletion." In: *Physical Review Letters* 87.7 (July 2001), p. 078501. DOI: 10.1103/PhysRevLett.87.078501.

[133] Elahe Alizadeh and Léon Sanche. „Precursors of Solvated Electrons in Radiobiological Physics and Chemistry." In: *Chemical Reviews* 112.11 (Nov. 2012), pp. 5578–5602. ISSN: 0009-2665. DOI: 10.1021/cr300063r.

[134] Elahe Alizadeh, Thomas M. Orlando, and Léon Sanche. „Biomolecular Damage Induced by Ionizing Radiation: The Direct and Indirect Effects of Low-Energy Electrons on DNA." In: *Annual Review of Physical Chemistry* 66.1 (Apr. 2015), pp. 379–398. ISSN: 0066-426X, 1545-1593. DOI: 10.1146/annurev-physchem-040513-103605.

[135] Léon Sanche. „Low-Energy Electron Damage to DNA and Its Basic Constituents." In: *Physica Scripta* 68.5 (Jan. 2003), p. C108. ISSN: 1402-4896. DOI: 10.1238/Physica.Regular.068a0C108.

[136] Yoshi-Ichi Suzuki, Kiyoshi Nishizawa, Naoya Kurahashi, and Toshinori Suzuki. „Effective Attenuation Length of an Electron in Liquid Water between 10 and 600 eV." In: *Physical Review E* 90.1 (July 2014), p. 010302. DOI: 10.1103/PhysRevE.90.010302.

[137] Stephan Thürmer, Robert Seidel, Manfred Faubel, Wolfgang Eberhardt, John C. Hemminger, Stephen E. Bradforth, and Bernd Winter. „Photoelectron Angular Distributions from Liquid Water: Effects of Electron Scattering." In: *Physical Review Letters* 111.17 (Oct. 2013), p. 173005. DOI: 10.1103/PhysRevLett.111.173005.

[138] Junichi Nishitani, Yo-ichi Yamamoto, Christopher W. West, Shutaro Karashima, and Toshinori Suzuki. „Binding Energy of Solvated Electrons and Retrieval of True UV Photoelectron Spectra of Liquids.“ In: *Science Advances* 5.8 (), eaaw6896. DOI: 10.1126/sciadv.aaw6896.

[139] Ruth Signorell. „Electron Scattering in Liquid Water and Amorphous Ice: A Striking Resemblance.“ In: *Physical Review Letters* 124.20 (May 2020), p. 205501. DOI: 10.1103/PhysRevLett.124.205501.

[140] David Luckhaus, Yo-ichi Yamamoto, Toshinori Suzuki, and Ruth Signorell. „Genuine Binding Energy of the Hydrated Electron.“ In: *Science Advances* 3.4 (), e1603224. DOI: 10.1126/sciadv.1603224.

[141] M. Michaud, A. Wen, and L. Sanche. „Cross Sections for Low-Energy (1–100 eV) Electron Elastic and Inelastic Scattering in Amorphous Ice.“ In: *Radiation Research* 159.1 (Jan. 2003), pp. 3–22. ISSN: 0033-7587, 1938-5404. DOI: 10.1667/0033-7587(2003)159[0003:CSFLEE]2.0.CO;2.

[142] Conaill F. Perry, Inga Jordan, Pengju Zhang, Aaron von Conta, Fernanda B. Nunes, and Hans Jakob Wörner. „Photoelectron Spectroscopy of Liquid Water with Tunable Extreme-Ultraviolet Radiation: Effects of Electron Scattering.“ In: *The Journal of Physical Chemistry Letters* 12.11 (Mar. 2021), pp. 2990–2996. ISSN: 1948-7185, 1948-7185. DOI: 10.1021/acs.jpclett.0c03424.

[143] Thomas E. Gartmann, Sebastian Hartweg, Loren Ban, Egor Chasovskikh, Bruce L. Yoder, and Ruth Signorell. „Electron Scattering in Large Water Clusters from Photoelectron Imaging with High Harmonic Radiation.“ In: *Physical Chemistry Chemical Physics* 20.24 (2018), pp. 16364–16371. ISSN: 1463-9076, 1463-9084. DOI: 10.1039/C8CP02148A.

[144] Thomas E. Gartmann, Loren Ban, Bruce L. Yoder, Sebastian Hartweg, Egor Chasovskikh, and Ruth Signorell. „Relaxation Dynamics and Genuine Properties of the Solvated Electron in Neutral Water Clusters.“ In: *The Journal of Physical Chemistry Letters* 10.17 (Sept. 2019), pp. 4777–4782. DOI: 10.1021/acs.jpclett.9b01802.

[145] Inga Jordan, Martin Huppert, Dominik Rattenbacher, Michael Peper, Denis Jelovina, Conaill Perry, Aaron von Conta, Axel Schild, and Hans Jakob Wörner. „Attosecond Spectroscopy of Liquid Water.“ In: *Science* 369.6506 (Aug. 2020), pp. 974–979. DOI: 10.1126/science.abb0979.

[146] L. Seiffert et al. „Attosecond Chronoscopy of Electron Scattering in Dielectric Nanoparticles.“ In: *Nature Physics* 13.8 (Aug. 2017), pp. 766–770. ISSN: 1745-2481. DOI: 10.1038/nphys4129.

[147] Bernd Winter. „Liquid Microjet for Photoelectron Spectroscopy.“ In: *Nuclear Instruments and Methods in Physics Research Section A: Accelerators, Spectrometers, Detectors and Associated Equipment*. Special Issue in Honour of Prof. Kai Siegbahn 601.1 (Mar. 2009), pp. 139–150. ISSN: 0168-9002. DOI: 10.1016/j.nima.2008.12.108.

[148] Toshinori Suzuki. „Ultrafast Photoelectron Spectroscopy of Aqueous Solutions.“ In: *The Journal of Chemical Physics* 151.9 (Sept. 2019), p. 090901. ISSN: 0021-9606. DOI: 10.1063/1.5098402.

[149] Andrea Trabattoni et al. „Photoelectron Spectroscopy of Large Water Clusters Ionized by an XUV Comb.“ In: *Journal of Physics: Photonics* 2.3 (July 2020), p. 035007. ISSN: 2515-7647. DOI: 10.1088/2515-7647/ab92b1.

[150] H.G. Muller. „Reconstruction of Attosecond Harmonic Beating by Interference of Two-Photon Transitions.“ In: *Applied Physics B* 74.1 (June 2002), s17–s21. ISSN: 1432-0649. DOI: 10.1007/s00340-002-0894-8.

[151] P. B. Corkum. „Plasma Perspective on Strong Field Multiphoton Ionization.“ In: *Physical Review Letters* 71.13 (Sept. 1993), pp. 1994–1997. DOI: 10.1103/PhysRevLett.71.1994.

[152] U. Even. „“The Even-Lavie Valve as a Source for High Intensity Supersonic Beam”.“ In: *EPJ Techniques and Instrumentation* 2.1 (Dec. 2015), pp. 1–22. ISSN: 2195-7045. DOI: 10.1140/epjti/s40485-015-0027-5.

[153] Thomas E. Gartmann, Sebastian Hartweg, Loren Ban, Egor Chasovskikh, Bruce L. Yoder, and Ruth Signorell. „Electron Scattering in Large Water Clusters from Photoelectron Imaging with High Harmonic Radiation.“ In: *Physical Chemistry Chemical Physics* 20.24 (June 2018), pp. 16364–16371. ISSN: 1463-9084. DOI: 10.1039/C8CP02148A.

[154] C. Bobbert, S. Schütte, C. Steinbach, and U. Buck. „Fragmentation and Reliable Size Distributions of Large Ammonia and Water Clusters.“ In: *The European Physical Journal D - Atomic, Molecular, Optical and Plasma Physics* 19.2 (May 2002), pp. 183–192. ISSN: 1434-6079. DOI: 10.1140/epjd/e20020070.

[155] Bruce L. Yoder, Adam H. C. West, Bernhard Schläppi, Egor Chasovskikh, and Ruth Signorell. „A Velocity Map Imaging Photoelectron Spectrometer for the Study of Ultrafine Aerosols with a Table-Top VUV Laser and Na-doping for Particle Sizing Applied to Dimethyl Ether Condensation.“ In: *The Journal of Chemical Physics* 138.4 (Jan. 2013), p. 044202. ISSN: 0021-9606. DOI: 10.1063/1.4788620.

[156] Silko Barth, Milan Ončák, Volker Ulrich, Melanie Mucke, Toralf Lischke, Petr Slavíček, and Uwe Hergenhahn. „Valence Ionization of Water Clusters: From Isolated Molecules to Bulk.“ In: *The Journal of Physical Chemistry A* 113.48 (Dec. 2009), pp. 13519–13527. ISSN: 1089-5639, 1520-5215. DOI: 10.1021/jp906113e.

[157] J. A. R. Samson and W. C. Stolte. „Precision Measurements of the Total Photoionization Cross-Sections of He, Ne, Ar, Kr, and Xe.“ In: *Journal of Electron Spectroscopy and Related Phenomena*. Determination of Cross-Sections and Momentum Profiles of Atoms, Molecules and Condensed Matter 123.2 (May 2002), pp. 265–276. ISSN: 0368-2048. DOI: 10.1016/S0368-2048(02)00026-9.

[158] G. N. Haddad and James A. R. Samson. „Total Absorption and Photoionization Cross Sections of Water Vapor between 100 and 1000 Å.“ In: *The Journal of Chemical Physics* 84.12 (June 1986), pp. 6623–6626. ISSN: 0021-9606. DOI: 10.1063/1.450715.

[159] Eli. Grushka. „Characterization of Exponentially Modified Gaussian Peaks in Chromatography.“ In: *Analytical Chemistry* 44.11 (Sept. 1972), pp. 1733–1738. ISSN: 0003-2700. DOI: 10.1021/ac60319a011.

[160] Sebastian Hartweg, Bruce L. Yoder, Gustavo A. Garcia, Laurent Nahon, and Ruth Signorell. „Size-Resolved Photoelectron Anisotropy of Gas Phase Water Clusters and Predictions for Liquid Water.“ In: *Physical Review Letters* 118.10 (Mar. 2017), p. 103402. DOI: 10.1103/PhysRevLett.118.103402.

DECLARATION

Eidesstattliche Versicherung

Hiermit versichere ich an Eides statt, die vorliegende Dissertationsschrift selbst verfasst und keine anderen als die angegebenen Hilfsmittel und Quellen benutzt zu haben.

Die eingereichte schriftliche Fassung entspricht der auf dem elektronischen Speichermedium.

Die Dissertation wurde in der vorgelegten oder einer ähnlichen Form nicht schon einmal in einem früheren Promotionsverfahren angenommen oder als ungenügend beurteilt.

Hamburg, den 27.03.2022

Lorenzo Colaizzi

COLOPHON

This document was typeset using the typographical look-and-feel `classicthesis` developed by André Miede and Ivo Pletikosić. The style was inspired by Robert Bringhurst's seminal book on typography "*The Elements of Typographic Style*". `classicthesis` is available for both LaTeX and LyX:

https://bitbucket.org/amiede/classicthesis/

Final Version as of December 5, 2022 (classicthesis v4.6).